Identifying the role of nucleotide binding and hydrolysis in MutS in the molecular enzymology of *E. coli* DNA mismatch repair initiation

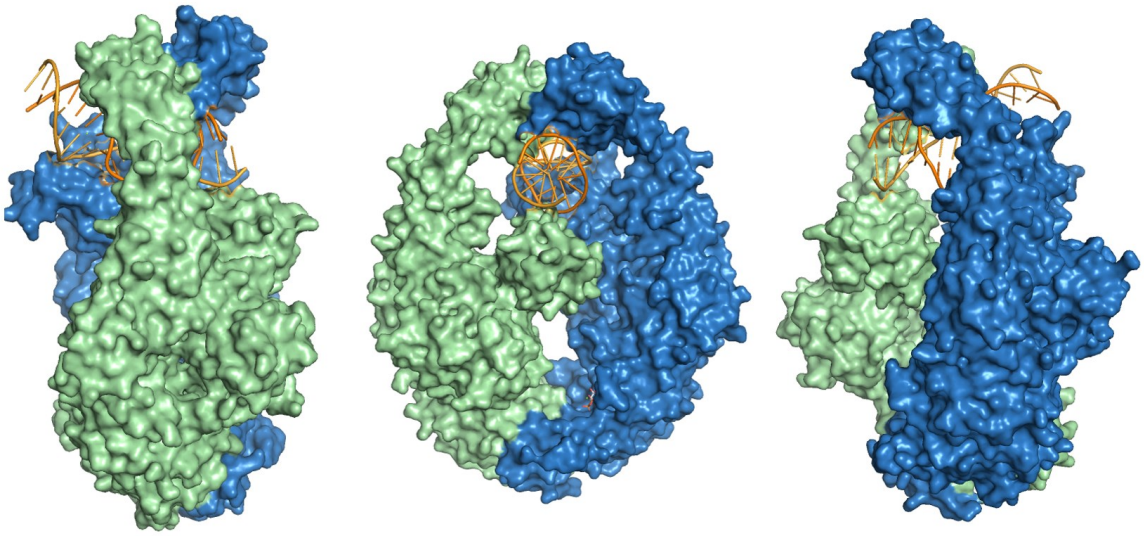

Vincent P.E. Kruit

Master End Project for MSc. in Nanobiology

Supervisors

Dr. Ir. Joyce H.G. Lebbink

Charlie Laffeber

Performed at

Lebbink laboratory

Department of Molecular Genetics

Erasmus Medical Centre Rotterdam

“Do not waste clean thinking on dirty enzymes” – Arthur Kornberg

Contents

1

Introduction

I.1 General introduction

The DNA mismatch repair (MMR) pathway plays a crucial role in safeguarding genome integrity and ensuring faithful replication[1–3]. The importance of this pathway is underscored by its high degree of conservation from bacteria to humans. Dysfunctional MMR results in enhanced mutation rates, microsatellite instability, antibiotic resistance in bacteria and cancer in mammals[2,4–7]. Moreover, in humans defective MMR is the leading cause of hereditary nonpolyposis colorectal cancer, also known as Lynch syndrome[4,7–10].

In *Escherichia coli* MMR initiation is sequentially orchestrated by MutS, MutL and MutH. Orthologous proteins are involved in eukaryotic MMR initiation[2]. Following mismatch recognition and upon nucleotide exchange, the mismatch-bound form of MutS (ADP-bound state) undergoes a conformational transition into a so-called "sliding clamp" (ATP-bound state) (**Fig. 1**)[11]. Subsequently, the MutS sliding clamp recruits MutL in a hydrolysis-independent fashion, forming a MutS-MutL-DNA ternary complex[11,12]. In turn MutL recruits the latent MutH endonuclease which nicks the nascent strand at transiently hemi-methylated GATC sites, serving as entry point for downstream repair effectors such as the UvrD helicase.

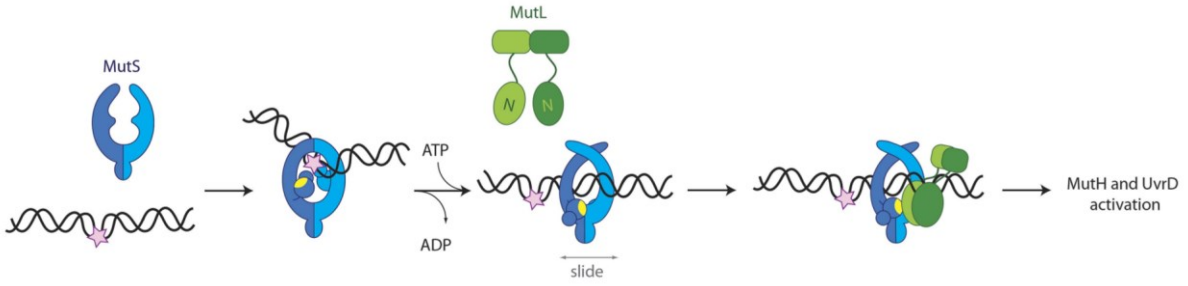

***Figure 1**. Schematic overview of MutS mismatch recognition and the subsequent nucleotide-exchange mediated conformational transition into a sliding clamp that recruits MutL during MMR initiation. In turn, MutL activates downstream effectors, such as MutH and UvrD. Taken from Groothuizen et al. 2015[13].*

One of the most contentious and heavily debated subjects in the MMR field is the molecular mechanism of communication by which mismatch recognition is coupled to strand discrimination and specifically what role ATP hydrolysis by MutS plays during MMR initiation[14]. Dominant MMR models pose that ATP hydrolysis by post mismatch recognition MutS enables its dissociation from the DNA once MutS encounters ssDNA, thereby resetting the system[15,16]. Other studies indicate that ATP hydrolysis fuels translocation along the DNA backbone either during an active search for mismatches or in the post mismatch recognition states of MutS[17–19].

However, Hao et al. (2020) recently showed by single-molecule Förster Resonance Energy Transfer (FRET) that in the absence of MutL and MutH, ATP hydrolysis enables *Thermus aquaticus* (Taq) MutS to rebind the mismatch, leading to localization of MutS and assembly of downstream effectors in the vicinity of the mismatch[20]. This finding indicates that in contrast to dominant MMR models the MutS sliding clamp is hydrolysing ATP while remaining on DNA, which induces additional conformational changes, enabling recurrent binding of the mismatch. As these proteins are highly conserved functional orthologs of eukaryotic MMR proteins, understanding how these initiate *E. coli* MMR will progress the entire scientific MMR field and impact future clinical studies.

I.2 Aim and outline

The main goal of this study is to generate and characterize a series of active site MutS mutants with variable ATPase activity which may be used to investigate the role of ATP hydrolysis by MutS during MMR initiation. Mutational analysis has shown that the glutamate at position 694 (E694), located in the Walker B motif of the active site of the C-terminal ATPase domain in MutS (**Fig. 2**), is implicated in ATP hydrolysis[12,21,22]. Further understanding the functional implications of this residue, specifically in ATP hydrolysis, may aid in understanding the mode of communication between mismatch recognition by MutS and strand incision by MutH. Therefore, active site mutants wherein the glutamate at position 694 (E694) is mutated to a glutamine (E694Q), aspartic acid (E694D) or asparagine (E694N) were generated and functionally characterized. We hypothesise that the negative charge on this residue is imperative for ATPase activity, therefore we chose to introduce the aforementioned mutations which remove the negative charge (E694Q), decrease the sidechain length (E694D), or both (E694N) which is expected to differentially affect ATPase activity.

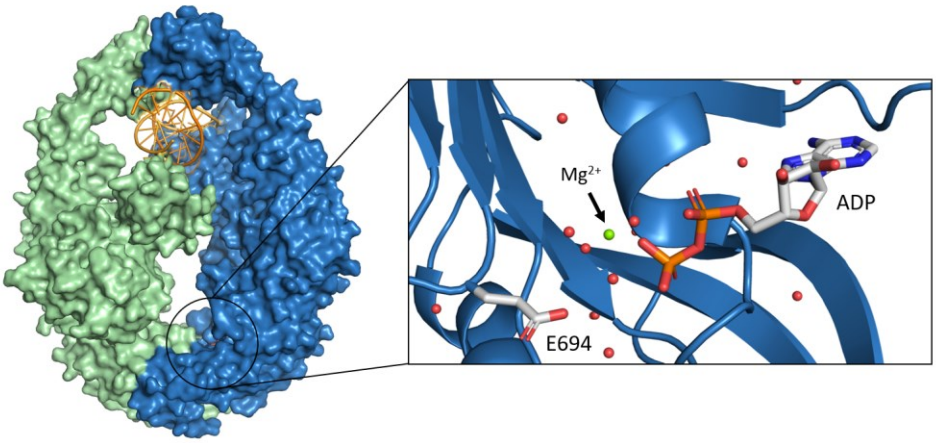

Figure 2. Crystal structure of mismatch-bound MutS*. Monomer A and B are colored in green and blue, respectively. DNA is shown in orange. Inset shows the active site of the C-terminal ATPase domain with the catalytic magnesium shown as green sphere, water molecules as red spheres and residue E694 as well as ADP are shown as sticks. PDB code: 1E3M.*

To elucidate the functional implications of the introduced mutations, ATPase activity was investigated using a custom colorimetric ATPase assay which first had to be implemented and optimized. Subsequently, DNA and nucleotide binding were assessed by Surface Plasmon Resonance (SPR) spectroscopy and nucleotide-exchange was studied using a fluorescent analogue of ADP, Mant-ADP. Finally, to elucidate the functional effects on the mechanistic interaction between MutS, MutL and MutH, *in vitro* assays utilizing the reconstituted MMR pathway in state-of-the-art incision assays and real-time FRET experiments were conducted.

I.3 Theoretical background

I.3.1 The E. coli DNA mismatch repair pathway

I.3.1.1 Mismatch recognition and MutS sliding clamp formation

Misincorporation of nucleotides and slippage of DNA polymerase during DNA replication lead to mismatches. To ensure faithful replication and safeguard genome integrity these errors are corrected by the DNA mismatch repair (MMR) pathway, complementing the DNA polymerase proofreading

ability and reducing the mutation frequency by an additional factor of 100-1000[6,23–25]. Additionally, MMR prevents illegitimate homeologous recombination between divergent DNA sequences and has been implicated in DNA damage signalling, triplet repeat expansion and antibody diversification[26–31]. Moreover, MMR is involved in recognizing DNA modified by alkylation and intercalators, thereby conferring sensitivity to DNA-damaging agents[32–36].

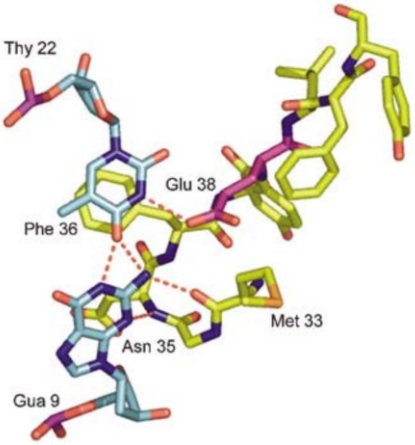

***Figure 3**. Binding of MutS (yellow) to a GT mismatch (blue). The side chain of Phe 36 is stacking on the thymidine base, glutamate 38 (side chain colored magenta) is forming a hydrogen bond with the thymidine. Taken from Lebbink et al. 2006[44].*

The MMR pathway consists of a cascade of proteins which act sequentially. In *E. coli* mismatches are recognized by the homodimeric (or homotetrameric) ATP Binding Cassette (ABC)-family MutS ATPase, which constantly scans replicated DNA for mismatches using highly conserved phenylalanine (F36) and glutamate (E38) residues (Phe-X-Glu motif) in the N-terminal domain (**Fig. 3**)[37]. During each binding event MutS rapidly scans thousands of basepairs at speeds of 700 bp s^{-1} whilst the DNA is held between the mismatch-binding and clamp domains (**Fig. 4a**) which, unlike in mismatch-bound MutS (**Fig. 4b and Fig. 5**), retain the DNA in a straight conformation. However, recently obtained cryo-EM structures reveal that MutS actively attempts to distort the DNA while scanning[11].

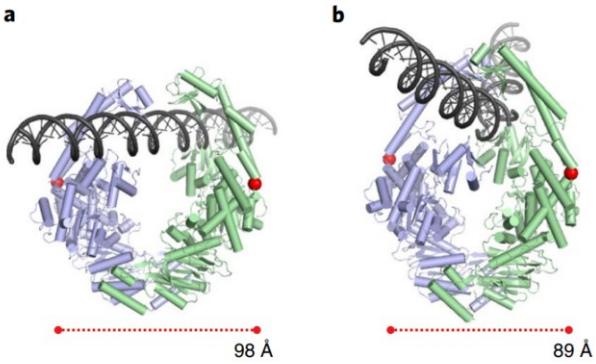

***Figure 4**. Structures of scanning (**a**) and mismatch-bound MutS (**b**). Monomer A and B are shown in green and blue, respectively. Each residue at position 400 is marked by a red sphere and their distance is shown below. DNA is shown in black. Taken from Fernandez-Leiro et al. (2021)[11].*

Furthermore, although *E. coli* MutS is homodimeric it functions as a heterodimer since both monomers play asymmetric roles in mismatch recognition. The ADP bound monomer is able to bind to the mismatch, whereas the other nucleotide free monomer is not[38]. In eukaryotes this asymmetric mismatch recognition is conserved and emphasized by the heterodimeric composition of MutSα (Msh2-Msh6)[39].

In *E. coli* MutS the phenylalanine of the Phe-X-Glu motif protrudes into the minor groove of the DNA helix and upon mismatch recognition stabilizes mismatch binding by π-stacking onto one of the mismatched bases, mimicking a DNA base (**Fig. 3**). In addition, the glutamate in this motif participates in hydrogen bonding with the mismatch, leading to stable mismatch binding and local structural rearrangements, resulting in a 60° bend in the DNA backbone towards the major groove[40–43].

Moreover, hydrogen bonding between the mismatch and the glutamate confers mismatch specificity and triggers intramolecular signalling, resulting in inhibition of ATP hydrolysis and tightening of the MutS dimer[44]. These local structural rearrangements are thought to license the conformational transformation into a so-called sliding clamp, thereby inhibiting formation of sliding clamps on homoduplex DNA.

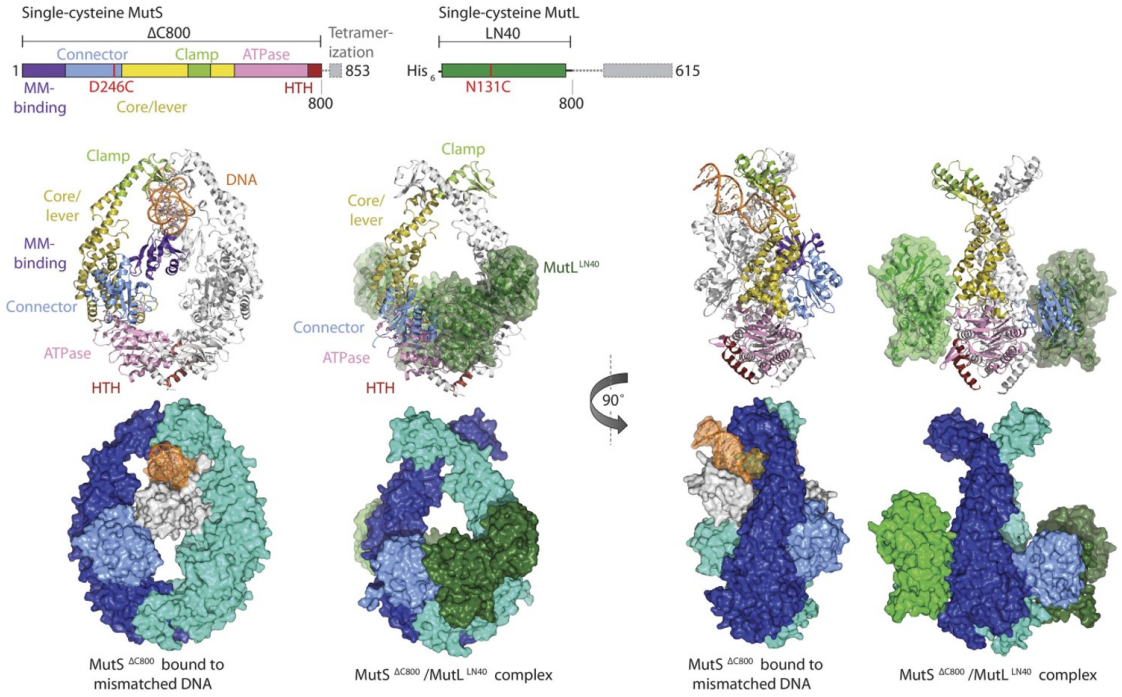

Figure 5. Crystal structures of MutS$^{\Delta C800}$ in the mismatch-recognition state and crosslinked to MutL^{LN40} in closed conformation*. Domain and construct definitions are shown on top. Monomer A and B of MutS are shown in blue and cyan, respectively. Adapted from Groothuizen et al. 2015[13].*

Subsequently, the conformational change into a sliding clamp is triggered by nucleotide exchange (ADP release and ATP binding)[12,15]. Prevailing MMR models pose that once the MutS sliding clamp is formed it is "blind" to the mismatch and laterally diffuses along the DNA helix in a hydrolysis-independent fashion[16,45]. During the sliding clamp transition the mismatch and connector domain of MutS rotate outwards by 180°, forming a new and larger channel for the DNA (**Fig. 5**). This conformational transition exposes a second MutL binding interface, enabling stable binding of the 40 kDa N-terminal MutL domains (LN40) and the formation of a MutS-MutL-DNA ternary complex (**Fig. 5 and Fig. 6**)[46]. In addition to the binding interfaces on MutS, formation of the MutS-MutL-DNA ternary complex is stabilized by the positively charged cleft present on the N-terminal MutL domains that interact with the DNA (**Fig. 8**)[47].

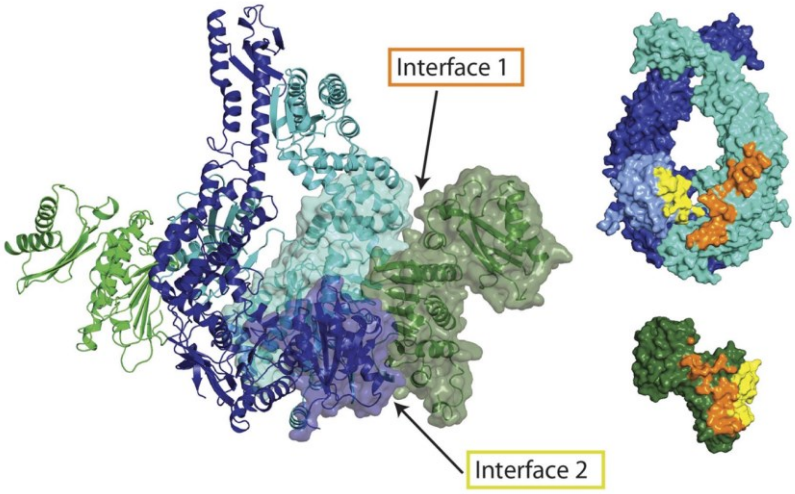

Figure 6. MutS$^{\Delta C800}$-MutL^{LN40} complex formation as determined by X-ray crystallography*. The MutS sliding clamp (blue and cyan) is able to bind the N-terminal MutL domain, LN40, (green) via interfaces on the ATPase (orange) and connector (yellow) domains. Taken from Groothuizen et al. 2015*[13]*.*

Borsellini et al. (2022) recently showed by cryo-electron microscopy (Cryo-EM) that in the absence of DNA and upon binding a single ATP molecule, the MutS dimer undergoes partial closure (**Fig. 7b**)[15]. Furthermore, when AMPPNP (a nonhydrolyzable ATP analogue) is bound to both subunits, an even more closed conformational state is observed (**Fig. 7c**). These closed states are expected to exhibit decreased affinity for DNA, necessitating ATP hydrolysis and a subsequent conformational transition to a more open state, to enable DNA binding.

Although it is clear that ATP binding and hydrolysis facilitate transitioning between the different conformational states of MutS, the exact underlying molecular mechanism remains unknown. Importantly, a detailed mechanistic description of how mismatch-bound MutS recruits and activates MutL and, in particular, which conformational changes in both proteins are required, is still lacking.

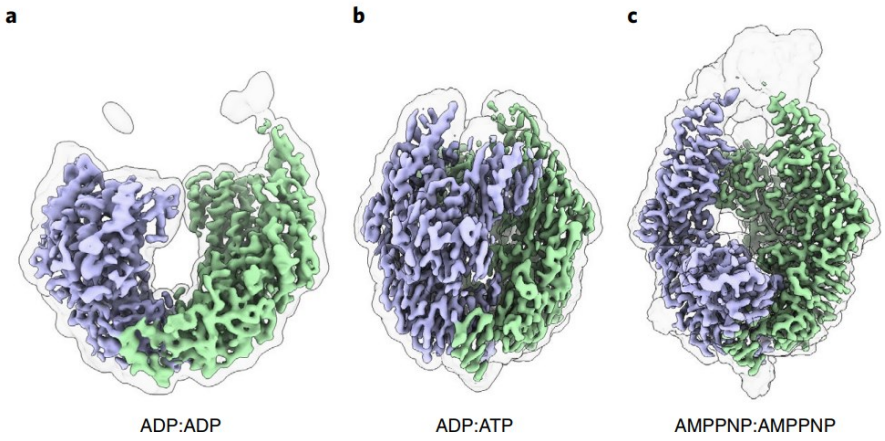

Figure 7. Various nucleotide-mediated conformational states of the MutS dimer in the absence of DNA. a*, In the presence of ADP bound to both subunits, MutS adopts an open conformation that facilitates DNA binding.* ***b****, Binding of ATP to one of the subunits induces a closed conformational state.* ***c****, Binding of AMPPNP to both subunits induces an even more closed conformation. Monomer A and Monomer B are represented in green and blue, respectively. The cryo-EM maps at a lower contour level are indicated by transparent outlines. Taken from Borsellini et al. 2022*[15]*.*

I.3.1.2 The MutL ATPase and MutH endonuclease

In *E. coli* the homodimeric MutL ATPase assists MutS during coordination of MMR initiation by recruitment and activation of the latent MutH endonuclease as well as the UvrD helicase. *E. coli* MutL belongs to the GHKL (Gyrase, Hsp90, histidine kinase and MutL) ATPase/kinase superfamily and upon nucleotide binding the N-terminal domains become ordered and are able to dimerize, enabling the formation of a MutL sliding clamp[48,49].

Subsequently, the nucleotide-mediated structural rearrangements in the N-terminal domains result in a high affinity MutH binding site, enabling MutH recruitment. In methyl-directed MMR, as found in *E. coli* and related gram negative y-proteobacteria, either the MutS-MutL-MutH supercomplex or MutL-MutH complex searches for a transiently hemi-methylated GATC site which discriminates the methylated template from the unmethylated nascent strand. Subsequently, MutH nicks the nascent strand 5' of the Guanine in the GATC motif. The nick will serve as entry point for the UvrD helicase, which is also recruited by MutL and together with a 5'-3' or 3'-5' exonuclease this leads to the displacement and degradation of the nascent strand[50]. Following degradation, the repair tract is resynthesized and ligated by DNA polymerase and DNA ligase, respectively.

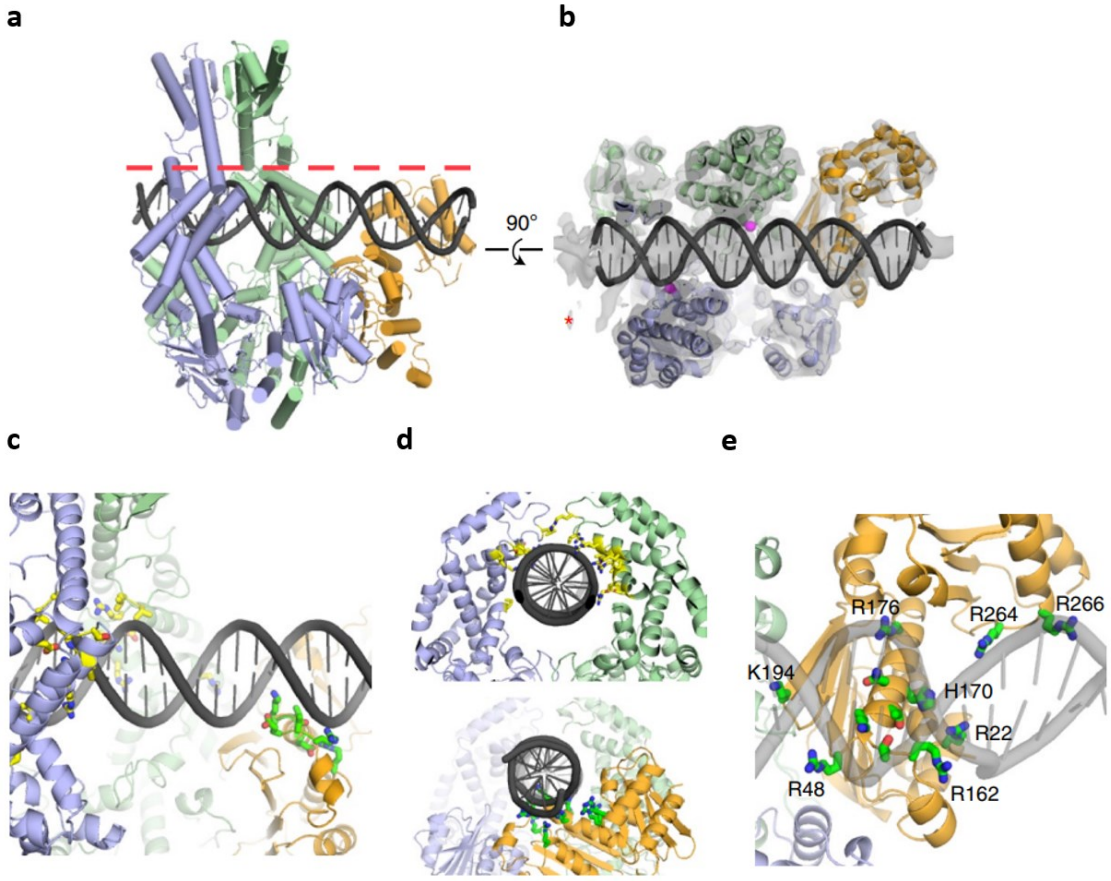

***Figure 8. MutS-MutL^{LN40}-DNA ternary complex. a**, Side view of MutS-MutL^{LN40}-DNA ternary complex. Dashed line indicates viewpoint in **b**. **b**, The cryo-EM map, depicted as a translucent gray surface at a contour level of 5, illustrates the cut-through of MutL^{LN40}-MutS. Within monomer B, the anticipated location of MutL^{LN40} is denoted by a red asterisk (*). The lever and clamp domains have been excluded from the depiction to enhance clarity. **c**, DNA interaction in the MutS-MutL^{LN40} complex. MutS and MutL residues involved in DNA binding are depicted in yellow and green, respectively. **d**, Front view of DNA*

interacting residues in MutS (top) and MutL^{LN40} (bottom). ***e****, Top view of DNA-interacting MutL^{LN40} residues. Adapted from Fernandez-Leiro et al. 2021*[11]*.*

The N-terminal MutL domains are connected to the C-terminal dimerization domains via 100 residue long proline-rich flexible linkers. The linkers generate a large central cavity which includes DNA during signal propagation[51]. In addition to DNA inclusion, the unstructured linkers enable bypass of roadblocks during movement across the DNA helix[52]. Up to 40 residues of the linker can be deleted without functional consequences, however deletion of the region close to the N-terminal ATPase domains impairs functionality *in vivo,* although DNA binding and ATPase activity are not affected[53]. Furthermore, binding of MutL to the DNA is stabilized by the positively charged cleft present on the N-terminal MutL domains (**Fig. 8**). Removal of the sidechains of R162, R266 and R316 from this region results in severely impaired DNA binding[47].

Finally, in contrast to methyl-directed MMR, the eukaryotic MMR initiation is regulated by heterodimeric MutS and MutL homologs, reflecting the functional asymmetry of both MutS subunits. In most other species, except for a few related γ-proteobacteria, MutL homologs possess latent endonuclease activity, removing the necessity for the MutH endonuclease. Furthermore, in these organisms it is not the presence of hemi-methylated GATC sites but the orientation of the β or PCNA replicative DNA polymerase sliding clamp on DNA that directs the MutL endonuclease activity towards the nascent strand during strand discrimination[54,55].

I.3.2 Structural composition and functional importance of the MutS ATPase domain

One of the core components of MutS is the ATPase domain which is involved in regulating many of the characteristic functions of the complex. MutS adopts different active states, mediated by nucleotide binding, hydrolysis and release. This section provides a comprehensive review of the structural composition and functional implications of this domain.

I.3.2.1 The allosteric effect of DNA on nucleotide exchange

It is well established that DNA binding promotes nucleotide exchange, enhances enzymatic activity and that ATP binding induces DNA release, indicating that communication takes place between the N-terminal mismatch binding domains and C-terminal ATPase domains[21,56–58]. Indeed, bulk kinetic measurements and single molecule data revealed a robust allosteric signalling mechanism between the ATPase and DNA binding sites, despite the substantial distance of approximately 70 Å.

The effect of DNA on the switching behaviour of MutS is comparable to that of guanine exchange factors, which toggle G-proteins between the “on” and “off” states. Analogously, DNA acts as allosteric factor which toggles MutS between the ADP-bound mismatch recognition state and the ATP-bound sliding clamp state. Furthermore, bulk kinetic experiments revealed that in the absence of DNA, ADP release is the rate limiting step during the steady-state ATP hydrolysis cycle[44,56,59,60]. Additionally, these experiments showed that DNA significantly enhanced the rate at which ADP is released.

I.3.2.2 Nucleotide binding and hydrolysis

Each MutS subunit contains an ABC motif which combines to create a composite active site upon dimerization. The ATPase domains are asymmetric in nucleotide binding and hydrolysis, consisting of a high affinity (K_D ~ 1 μM) and a low affinity (K_D ~ 30 μM) nucleotide binding site, which communicate

during hydrolysis[38,61]. Additionally, MutS is able to simultaneously bind ATP in one site and ADP in the other[61–63]. Through a combination of rapid quench experiments to measure pre-steady state ATP binding and hydrolysis, and stopped flow experiments to assess phosphate release, it was discovered that free MutS exhibits a fast ATP binding rate (10^6 M^{-1} s^{-1} at 40 ◦C for Taq MutS) and catalyses a burst of hydrolysis of one ATP molecule per dimer (10 s^{-1} at 40 ◦C for Taq MutS) (**Fig. 9**). These findings recapitulate the asymmetric nucleotide binding activity. Subsequent phosphate release is fast, indicating that ensuing steps during the hydrolysis cycle are rate limiting[64].

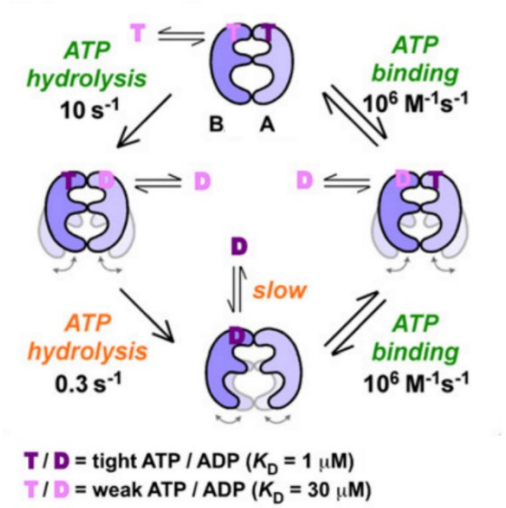

***Figure 9. Model of the ATP hydrolysis cycle in the absence of a mismatch**. Rapid binding of ATP to the high (A) and low (B) affinity sites results in the closure of the clamp domains, rendering MutS incapable of loading onto DNA. Subsequently, there is fast and slow hydrolysis of ATP at the high and low affinity sites, respectively. ADP dissociates from A, while in B ADP species accumulate in steady state, wherein the clamp domains can open. Adapted from Hingorani 2016[64].*

Moreover, MutS undergoes rapid conformational changes, transitioning between "open" and "closed" states, upon binding ATP to both subunits and upon ATP hydrolysis at the high affinity nucleotide binding site, respectively[15,65]. Complementary sm-FRET data further indicate that MutS forms a closed clamp when bound to ATP, which reverts upon hydrolysis and nucleotide release. These findings are supported by genetic analysis showing that mutations targeting highly conserved residues involved in allosterically linking these distant sites are found in patients with Lynch Syndrome[66]. Collectively this indicates that communication takes place between the distant mismatch binding and ATPase domains located at opposing ends of the complex[2,58,67].

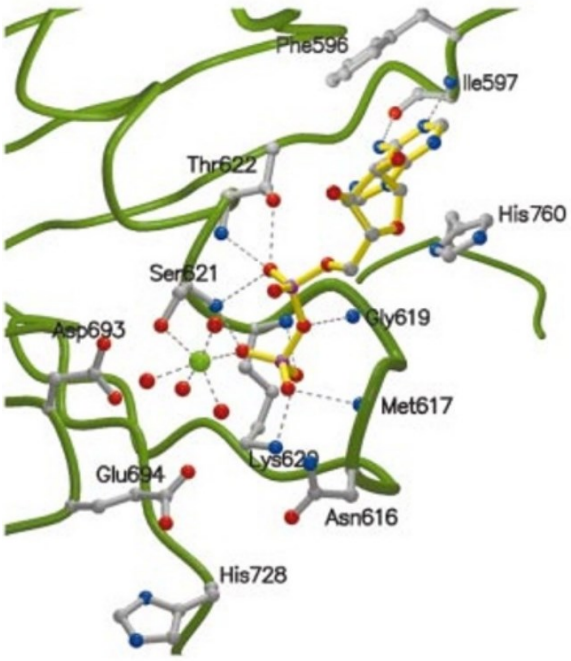

***Figure 10**. Stereo view of the active site of the MutS ATPase domain bound to ADP (yellow) as determined by X-ray crystallography. ADP-contacting residues are shown in grey, Mg^{2+} is shown in bright green and MutS in dark green. Taken from Lamers et al. 2000[68].*

Nucleotides are bound in the classical P-loop mode. Adenine specificity is conferred by the main-chain atoms of I597 which forms two hydrogen bonds with the adenine group, binding of which is further stabilized by π-stacking between H760 and F596. Additionally, the phosphate tail is bound by the Walker A motif (residues 614-622), in specific by D616, K620 and T622 (**Fig. 10**)[15,68].

The primary role of the highly conserved C-terminus Walker B motif (D-E-x-x, residues 693-696) is to catalyse the ATP hydrolysis cycle. Specifically, the

Walker B motif is predominantly involved in stabilization of the magnesium-bound water molecules. The aspartic acid residue present in this motif (D693) coordinates two of the water molecules present in the hydration shell of the catalytic magnesium ion (**Fig. 11**). Furthermore, the adjacent glutamate (E694) is also involved in coordination of the hydration shell and is thought to catalyse ATP hydrolysis by destabilisation of the β-γ phosphate bond of ATP[21,56,68]. These findings were supported by mutational analysis, showing that these carboxylates (D693 and E694) are imperative for ATPase activity[12,21,22]. For example, substitution of E694 for an alanine residue (E694A) almost completely abolishes all ATPase activity, decreasing the maximal steady-state hydrolysis velocity by about two orders in magnitude from ~2 min^{-1} to ~0.02 min^{-1} [21,56,57,69,70].

Furthermore, H728 may act as catalytic base during hydrolysis[21]. Based on the nucleotide state of the protein this residue either points away or towards the bound nucleotide (**Fig. 11**). Moreover, the equivalent of H728 in Rad50 (also an ABC ATPase) is thought to activate a water molecule to perform nucleophilic attack on the γ-phosphate of ATP and this finding was corroborated by recent quantum mechanical modelling of the ABC transporter HlyB[71,72]

Coordination of the catalytic magnesium ion is achieved by six ligands in an octahedral geometry: the β-phosphate of ADP, the hydroxyl group of S621 and four water molecules (**Fig. 11 A and C**). When ATP instead of ADP is bound, the γ-phosphate replaces one of the ordered water molecules from the hydration shell (**Fig. 11 B and D**). As exemplified by mutants deficient in magnesium chelation, such as $MutS^{D693V}$, which were shown to be severely affected in ATPase activity[56]. The mutational analysis of the active site carboxylates (D693 and E694) underscores the delicate balance of electrostatic forces on mediating the conformational transitions by affecting nucleotide binding, hydrolysis and release.

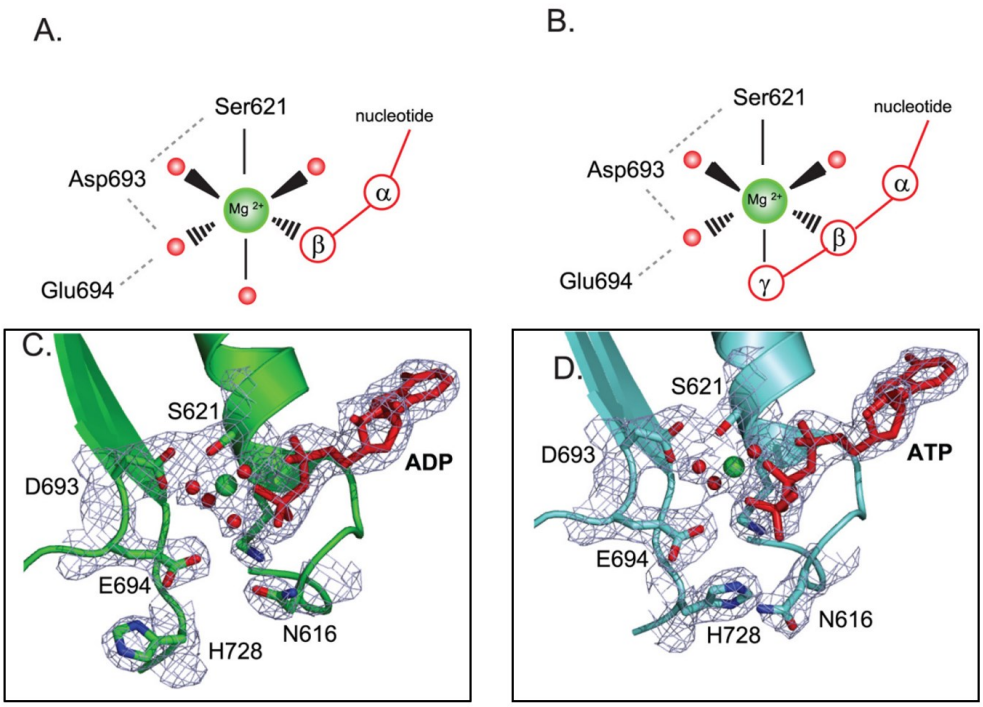

***Figure 11**. Schematic representations of the active site showing the coordination of the hydration shell of the catalytic magnesium ion in the ADP (**A**) and ATP (**B**) bound states accompanied by the corresponding three dimensional structures (**C and D**), respectively. Adapted from Lebbink et al. 2010[56].*

Furthermore, binding of ATP induces local structural rearrangements in the ATPase domain. The positively charged helix-dipole, deposited via S668, of the signature helix and loop of the opposing monomer is pulled towards the incoming ATP molecule by electrostatic attraction of the negatively charged y-phosphate (**Fig. 12**). This results in formation of a closed composite active site which is thought to enable rapid ATP hydrolysis. Moreover, cryo-EM structures indicate lower Mg^{2+} occupancy in the active sites of MutS in the ATP:ADP bound state compared to the state in which both sites are occupied by ATP[15]. In addition, in the ATP:ADP bound state the signature motif (GxSTF, residues 666–670) is more distant from the nucleotide compared to the ATP:ATP bound state. These observations may account for the biphasic ATP hydrolysis, where there is an initial burst followed by a slower steady state hydrolysis rate, observed in stopped-flow experiments[20,61]. This is because the ATP:ADP state appears to be less favorable for hydrolysis than the ATP:ATP state.

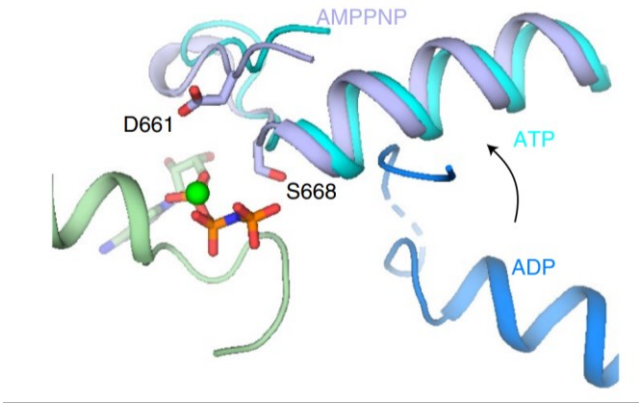

***Figure 12**. Upon ATP binding the composite active site is formed by electrostatic attraction of the positively charged signature helix (blue ADP-bound state, cyan ATP-bound state) from the opposing monomer by the incoming ATP molecule (shown as sticks), resulting in a structural rearrangement towards the nucleotide. Adapted from Borsellini et al. 2022[15].*

2

Materials and Methods

M.1 Materials

M.1.1 Site-directed mutagenesis of the wildtype mutS gene to obtain mutS E694D and E694Q. To obtain mutants, site-directed mutagenesis, Dpn I digestion of the amplification products and transformation of XL10-Gold Ultracompetent Cells was performed using the Agilent technologies QuikChange XL Site-Directed Mutagenesis Kit (Cat. No. 200516), according to the manufacturer's instructions (**see appendix for primer sequences**). Prior to transformation of the XL10-Gold Ultracompetent Cells the amplification products were gel purified to eliminate undesirable reaction products and oligonucleotides using the Promega Wizard SV Gel and PCR Clean-Up system (Cat. No. A9282), according to the manufacturer's instructions. Following mutagenesis, minipreparation of plasmid DNA was performed and the presence of desired mutations was sequence verified using suitable sequencing primers (**see appendix**). After sequence verification, the purified DNA was transformed into *E. coli* DH5α cells and a midipreparation of plasmid DNA was performed. Following midipreparation, the entire open reading frame was sequence verified. Subsequently, the sequence verified DNA was stored at -20 °C until use.

*M.1.2 Purification and preparation of MutL, MutH and MutH$^{156C\text{-}AF647}$***.** Wildtype MutL, MutH and a single-solvent-exposed-cysteine MutH variant (MutH156C) were purified as described before[26,56,73,74]. Concentrations were determined as described elsewhere[75]. Subsequently, MutH156C was diluted to 50 µM in buffer (10 mM HEPES-KOH pH 8.0, 1 mM EDTA, 500 mM KCl, 10% glycerol) and labelled using a 3-fold molar excess Alexa Fluor® 647 (AF647, Invitrogen) for 30 min on ice. Following labelling, excess dye was removed using a Zeba Desalt Spin column 7K (Thermo Scientific™, Cat. No. 89882) and the degree of labelling (99%) was determined by absorbance spectroscopy.

M.2 MutS production and purification

This section described the step by step protocol used to induce protein production and purify MutS using a combination of precipitations and chromatography techniques.

M.2.1 Electrophoresis using 8% Sodium dodecyl-sulphate polyacrylamide gel (SDS PAGE). To generate an 8% SDS PAGE gel, a separating solution was made (8% Acrylamide/Bis-acrylamide mix (37.5:1), 375 mM Tris pH 8.8, 0.1% sodium dodecyl-sulphate (SDS), 0.125% ammonium persulphate, 0.06% N,N,N',N'-Tetramethyl ethylenediamine) and poured between two 1.5 mm glass plates. To even out the surface, 1 ml isopropanol was added on top of the separating solution. Next, the gel was left at room temperature for ~30 min to polymerize, after which the isopropanol was removed. Subsequently, a 5% stacking solution was made (5% Acrylamide/Bis-acrylamide mix (37.5:1), 125 mM Tris pH 6.8, 0.1% SDS, 0.125% ammonium persulphate, 0.1% N,N,N',N'-Tetramethyl ethylenediamine) and poured on top of the separating gel. After polymerisation of the stacking gel for ~30 min at room temperature, the SDS PAGE gel was either directly utilized or stored at 4 °C.

Samples were diluted in phosphate-buffered saline (PBS) to reach an approximate level of 100 mAU based on the chromatographic profiles. Subsequently, an equal volume of Laemmli buffer (4% SDS, 20% glycerol, and 120 mM Tris pH 6.8) was added to the diluted samples. The samples were subsequently heated for 5 min in boiling Milli-Q water, and 20 µl of the resulting solution was loaded onto SDS-PAGE gels. Electrophoresis of gels was performed in electrophoresis buffer (200 mM glycine, 25 mM Tris, 3.5 mM SDS) at 70 V until the samples migrated from the stacking gel into the separating gel (~20 min). Subsequently, the voltage was raised to 170 V, and the electrophoresis continued for an additional 1.5 h. Following electrophoresis, the gel was subjected to a series of washing steps using Milli-Q consisting of microwave-assisted heating at 900 Watt for 30 s, followed by incubation on an

orbital shaker for 5 min. This sequence was repeated thrice to effectively eliminate SDS. Finally the gels were stained using methanol-free colloidal Coomassie blue (0.8% w/v Coomassie Brilliant Blue G-250, 0.35% v/v fuming HCl), according to published protocol[76].

M.2.2 Production and harvest of $MutS^{E694D}$, $MutS^{E694Q}$ and $MutS^{Wt}$. To obtain colonies producing the desired proteins, 100 ng sequence verified plasmid DNA coding for $MutS^{E694D}$, $MutS^{E694Q}$ or $MutS^{Wt}$ was transformed into *mutS* deficient *E. coli* BL21(DE3) pLysS,mutS:Tn10 cells (kind gift from Nora Goosen) by heat shocking the cells at 42 °C for 90 s, incubating on ice for 2 min and supplementing 450 µL Super Optimal Broth (SOC) medium. Subsequently, the cells were incubated at 37 °C for 1 h whilst shaking and plated on Luria-Bertani (LB) agar with 50 µg ml^{-1} ampicillin (AMP) and 34 µg ml^{-1} chloramphenicol (CAM). After overnight incubation at 37 °C all colonies were scraped from the plates and pre-cultured in six flasks containing 50 ml pre-warmed LB agar, 50 µg ml^{-1} AMP and 34 µg ml^{-1} CAM at 37 °C for 1 h. Each pre-culture was then supplemented to 1 l of pre-warmed LB agar, containing 50 µg ml^{-1} AMP and 34 µg ml^{-1} CAM, and grown at 37 °C to an OD_{600} of ∼0.5. Subsequently, the cultures were induced with a final concentration of 1 mM isopropyl 1-thio-β-d-galactopyranoside (IPTG) for ∼4 h at 25 °C. Following induction, the cells were harvested at 4,500 RPM for 15 min at 4 °C (Avanti centrifuge, JLA-8.1000 rotor). Finally, the cell pellets were flash-frozen in liquid nitrogen and stored at -80 °C.

M.2.3 Cell lysis. Harvested cell pellets were resuspended in lysis buffer (25 mM HEPES KOH pH 7.5, 100 mM KCl, 5 mM EDTA, 1 mM phenylmethylsulfonyl fluoride (PMSF), 1 mM DL-Dithiothreitol (DTT) and 1 tablet/50 ml cOmplete™ EDTA-free Protease Inhibitor Cocktail (Roche Diagnostics GmbH, Mannhein, Germany Cat. No. 11873580001)) and lysed by sonification on ice water. Following sonification the lysate was spun down at 18,000 RPM for 45 min at 4 °C (Avanti centrifuge, JLA-30.50 rotor).

M.2.4 Streptomycin sulphate precipitation. To the cell lysate a 25% w/v streptomycin sulphate solution was slowly supplemented whilst stirring on ice, to a final concentration of 5% w/v, to precipitate unwanted oligonucleotides. Following addition of streptomycin, the reaction was slowly stirred on ice for 15 min. Subsequently, the reaction was spun down at 4,000 RPM for 15 min at 4 °C (Eppendorf, Cat. No. 5811000015). Afterwards the supernatant was collected and stored at 4 °C.

M.2.5 Ammonium sulphate precipitation. To precipitate MutS the supernatant collected after streptomycin sulphate precipitation was subjected to an ammonium sulphate precipitation by slowly supplementing a saturated ammonium sulphate solution, drop by drop, while stirring on ice continuously. The volume of the saturated ammonium sulphate solution added was equal to 52% of the volume of the supernatant (**see M.2.4**). Subsequently, the reaction was slowly stirred on ice for 25 min. Afterwards, the solution was spun down at 4,000 RPM for 25 min at 4 °C (Eppendorf, Cat. No. 5811000015). After draining the pellet, it was redissolved in 6 ml GF1 buffer (25 mM HEPES-KOH pH 7.5, 150 mM KCl, 5 mM EDTA, 0.1 mM PMSF, 1 mM DTT). Subsequently, the redissolved pellet was spun down at 4,000 RPM for 3 min at 4 °C (Eppendorf, Cat. No. 5811000015). Afterwards the supernatant was filtered through a 0.22 µm Whatman® Puradisc cellulose-acetate syringe filter (Cytiva, Cat. No. 10462200).

M.2.6 Size exclusion chromatography. To separate protein aggregates and other unwanted proteins from MutS size exclusion chromatography was conducted using the HiLoad® 26/600 or 16/600 Superdex® 200 gel filtration chromatography column (Cytiva, Cat. No. GE28-9893-36 and GE28-9893-35, respectively) operated by an ÄKTA PURE (Cytiva). Prior to use the column was equilibrated overnight with GF1 buffer (**see M.2.5**). Subsequently, the filtered supernatant obtained after ammonium sulphate precipitation was loaded onto the column and eluted using GF1 buffer. Following affinity chromatography using the HiTrap Heparin HP column (**see M.2.8**) the eluate was purified again

by gel filtration chromatography using GF2 buffer (1 M HEPES-KOH pH 7.5, 250 mM KCl, 1 mM DTT). Elution was monitored at wavelengths of 260 and 280 nm.

M.2.7 Anion-exchange chromatography. Following gel filtration the eluted fractions of interest were pooled and loaded on a HiTrap® Q High Performance anion-exchange chromatography column (Cytiva, Cat. No. 17-1154-01) operated by an ÄKTA PURE (Cytiva), which had first been equilibrated with buffer QH1 (25 mM HEPES-KOH pH 7.5, 100 mM KCl, 5 mM EDTA, 0.1 mM PMSF, 1 mM DTT). The column was then washed with five column volumes (25 ml) buffer QH1. Subsequently all bound protein was eluted using ten column volumes of gradually applied high salt buffer QH2 (25 mM HEPES-KOH pH 7.5, 1 M KCl, 5 mM EDTA, 0.1 mM PMSF, 1 mM DTT). Elution was monitored at wavelengths of 260 and 280 nm.

M.2.8 Affinity chromatography. Next, the fractions of interest eluted during anion-exchange chromatography were pooled and diluted using dilution buffer (25 mM HEPES-KOH pH 7.5, 5 mM EDTA, 0.1 mM PMSF, 1 mM DTT) to 100 mM salt calculated based on the conductivity of the eluted fractions compared to that of buffer QH1 (**see M.2.7**). The sample was then injected onto a HiTrap Heparin HP affinity chromatography column (Cytiva, Cat. No. 17-0407-03) operated by an ÄKTA PURE (Cytiva), which was equilibrated using buffer QH1 prior to loading of the sample. Subsequently, the column was washed with five column volumes (25 ml) buffer QH1 and all bound protein was eluted using ten column volumes of gradually applied high salt buffer QH2 (**see M.2.7**). Elution was monitored at wavelengths of 260 and 280 nm.

M.2.9 Concentrating and storage. Following the final gel filtration column, fractions of interest were pooled and concentrated at 4 °C using either a Vivaspin® 6 or Vivaspin® 20 (depending on the sample volume) centrifugal concentrator with a molecular weight cut-off of 10 kDa. Prior to use the concentrator was equilibrated using GF2 buffer (**see M.2.6**). To determine the final concentration the A_{280} was measured using a Nanodrop™ 2000/2000c Spectrophotometer (Thermo Scientific™, Cat. No. ND2000CLAPTOP). The concentration was calculated according to the Lambert-Beer law, using ε = 73,230 $M^{-1}cm^{-1}$ as molar extinction coefficient of MutS. After determining the concentration, the protein was flash-frozen in liquid nitrogen and stored at -80 °C.

M.3 Colorimetric ATPase assay

M.3.1 Preparation of ATPase assay reagents. To obtain an ammonium heptamolybdate-malachite green solution, an ammonium heptamolybdate in 3.5 normality hydrochloric acid solution was prepared by diluting 34.5 ml of 37% concentrated hydrochloric acid (Sigma-Aldrich, Cat. No. 258148) in 90 ml Milli-Q, dissolving 4.2 g (4.2% w/v) ammonium heptamolybdate tetrahydrate (Sigma-Aldrich, Cat. No. A7302) in this mixture and diluting it to 100 ml using Milli-Q. Subsequently, a well stirred malachite green solution was obtained by dissolving 90 mg N,N,N′,N′-Tetramethyl-4,4′-diaminotriphenylcarbenium oxalate (Malachite green-oxalate salt, Sigma-Aldrich Cat. No. M6880) in 200 ml Milli-Q (0.045% w/v). Finally, the ammonium heptamolybdate solution and malachite green-oxalate solution were mixed in a 1:3 ratio and stirred for ∼1-2 H. Afterwards the solution was filtered through a 0.22 µm Whatman® Puradisc cellulose-acetate syringe filter (Cytiva, Cat. No. 10462200) and stored at 4°C in the dark. Just before use 0.01% Tween-20 was supplemented to prevent sedimentation of the phosphomolybdate-dye complexes during experiments. Additionally, a 34% w/v trisodium citrate dihydrate solution (Sigma-Aldrich, Cat. No. 71406) was prepared by dissolving 17 g in 50 ml Milli-Q.

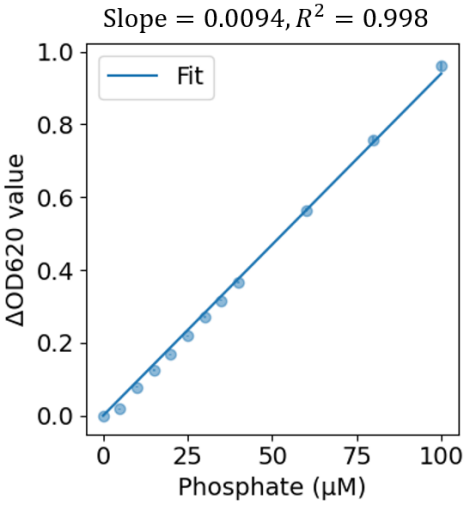

Figure 13. Exemplary phosphate standard curve. *Background corrected absorbance at 620 nm (ΔOD620) is plotted for a range of ATP concentrations. Data is represented as mean ± std, N=4.*

M.3.2. Spectrophotometric determination of the phosphomolybdate-malachite green complex. Spectrophotomeric determination of the phosphomolybdate-malachitte green complexes was conducted in a 96-well microplate format (Thermo Scientific™, Cat. No. 266120). Reactions containing 30 µl wildtype or mutant MutS in assay buffer A (**see M.7.1**) or buffer (no enzyme control) were initiated by supplementing 10 µl ATP or buffer (no ATP control) such that the final concentrations of enzyme (monomer concentration) and ATP became as specified. In order to determine the nucleotide binding affinity steady-state ATP hydrolysis was monitored as a function of ATP concentration (0-1 mM). All reactions were conducted at 22 °C unless otherwise stated.

To determine the amount of phosphate and terminate the reactions, each of the 40 µl reactions were quenched at indicated timepoints using 200 µl ammonium heptamolybdate-malachite green reagent, containing 0.01% Tween-20 (**see M.3.1**). Exactly 2 min after quenching the reactions, trisodium citrate was supplemented to neutralize the pH, thereby preventing spontaneous ATP hydrolysis. Following neutralization the reactions were allowed to develop for 35-50 min at room temperature and the optical density at 620 nm was measured using a SpectraMax iD3 Multi-Mode Microplate Reader (Avantar VWR, Cat. No. 75886-128).

To determine the amount of phosphate based on the absorptivity of the reactions a 1 mM phosphate standard was prepared by dissolving 0.68045 g monobasic potassium phosphate powder (Sigma-Aldrich, Cat. No. P0662) in 5 L using glassware which was thoroughly rinsed with Milli-Q prior to use, to remove any residual detergents which may be a source of phosphate contamination. From the 1 mM phosphate standard serial dilutions in Milli-Q were made spanning a range of 0-100 µM (0, 5, 10, 15, 20, 25, 30, 35, 40, 60, 80, 100 µM). Standard curves were prepared in triplicate to account for intraexperimental variation. Subsequently, the 40 µl standard reactions were quenched and developed using 200 µl ammonium heptamolybdate-malachite green reagent containing 0.01% Tween-20 and 24 µl sodium citrate which was supplemented exactly 2 min later. Subsequently, the amount of phosphate in samples of interest was calculated according to the standard curve which was fitted by a first order linear equation after background subtraction (**Fig. 13**). Furthermore, to account for variability within the experiment, each experiment was conducted in duplicate and to account for interexperimental variation all experiments were conducted in at least triplicate on different days.

M.3.3. Quantification and data analysis. To determine the maximum steady-state ATP hydrolysis velocity (V_{max}) and the substrate affinity (K_m) of mutant or wildtype MutS, steady-state ATP hydrolysis velocities were determined over a range of ATP concentrations and the data was fitted according to Michaelis-Menten kinetics **Eq. (1).** The steady-state ATP hydrolysis velocities were calculated by linearly fitting the amount of spectrophotometrically determined phosphate produced over time normalized to the amount of protein (**see M.3.2.**). All data analysis was done using in Python 3.8 (with analysis libraries Numpy 1.19.0, Scipy 1.5.0, Pandas 2.0.0 and Matplotlib 3.7.1).

$$v([ATP]) = \frac{V_{max}[ATP]}{K_m + [ATP]} \quad (1)$$

M.4 Preparation and purification of Alexa Fluor® 647-labelled and unlabelled circular DNA constructs.

The preparation of the circular DNA constructs utilized as substrate during FRET and *in vitro* nicking assays (**see R.3**) can be divided into four steps: primer phosphorylation, primer annealing, primer extension and ligation, and finally gel purification. Below, the step-by-step protocol for preparation of the construct is described. During the preparation of fluorescently labelled DNA constructs (GT#1^{AF647} and AT#1^{AF647}) the reaction was covered in tin foil at all times to prevent the fluorophores from photobleaching.

M.4.1 Primer phosphorylation. The primer of interest (GT14^{AF647}, GT14, AT14^{AF647} or AT14, **see Appendix**) was phosphorylated in a T4 polynucleotide kinase reaction (6 µM primer, 10x T4 Polynucleotide Kinase Reaction Buffer (Roche diagnostics, Cat. No. 54069200), 20 U/µl T4 polynucleotide kinase (Roche diagnostics, Cat. No. 10174645001), 1 mM ATP) for 1 h at 37 °C. Afterwards the reaction was incubated at 70 °C to heat inactivate the T4 polynucleotide kinase. Subsequently, the reaction was cooled for 10 min on ice and stored at 4 °C.

M.4.2 Primer annealing. Following primer phosphorylation the phosphorylated primer of interest was annealed on ssDNA derived from phagemids GATC1 as described[52,75,77]. To anneal the primer to the ssDNA substrate, 60 µg ssDNA was combined with 120 pmol phosphorylated primer in T4 polymerase buffer (50 mM Tris, 15 mM $(NH_4)_2SO_4$, 7 mM $MgCl_2$, 0.1 mM EDTA, 10 mM β-mercaptoethanol, 0.02 mg/ml BSA, pH 8.8), heated for 6 min at 85 °C and left to slowly cool down overnight at room temperature.

M.4.3 Primer extension and ligation. After primer phosphorylation and annealing (**see M.4.1 and M.4.2**) the primer was extended and the resulting dsDNA product ligated in a primer extension/ligation reaction, containing 1 mM dNTP's, 1 mM ATP, 1 U T4 ligase and 30 U T4 polymerase in T4 polymerase buffer, for 3 h at 37 °C. Subsequently, the reaction was incubated at 70 °C for 20 min to heat inactivate the enzymes and stored at 4 °C.

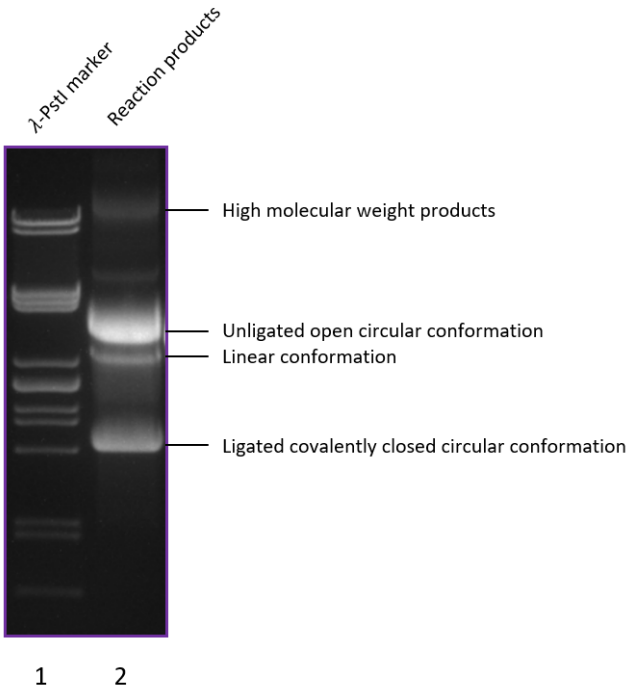

M.4.4 Gel purification. The product obtained after primer extension and ligation (**see M.4.3**) was checked by gel electrophoresis on a 0.8% agarose gel, containing 1 µg/ml ethidium bromide, for 2.5 h at 100 V using a λ-PstI DNA marker as reference (**Fig. 14**). Samples from the bulk were run on adjacent lanes and visualized by UV light in order the locate the ligated product for excision. The ligated product was then excised and gel purified using the Wizard® SV Gel and PCR Clean-Up System (Promega, Cat. No. A9281), according to the manufacturer's instructions. The final

concentration was measured using a Nanodrop™ 2000/2000c Spectrophotometer (Thermo Scientific™, Cat. No. ND2000CLAPTOP) and the purified DNA was stored in the dark at 4 °C.

***Figure 14**. Exemplary 0.8% agarose gel showing the different reaction products obtained after primer extension and ligation (**lane 2**). The ligated product was excised from the gel and purified to obtain the ligated covalently closed circular product.*

M.5 Nucleotide exchange

Nucleotide exchange was quantified using MutS-bound Mant-ADP in a 96-well microplate format (Greinder Bio-One, Cat. No. 655076). Reactions contained 2.5 µM wildtype or mutant MutS (monomer concentration) and 1 µM Mant-ADP (Jena Bioscience, Cat. No. NU-201S) in assay buffer A without BSA, to avoid interference from its autofluorescence (25 mM HEPES-KOH pH 7.5, 150 mM KCl, 5 mM $MgCl_2$, 10% Glycerol, 1 mM DTT, 0.005% Tween-20). Optionally, a molar excess of 5 µM 41-bp heteroduplex (41Glow annealed to 41Tup, **see appendix**) or homoduplex (41Alow annealed to 41Tup, **see appendix**) DNA oligonucleotides was added. In some experiments 5 µM 41-bp biotinylated heteroduplex (bio-41Glow annealed to bio-41Tup, **see appendix**) or homoduplex (bio-41Alow annealed to bio-41Tup, **see appendix**) DNA oligonucleotides end-blocked with 10 µM streptavidin tetramer (Thermo Scientific™, Cat. No. 10197673) were ultilized to investigate the effect of DNA ends on nucleotide exchange. After a 5 min incubation at 22 °C nucleotide exchange was initiated by injection of 1 mM ATP. Subsequently, Mant-ADP release was monitored by exciting the reactions at 355 nm and measuring emission at 405 nm at 1 Hz for 5 min using an integration time of 140 ms, 1 mm read height and a medium PMT gain in a SpectraMax iD3 Multi-Mode Microplate Reader (Avantar VWR, Cat. No. 75886-128). A function describing a single exponential decay exponential was fitted to the data in Python 3.8 (with analysis libraries Numpy 1.19.0, Scipy 1.5.0 and Matplotlib 3.7.1) to obtain Mant-ADP release rates. Experiments were conducted in triplicate on different days in order to account for interexperimental variation.

M.6 Surface plasmon resonance

All SPR spectroscopy was performed at 25 °C on a Biacore T100 (Cytiva). To assemble a sensor surface suitable for studying the kinetics of MutS binding to DNA, the equivalent of ~2400 response units (RU) of streptavidine tetramer (Thermo Scientific™, Cat. No. 10197673) was conjugated to the surface of a CM5 chip (Cytiva, Cat. No. BR100530) using an amine coupling kit (Cytiva, Cat. No. BR100050), according to the manufacturer's protocol. 1 RU corresponds to a surface coverage of ~1 µg m^{-2} for a typical protein. Following streptavidin immobilization, 1 nM of 41-bp heteroduplex or homoduplex biotinylated oligonucleotides in HSN buffer (10 mM HEPES-KOH pH 7.5 and 150 mM NaCl) were bound to the streptavidin surface to the equivalent of ~15 RU. The DNA was obtained by annealing ssDNA oligonucleotide bio-41Tup with a 2-fold molar excess of either 41Glow (to create dsDNA with a single GT mismatch) or 41Alow (to create homoduplex dsDNA) overnight after heating for 5 min at 85 °C in 25 mM HEPES-KOH (pH 7.5) and 150 mM KCl, to assure all biotinylated DNA was double stranded (**see appendix for sequences**).

Following sensor surface assembly, wildtype and mutant MutS binding kinetics were studied in the absence or presence of ATP (concentrations for protein (monomer) and ATP as specified) in SPR buffer (25 mM HEPES-KOH pH 7.5, 150 mM KCl, 5 mM $MgCl_2$, 0.05% Tween-20 and 1 mM DTT). Samples were injected with a flow rate of 50 µl min^{-1} and regeneration was achieved by injecting a 0.05% SDS solution

in Milli-Q for 30 s at 50 µl min^{-1}. All data was collected at 10 Hz. Furthermore, exponential fits to the data were obtained using freely available online SPR analysis software (Anabel) and subsequent data analysis was conducted using Python 3.8 (with analysis libraries Numpy 1.19.0, Scipy 1.5.0 and Matplotlib 3.7.1)[79]. Double background normalization was conducted by subtracting signal measured in identical flow cells without immobilized DNA and signal measured upon injecting only buffer. Lastly, all experiments were conducted in triplicate on different days in order to account for interexperimental variation.

M.7 Ensemble MutH activation assays

M.7.1 Strand incision. Strand incision assays were performed with 100 nM wildtype or mutant MutS (monomer concentration), 100 nM wildtype MutL (monomer concentration), 50 nM wildtype MutH, 1 mM ATP and 0.5 nM fluorescently labelled heteroduplex or homoduplex DNA (**GT#1^{AF674} or AT#1^{AF647}, see M.4)** in assay buffer A (25 mM HEPES-KOH pH 7.5, 150 mM KCl, 5 mM $MgCl_2$, 10% Glycerol, 0.1 mg/ml BSA, 1 mM DTT, 0.005% Tween-20). Protein concentrations reflect the assumed minimal stoichiometry of 1 MutS dimer, 1 MutL dimer and 1 MutH monomer. Where indicated, 1 µM 41-bp long heteroduplex linear dsDNA oligonucleotides with biotinylated ends (trap DNA) and 2 µM streptavidin tetramer (Thermo Scientific™, Cat. No. 10197673) were supplemented to prevent "multiple loading" from occurring. The order in which the various DNA substrates and proteins were combined varied depending on the experiment. At indicated timepoints 10 µl samples of the reaction were terminated with an equal volume stop solution (20% glycerol, 1% SDS and 50 mM EDTA). Samples were analysed on a 0.8% agarose gel run in 1x TAE for 16 h at 20 V containing 2 µM chloroquine, covered in tin foil to prevent photobleaching. All reactions were conducted at 22 °C unless otherwise stated. Experiments were conducted in triplicate on different days in order to account for interexperimental variation.

M.7.2 Quantification and data analysis. Progressive strand incision of the AF647-labelled DNA constructs was monitored by using a Typhoon9100 imager (Cytiva) with excitation wavelength fixed at 633 nm and emission collected via the Cy5 670BP30 filter at 100 µm resolution with PMT gain set to 800 V. Subsequently, the intensities of the bands was quantified in FIJI 2.1.0 [78]. The fraction of incised DNA was determined after background subtraction through dividing the band intensity of the nicked DNA by the cumulative signal of un-incised as well as incised DNA, corrected for the intensity of the signal of unconverted substrate present at time equals zero minutes. Data analysis was done in Python 3.8 (with analysis libraries Numpy 1.19.0, Scipy 1.5.0, Matplotlib 3.7.1 and Sklearn 1.2) using **Eq. 3, 4** and **5**.

$$f_1(t) = \alpha(1 - e^{-r_1 t}) + r_2 t \quad (2)^*$$

$$f_2(t) = \frac{L}{1 + e^{-\kappa(t-a)}} \quad (3)$$

$$r = \frac{\ln(2)}{{f_2}^{-1}\left(\frac{L}{2}\right)} \quad (4)$$

$$f_3(t) = \frac{f_{max} * t}{t + t_{\frac{1}{2}}} \quad (5)$$

*Generalised formula, depending on the experiment α and r_2 were fixed.

M.8 Ensemble MutH recruitment assays

M.8.1 MutH recruitment. MutH recruitment was assessed in real-time in a reconstituted MMR reaction containing 100 nM wildtype or mutant MutS (monomer concentration), 100 nM wildtype MutL (monomer concentration) and 50 nM of a fluorescently-labelled single-solvent-exposed-cysteine MutH variant ($MutH^{156C\text{-}AF674}$) and either 1 mM ATP or 0.5 nM unlabelled DNA (**GT#1 or AT#1, see M.4**) stained with 200 nM SYBR Green I (final concentrations) in assay buffer A without BSA, to avoid interference from its autofluorescence (25 mM HEPES-KOH pH 7.5, 150 mM KCl, 5 mM $MgCl_2$, 10% Glycerol, 1 mM DTT, 0.005% Tween-20). The 50 µl reactions were started by injecting an equal volume of either 1 mM ATP or 0.5 nM unlabelled DNA stained with 200 nM SYBR Green I, depending on the experiment. The excitation wavelength was fixed at 485 nm for the SG (donor) and emission was monitored at 680 nm (for $MutH^{156C\text{-}AF647}$, acceptor) to detect energy transfer. Experiments were conducted at 22 °C in a 96-well microplate format (Greiner Bio-One, Cat. No. 655076) using a SpectraMax iD3 Multi-Mode Microplate Reader (Avantar VWR, Cat. No. 75886-128). Data was acquired at 1 Hz for 10 min using an integration time of 140 ms, 10 mm read height and a medium PMT gain. Data analysis was conducted using FIJI 2.1.0 and Python 3.8 (with analysis libraries Numpy 1.19.0 and Matplotlib 3.7.1). Experiments were conducted in triplicate on different days in order to account for interexperimental variation.

M.8.2 Endpoint MutH activation. In addition to MutH recruitment, endpoint MutH activation was determined by terminating 10 µl samples taken from each reaction after measuring FRET with an equal volume of stop solution (**see M.7.1**). Subsequently, the samples were analysed on a 0.8% agarose gel containing 2 µM chloroquine run in 1x TAE for 16 h at 20 V. Following gel-electrophoresis, gel slices of interest were incubated in 100 mL 1X TAE containing 10000x diluted SYBR Gold (Invitrogen™, Cat. No. S11494) for 40 min on an orbital shaker to stain the DNA. Next, the gel slice was imaged by scanning the fluorescence of the SYBR Gold DNA intercalator using a Typhoon9100 imager (Cytiva) with CY2 settings and PMT 550 V at 100 µm resolution.

3

Results

Protein purifications

R.1. Purification of MutS^{Wt}, MutS^{E694Q} and MutS^{E694D} from mutS deficient E. coli BL21(DE3)pLysS,mutS:Tn10

In this section the procedure to obtain purified MutS is described (**Fig. 15**). This is a well-established protocol which has been followed many times to generate a number of MutS mutants over the years[13,15,26,56,68,69]. First mutagenesis was performed on the wildtype vector to obtain vectors coding for the MutS mutants, which were subsequently sequence verified and transformed into *mutS* deficient *E. coli* BL21(DE3)pLysS,mutS:Tn10 cells (kind gift from Nora Goosen). After selection and culturing of the cells, protein production was induced and the cells were harvested. Subsequently, the harvested cell pellets were utilized to obtain purified MutS by a combination of precipitations and chromatographic techniques. To monitor the process and ensure quality control, samples were taken and analysed by sodium dodecyl sulphate polyacrylamide gel electrophoresis (SDS-PAGE) during the entire process. In addition the A_{260}, A_{280}, pH and conductivity were measured during each column purification (**see M.2.1**). Below the results obtained after each step will be discussed. For elaborate details on the exact methodologies see **M.2**. Data from MutS^{E694N} is not shown since it was previously purified in the laboratory in an identical manner.

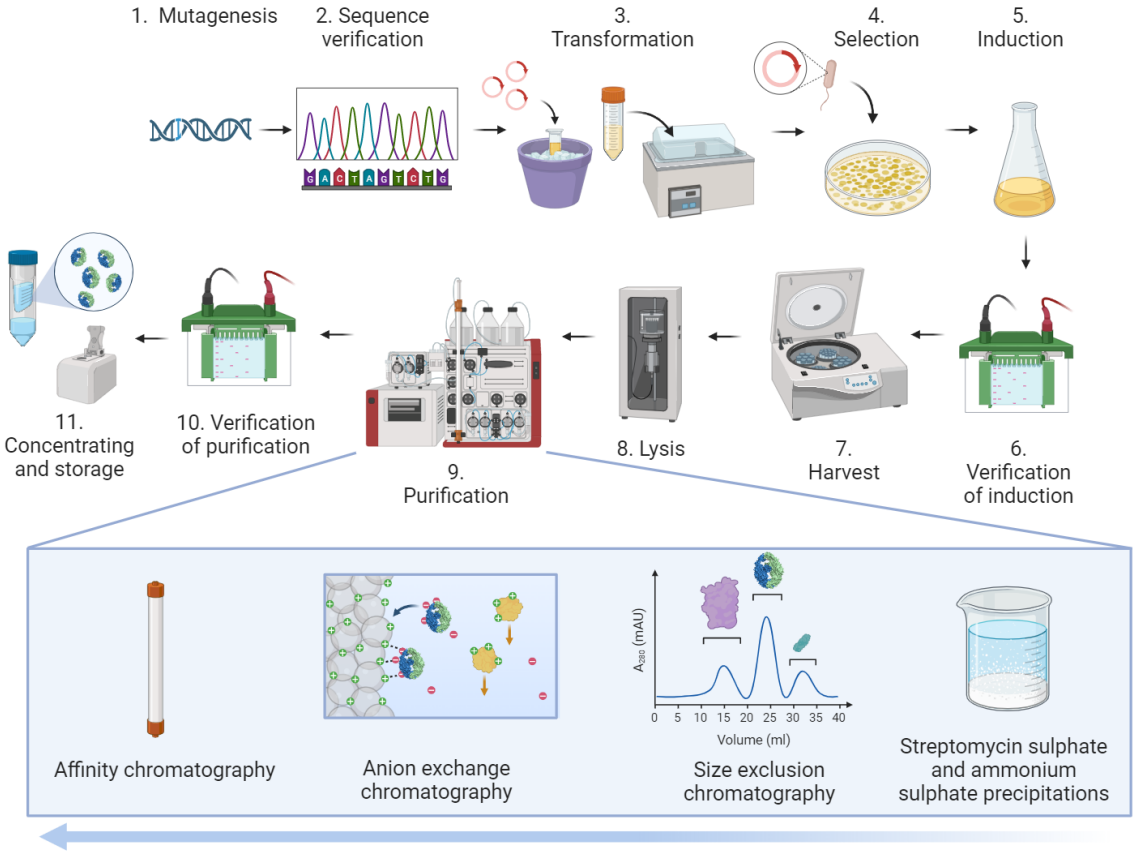

***Figure 15**. Graphical abstract of the MutS purification procedure. Created with BioRender.com.*

R.1.1. Mutagenesis, transformation, induction and harvest

To obtain vectors coding for MutS^{E694Q} and MutS^{E694D} point mutations were introduced in the sequence coding for wildtype MutS by site-directed mutagenesis (**see M.1.1**). Subsequently, the vectors were sequence verified and transformed in *mutS* deficient *E. coli* BL21(DE3)pLysS,mutS:Tn10 cells by heat shocking the bacteria (**see M.2.2**). The vectors contain an ampicillin resistance gene and the *E. coli* BL21(DE3)pLysS,mutS:Tn10 strain is resistant against chloramphenicol, therefore the cultures were grown in the presence of these antibiotics to select only those bacteria which were correctly transformed. Next, protein production was induced during mid-exponential growth phase, as determined by measuring the optical density, by administering 1 mM isopropyl 1-thio-β-d-galactopyranoside (IPTG). Following induction the cells were harvested, flash-frozen in liquid nitrogen and stored at -80 °C. Samples were taken before and after induction and analysed by SDS-PAGE (**see M.2.1**).

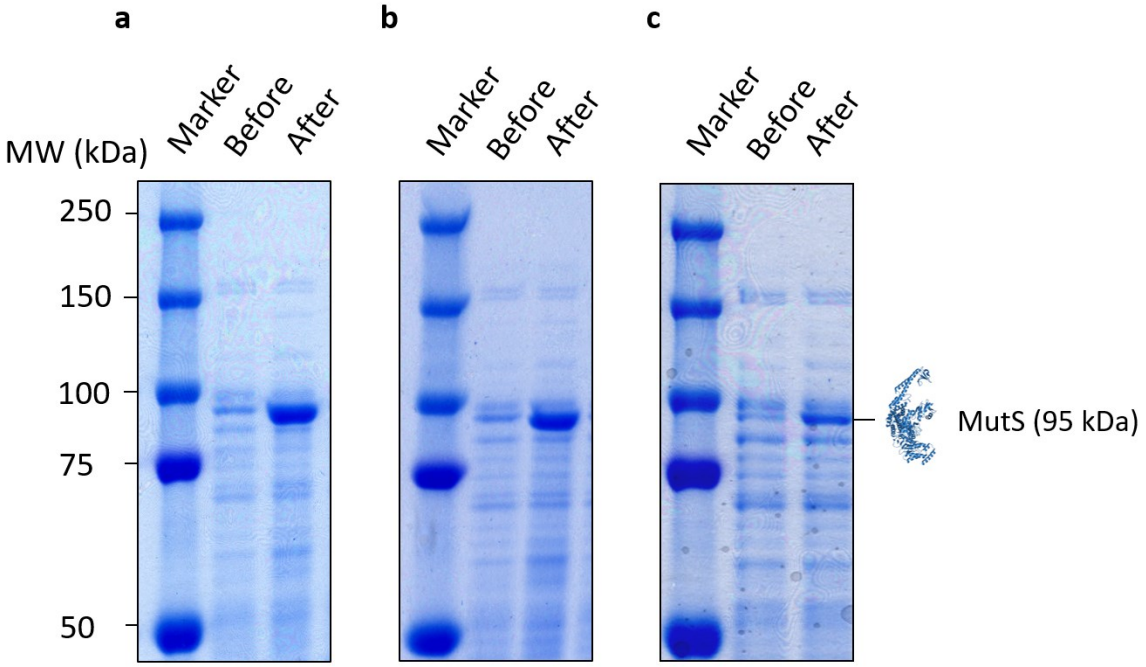

***Figure 16. Induction gels**. After addition of 1 mM IPTG well defined bands appeared on 8% SDS-PAGE gels around 100 kDa, corresponding to the molecular weight of MutS^{E694Q} (**a**), MutS^{E694D} (**b**) and MutS^{Wt} (**c**) as can be seen by comparing the samples taken before (Before) and after induction (After).*

As expected, distinct bands with a molecular weight of approximately 100 kDa, which corresponds to the monomeric form of MutS (95 kDa), were observed after induction (**Fig. 16**). The data collectively demonstrates the successful transformation of mutS deficient *E. coli* BL21(DE3)pLysS,mutS:Tn10 cells with vectors encoding for MutS mutants and wildtype, and successful induction of protein production. Subsequently, the cells were subjected to lysis and purified through a combination of precipitations and chromatographic techniques as outlined below.

R.1.2 Streptomycin and ammonium sulphate precipitations

Next, the cell pellets were thawed, resuspended and sonified to obtain whole cell lysates (**see M.2.3**). It is well known that in bacterial cell extracts nucleic acids significantly interfere with protein isolation and separation. Therefore, the cell lysates were subjected to a streptomycin precipitation, which selectively precipitates nucleic acids, thereby reducing the number of unwanted oligonucleotides (**see M.2.4**)[80]. Samples taken from the cell lysates before (**Fig. 17, input**) and after (**Fig. 17, SM**) streptomycin precipitation did not show a marked difference on SDS-PAGE, indicating that the precipitation did not affect proteins, as expected.

Subsequently, the supernatant was subjected to an ammonium sulphate precipitation to precipitate MutS (**see M.2.5**). At high ionic strength proteins differ markedly in solubility, making it possible to selectively precipitate and isolate proteins of interest by supplementing the right amount of ammonium sulphate, which changes the ionic strength of the solution. MutS was precipitated by supplementing 52% of sample volume of a saturated ammonium sulphate solution. The precipitated proteins were subsequently recovered by resuspending the pellet. Samples were taken from the supernatant (**Fig. 17, AS 1**) and resuspended pellet (**Fig. 17, AS 2**) and analysed by SDS-PAGE. Although many proteins are present in the samples taken from the supernatant after ammonium sulphate precipitation, MutS seems to be absent. Furthermore, in the samples taken from the resuspended pellet MutS is enriched, as expected. Taken together the data indicate that the ammonium sulphate precipitation successfully eliminated unwanted proteins, leading to an increase in purity of MutS.

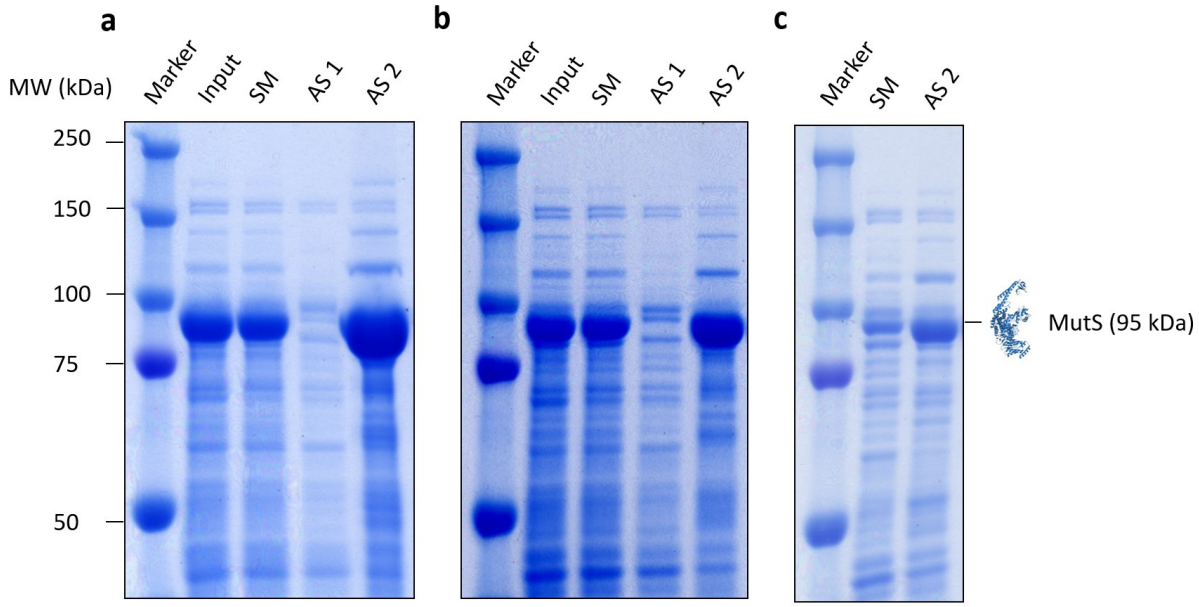

***Figure 17*. *Precipitation gels*.** *SDS-PAGE gels showing samples taken from the whole cell lysates (Input), after streptomycin precipitation (SM) as well as the supernatant (AS 1) and resuspended pellet (AS 2) after ammonium sulphate precipitation. Panels show data acquired during purification of MutS^{E694Q} (**a**), MutS^{E694D} (**b**) and MutS^{Wt} (**c**).*

R.1.3 Chromatography

R.1.3.1. Size exclusion chromatography gel filtration column I

Next, MutS was further purified by size exclusion chromatography (SEC) (**see M.2.6**). The SEC columns are filled with porous microscopic beads through which small molecules are able to manoeuvre, whereas large molecules are not, greatly increasing the pathlength of small particles. Therefore, smaller particles will elute later, resulting in separation by size (**Fig. 18**).

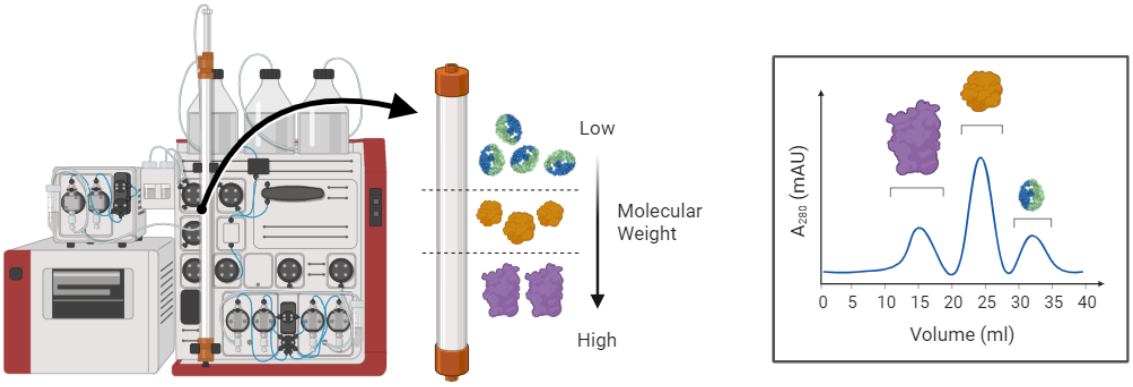

Figure 18. Schematic representation of the SEC principle*. The phenomenon of separation by size occurs as a consequence of the variance in pathlength, wherein larger molecules traverse a shorter distance and therefore elute earlier. Created with BioRender.com.*

In the chromatograms of all three MutS variants four peaks are visible (**Fig. 19, 20 and 21**). The first peak, which is eluted around 0.35 column volumes (CV) in all three chromatograms, is the largest and likely obtained from MutS aggregates. Indeed, samples taken from corresponding fractions were enriched in MutS as shown by SDS-PAGE (**Fig. 19, B8 and Fig. 21, B10**). In addition, the $\frac{A_{260}}{A_{280}}$ ratio for this peak was larger than 1, indicating the presence of unwanted nucleic acids in the eluate.

The second peak, around 0.45 CV, corresponds to the dimeric and tetrameric forms of MutS and was therefore pooled and utilized as input for subsequent purification steps. As expected, samples taken from corresponding fractions were distinctly enriched in MutS (**Fig. 19, C4-D5, Fig. 20, C7-D2 and Fig. 21, C8-D3**).

Trailing behind the two peaks at 0.35 and 0.45 CV is a third, around 0.7 CV, which likely derives from other proteins and small biomolecules. As expected, samples taken from corresponding fractions (**see Fig. 19, F9**) were enriched in small proteins with a molecular weight of ~50 kDa but not in MutS.

Finally the last peak around 0.95 CV co-occurs with a sharp increase in conductivity and a transient drop in pH, indicating that ions are eluted from the column. Except for this transient peak, the pH remained near constant (~7.9) during each run. During all runs the $\frac{A_{260}}{A_{280}}$ ratio was rather high (> 1), indicating that even after the streptomycin precipitation the sample still contains high amounts of nucleic acids which need to be removed during subsequent purifications. However, specifically for the peak corresponding to the dimeric and tetrameric forms of MutS, the $\frac{A_{260}}{A_{280}}$ ratio is smaller than 1, as desired. Taken together the data shows that the first SEC column successfully reduced the number of unwanted oligonucleotides and led to an increase in purity of MutS.

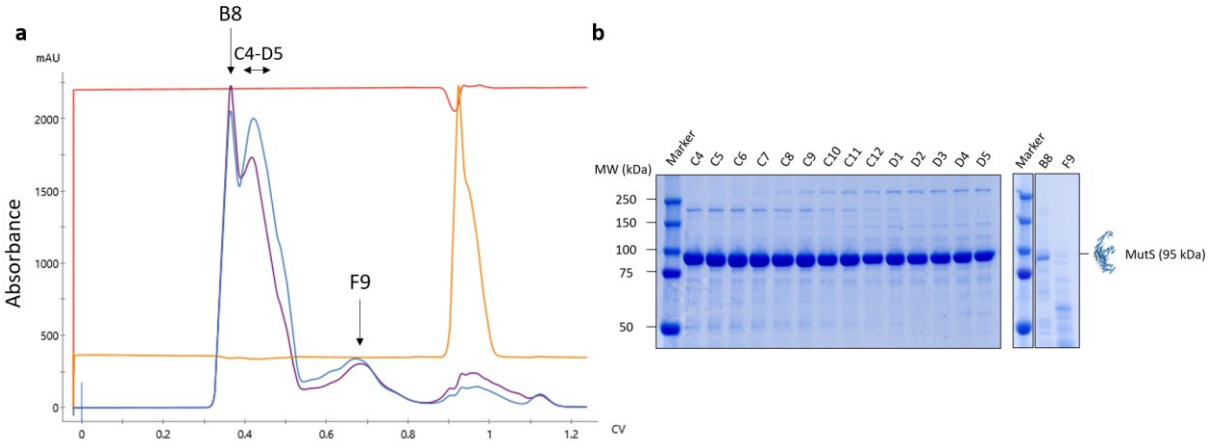

Figure 19. SEC column I purification data MutS^{E694Q}. ***a****, Chromatogram obtained during purification. Y-axis shows absorbance levels A_{260} (purple) and A_{280} (blue). Red and orange lines represent pH and conductivity respectively. Elution volume is expressed in column volumes (CV).* ***b****, SDS-PAGE gels showing samples taken from corresponding fractions in* ***a****.*

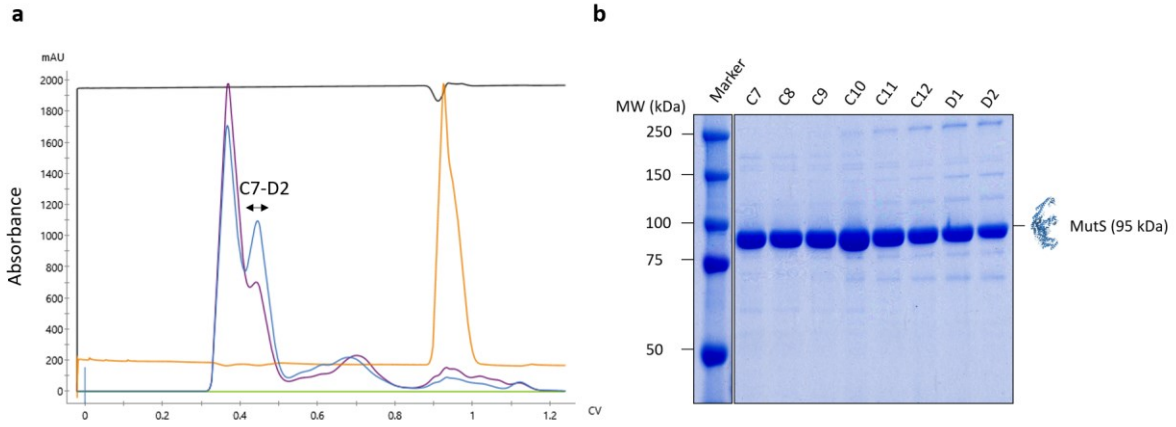

Figure 20. SEC column I purification data MutS^{E694D}. ***a****, Chromatogram obtained during purification. Y-axis shows absorbance levels A_{260} (purple) and A_{280} (blue). Black and orange lines represent pH and conductivity respectively. Elution volume is expressed in column volumes (CV).* ***b****, SDS-PAGE gel showing samples taken from corresponding fractions in* ***a****.*

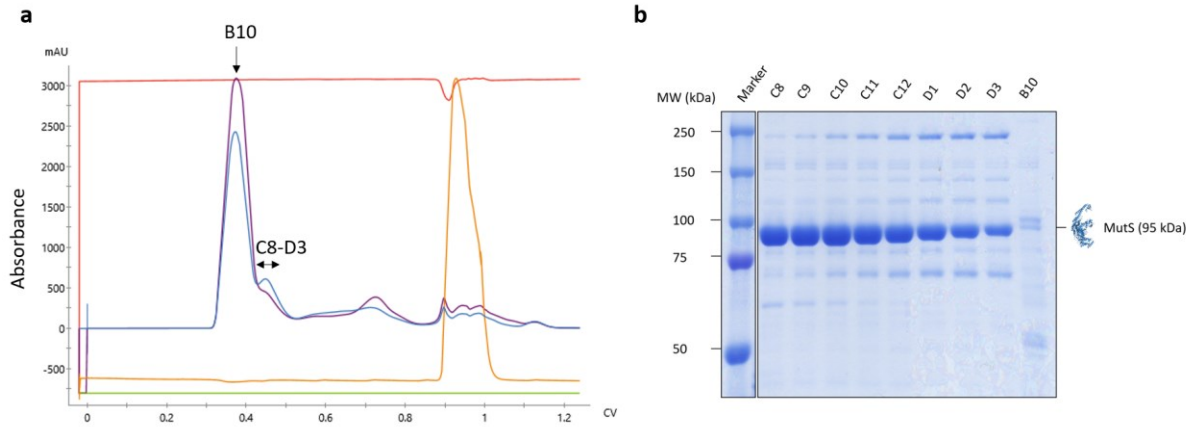

***Figure 21. SEC column I purification data MutS^{Wt}. a**, Chromatogram obtained during purification. Y-axis shows absorbance levels A_{260} (purple) and A_{280} (blue). Red and orange lines represent pH and conductivity respectively. Elution volume is expressed in column volumes (CV). **b**, SDS-PAGE gel showing samples taken from corresponding fractions in **a**.*

R.1.3.2. Anion-exchange chromatography

The pooled fractions of interest obtained after SEC were injected onto an anion-exchange chromatography column to further purify MutS (**M.2.7**). This column contains beads coated with positively charged moieties which constitute the stationary phase such that negatively charged proteins bind to the column, enabling separation based on charge (**Fig. 22**). To elute the proteins a buffer containing a high concentration of KCl (1 M) was gradually injected, resulting in disruption of the electrostatic interaction between the column material and the proteins.

MutS^{Wt} has an overall negative charge at a pH of ~7.9, as determined by the isoelectric point of the protein, which was calculated to be 5.7 based on the peptide sequence using the freely available "ProtParam" bioinformatics tool developed by the Swiss Institute of Bioinformatics. Additionally, the isoelectric point of the mutants is not expected to differ significantly from that of the wildtype. Hence, anion-exchange is an appropriate purification method for both wildtype and mutant MutS, relying on intrinsic properties.

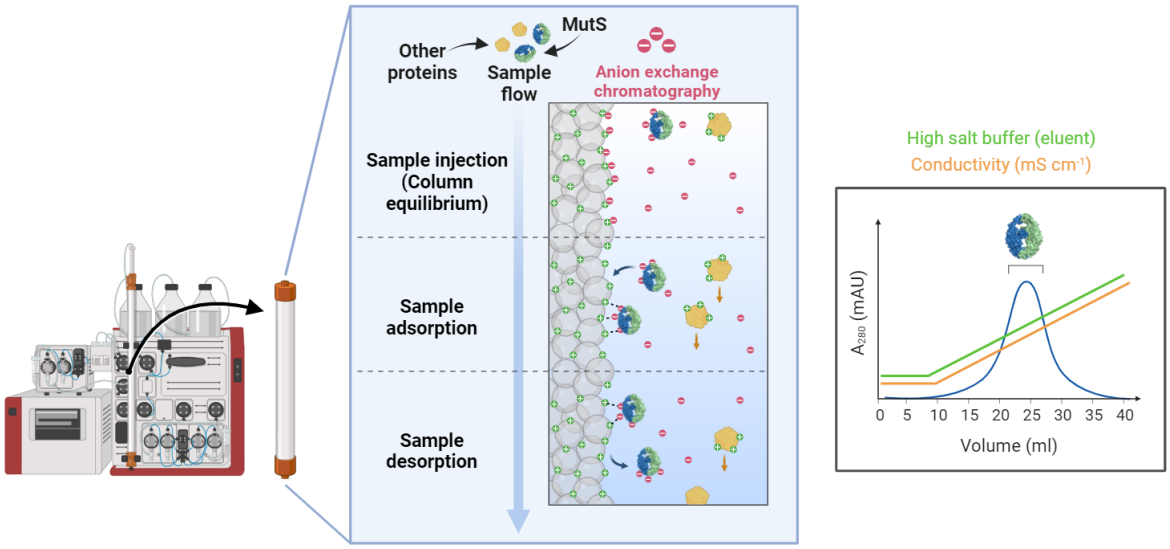

***Figure 22. Schematic representation of anion-exchange chromatography principle.** Beads coated with a positively charged moiety make up the column material and bind negatively charged proteins enabling separation based on charge. Bound proteins are eluted using a high salt buffer. Created with BioRender.com.*

Each chromatogram displays three distinct peaks around 13, 15, and 19 CV. As anticipated, the gradual application of a high salt buffer (1 M KCl) resulted in the elution of MutS, demonstrated by the simultaneous increase in A280 and conductivity (**Fig. 23, 24 and 25**). Samples obtained from corresponding fractions confirmed the presence of MutS through SDS-PAGE analysis. Additionally, the third peak around 19 CV exhibited a significantly larger $\frac{A_{260}}{A_{280}}$ ratio than 1, indicating the elution of nucleic acids.

The fractions corresponding to the second peak, which is eluted around 15 CV, were enriched most in MutS and had an acceptable $\frac{A_{260}}{A_{280}}$ ratio (< 1). Therefore, eluted fractions corresponding to this peak were pooled and utilized as input for subsequent purification steps. Moreover, a variety of proteins other than MutS were present in fractions collected from the flowthrough, indicating that these were successfully removed, resulting in an increase in purity. Collectively the data signifies that MutS was successfully purified by anion-exchange chromatography.

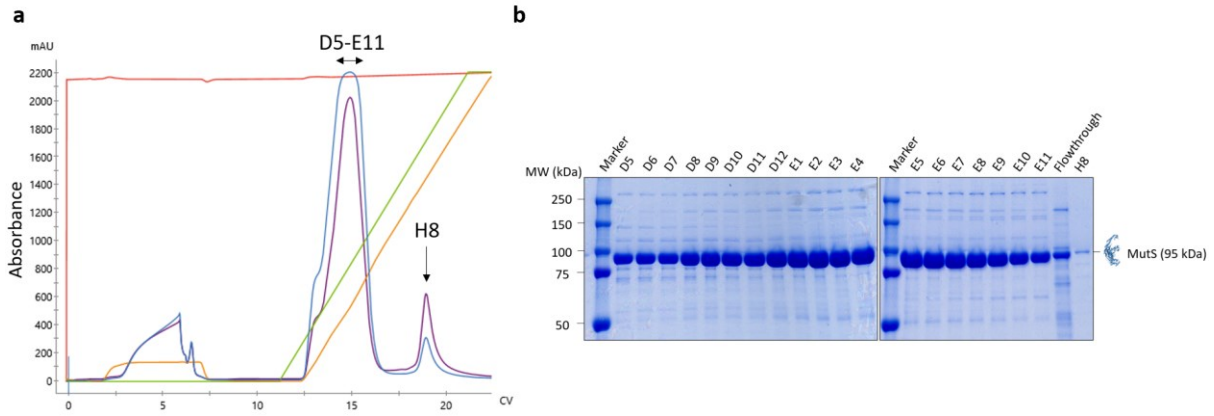

Figure 23. Anion-exchange chromatography purification data MutS^{E694Q}. ***a****, Chromatogram obtained during purification. Y-axis shows absorbance levels A_{260} (purple) and A_{280} (blue). Red, orange and green lines represent pH, conductivity and amount of injected high salt wash buffer, respectively. Elution volume is expressed in column volumes (CV).* ***b****, SDS-PAGE gels showing samples taken from corresponding fractions in* ***a****.*

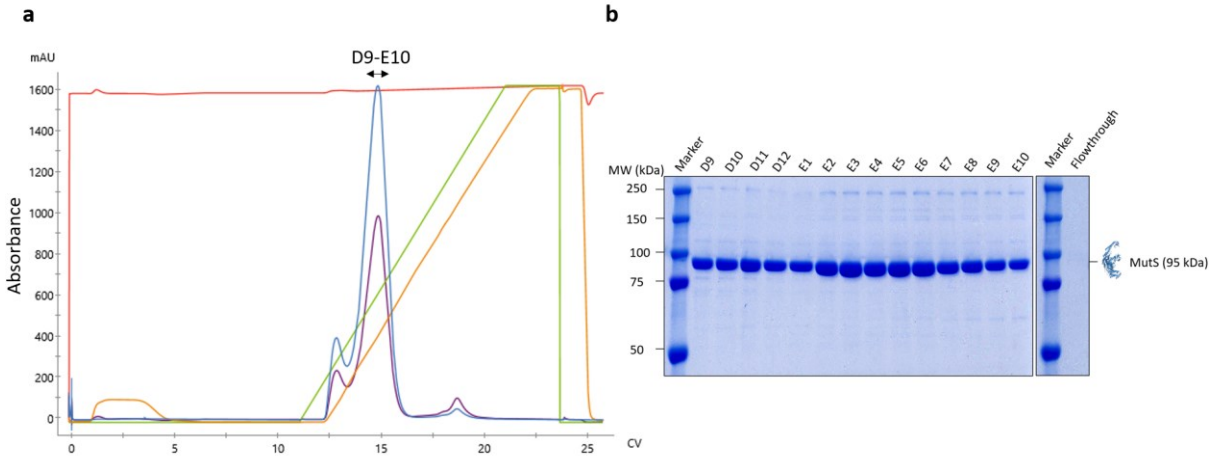

Figure 24. Anion-exchange chromatography purification data MutS^{E694D}. ***a****, Chromatogram obtained during purification. Y-axis shows absorbance levels A_{260} (purple) and A_{280} (blue). Red, orange and green lines represent pH, conductivity and amount of injected high salt wash buffer, respectively. Elution volume is expressed in column volumes (CV).* ***b****, SDS-PAGE gel showing samples taken from corresponding fractions in* ***a****.*

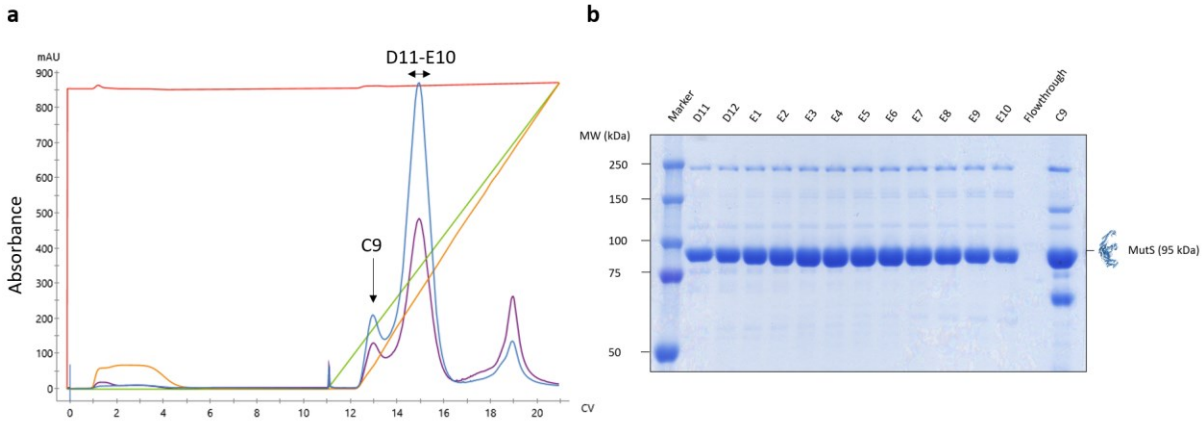

***Figure 25. Anion-exchange chromatography purification data MutS^{Wt}. a**, Chromatogram obtained during purification. Y-axis shows absorbance levels A_{260} (purple) and A_{280} (blue). Red, orange and green lines represent pH, conductivity and amount of injected high salt wash buffer, respectively. Elution volume is expressed in column volumes (CV). **b**, SDS-PAGE gel showing samples taken from corresponding fractions in **a**.*

R.1.3.3. Affinity chromatography

Next, the purified samples were injected onto a HiTrap Heparin HP affinity chromatography column which selectively binds DNA binding proteins, such as MutS (**see M.2.8**). Before injection the salt concentration of the pooled fractions was adjusted to 100 mM KCl to enable successful binding to the column. After sample application the proteins were eluted using a gradually applied high salt buffer (1 M KCl).

During purification of MutS^{E694Q} the pooled fractions were not properly adjusted to 100 mM salt concentration, resulting in incomplete binding to the column as indicated by the presence of MutS^{E694Q} in the flowthrough (**Fig. 26, Flowthrough I**). After further decreasing the salt concentration and reinjecting the flowthrough MutS^{E694Q} did bind to the column although some of it was still present in the flowthrough (**Fig. 26, Flowthrough II**).

When administering the elution buffer a well-defined peak in A_{280} was observed in all chromatograms. Samples taken from corresponding fractions were distinctly enriched in MutS as shown by SDS-PAGE (**Fig. 26, B2-B7, Fig. 27, B3-B8 and Fig. 28, C4-D1**).

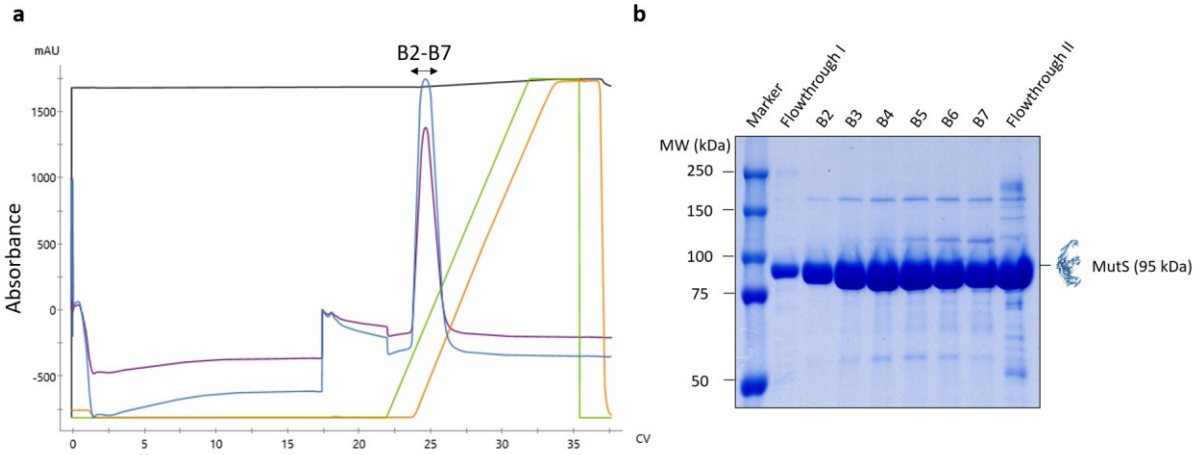

***Figure 26. Affinity chromatography purification data MutS^{E694Q}. a**, Chromatogram obtained during purification. Y-axis shows absorbance levels A_{260} (purple) and A_{280} (blue). Black, orange and green lines represent pH, conductivity and amount of injected high salt wash buffer, respectively. Elution volume is expressed in column volumes (CV). **b**, SDS-PAGE gel showing samples taken from corresponding fractions in **a**.*

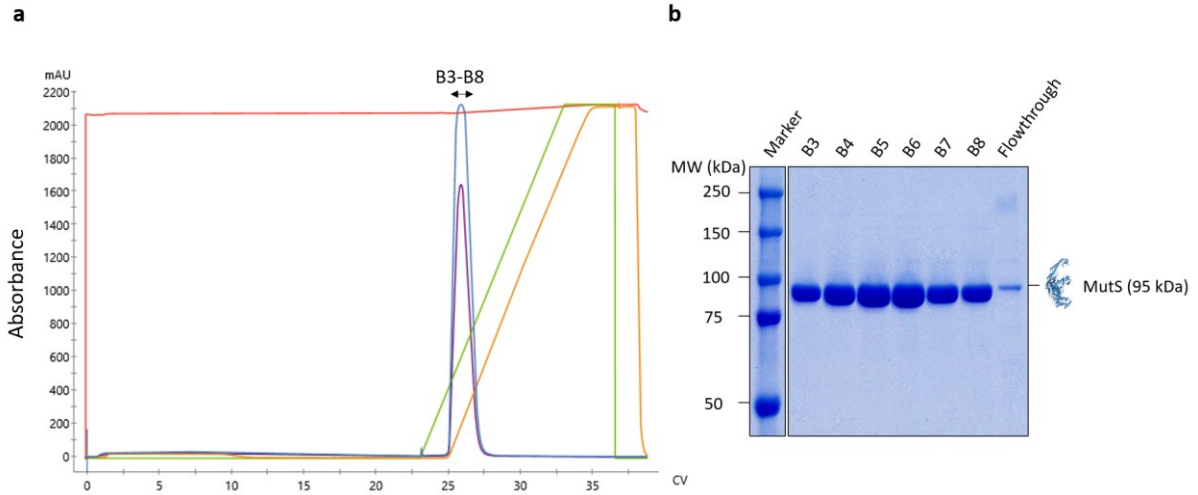

***Figure 27. Affinity chromatography purification data MutS^{E694D}. a**, Chromatogram obtained during purification. Y-axis shows absorbance levels A_{260} (purple) and A_{280} (blue). Red, orange and green lines represent pH, conductivity and amount of injected high salt wash buffer, respectively. Elution volume is expressed in column volumes (CV). **b**, SDS-PAGE gel showing samples taken from corresponding fractions in **a**.*

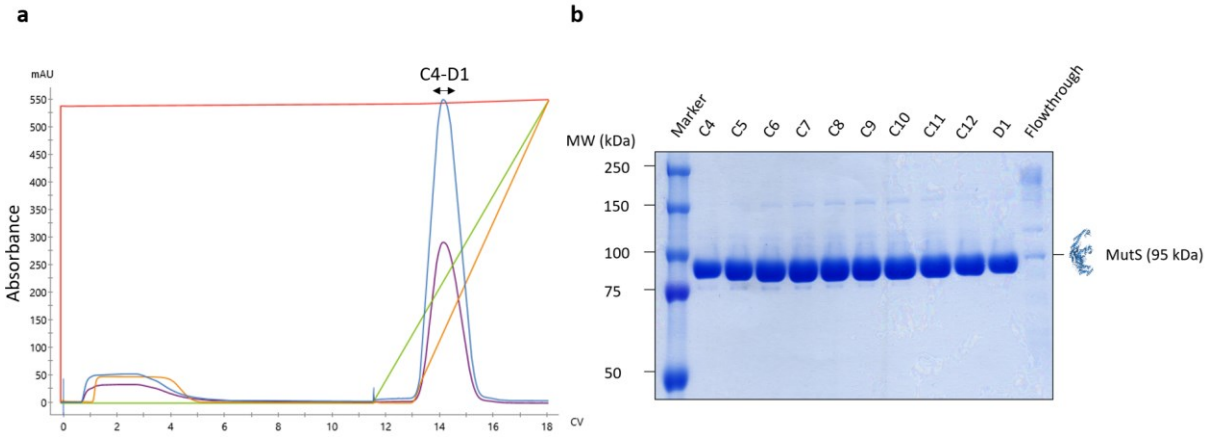

***Figure 28. Affinity chromatography purification data MutS^{Wt}. a**, Chromatogram obtained during purification. Y-axis shows absorbance levels A_{260} (purple) and A_{280} (blue). Red, orange and green lines represent pH, conductivity and amount of injected high salt wash buffer, respectively. Elution volume is expressed in column volumes (CV). **b**, SDS-PAGE gel showing samples taken from corresponding fractions in **a**.*

R.1.3.4. Size exclusion chromatography gel filtration column II

Finally, the pooled fractions obtained after purification by the HiTrap Heparin HP column were injected onto a SEC column (**see M.2.6 and M.2.9**). In most cases the chromatograms obtained after the final SEC column consisted of three peaks around 0.35, 0.45 and 0.55 CV (**Fig. 29, 30 and 31**).

The first peak, around 0.35 CV, contains residual aggregates which were not filtered during the first SEC run (**see R.1.3.1**), as indicated by the enriched presence of MutS in corresponding fractions (**Fig. 29, C1**). The peak around 0.55 CV contained traces of MutS (**Fig. 29, E6**). However, judging by the $\frac{A_{260}}{A_{280}}$ ratio of approximately 1, the eluate corresponding to this peak likely consisted of residual nucleic acids. The peak obtained around 0.45 CV was distinctly enriched in MutS as shown by SDS-PAGE (**Fig. 29, C10-D3, Fig. 30, C10-D4 and Fig. 31, C9-D2**). Furthermore, no additional proteins were observed to be present and the $\frac{A_{260}}{A_{280}}$ ratio of this peak was around 0.5-0.6, which is generally accepted as pure for protein solutions.

Subsequently, the pure fractions were pooled, concentrated and filtered using a Vivaspin® column with a molecular weight cut-off of 10 kDa (**see M.2.9**). The final concentrations were calculated using a molar extinction coefficient of ε = 73,230 $M^{-1}cm^{-1}$ after spectrophotometric determination of the absorbance at 280 nm. The proteins were subsequently aliquoted, flash-frozen in liquid nitrogen and stored at -80 °C. The total yields, each obtained from 6 L bacterial cultures, were 16 mg, 19 mg and 6 mg from the purifications of $MutS^{E694Q}$, $MutS^{E694D}$ and $MutS^{Wt}$, respectively. Taken together the data indicate that all three MutS variants were successfully purified.

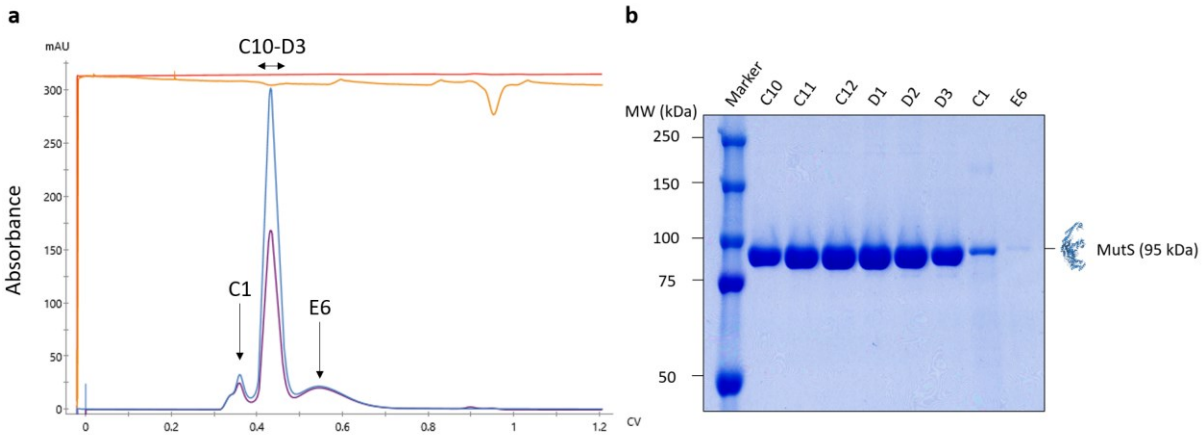

***Figure 29. SEC column II purification data $MutS^{E694Q}$. a**, Chromatogram obtained during purification. Y-axis shows absorbance levels A_{260} (purple) and A_{280} (blue). Red and orange lines represent pH and conductivity, respectively. Elution volume is expressed in column volumes (CV). **b**, SDS-PAGE gel showing samples taken from corresponding fractions in **a**.*

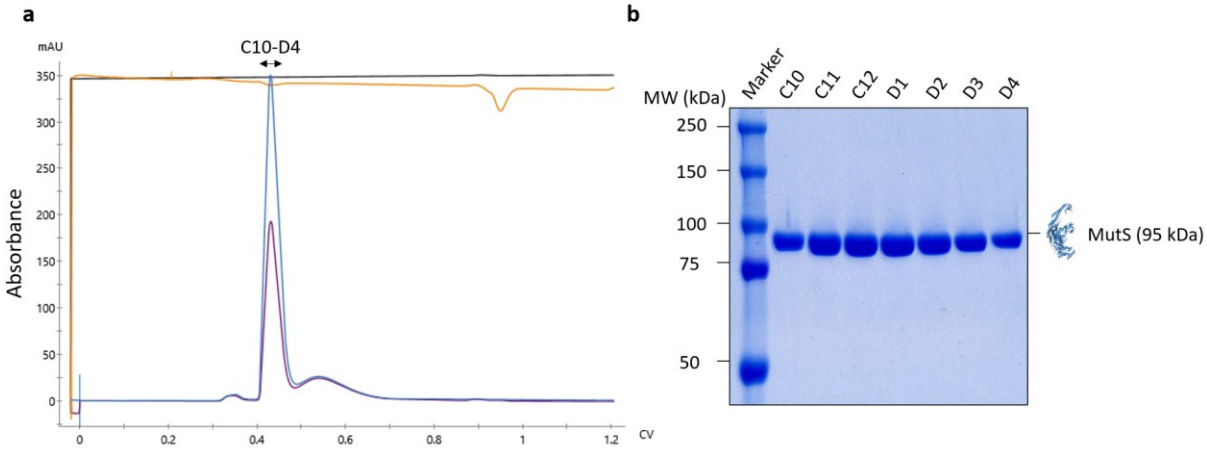

***Figure 30. SEC column II purification data MutS^{E694D}. a**, Chromatogram obtained during purification. Y-axis shows absorbance levels A_{260} (purple) and A_{280} (blue). Black and orange lines represent pH and conductivity, respectively. Elution volume is expressed in column volumes (CV). **b**, SDS-PAGE gel showing samples taken from corresponding fractions in **a**.*

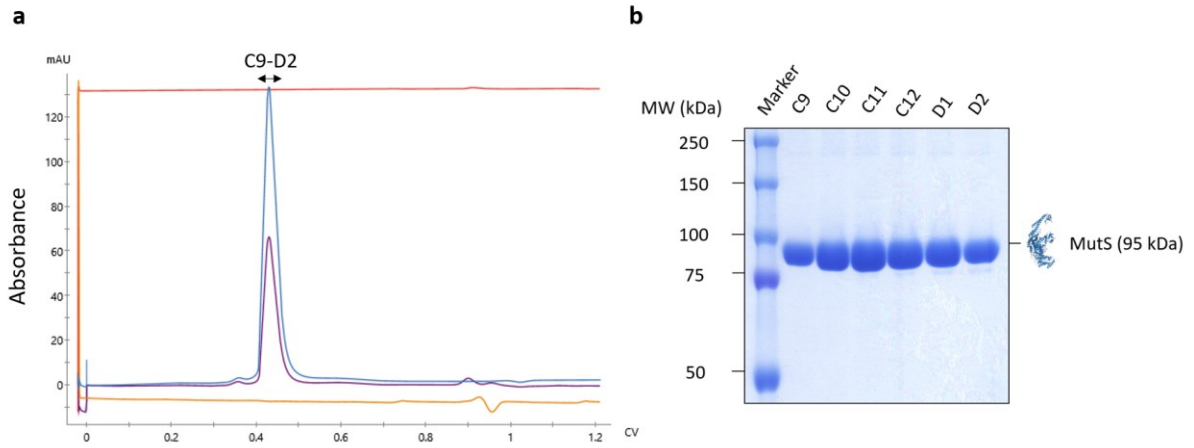

***Figure 31. SEC column II purification data MutS^{Wt}. a**, Chromatogram obtained during purification. Y-axis shows absorbance levels A_{260} (purple) and A_{280} (blue). Red and orange lines represent pH and conductivity, respectively. Elution volume is expressed in column volumes (CV). **b**, SDS-PAGE gel showing samples taken from corresponding fractions in **a**.*

4

Results

Nucleotide binding and hydrolysis

R.2 Implementation of a custom colorimetric ATPase assay and biochemical characterization of the ATPase activity of wildtype and mutant MutS

R.2.1 The principle behind the assay

In order to biochemically characterize the ATPase activity of wildtype and mutant MutS a colorimetric ATPase assay was implemented and optimized. The assay is based on a chemical reaction between the orthophosphate (phosphate) liberated during ATP hydrolysis, molybdate and a triphenylmethane dye in acidic solution, resulting in a colorimetric product the amount of which is proportional to the concentration of phosphate[81,82]. By measuring the absorbance of the dye-phosphomolybdate complex at its absorption maximum (620 nm) and comparing the measurements to a suitable standard, the amount of phosphate can be deduced.

The reaction occurs in two stages. First, the phosphate produced during ATP hydrolysis reacts with molybdate to form phosphomolybdate, which in turn can form a complex with the triphenylmethane dye, resulting in a marked shift in absorption maximum from that of the dye[83]. In this study the triphenylmethane dye of choice is malachite green which has been shown to result in the most sensitive detection of phosphate compared to other triphenylmethane dyes[81,84,85].

By calculating the amount of phosphate produced over time by wildtype or mutant MutS for a range of different ATP concentrations and fitting the data according to Michaelis-Menten kinetics, it is possible to determine the maximum steady-state velocity at which the protein hydrolyses ATP and to determine its affinity for this substrate. In this manner we aim to biochemically characterize the functional effects of the different mutations introduced in the active site of the MutS ATPase domain.

R.2.2 Characterization of a commercially available malachite green assay

R.2.2.1 Characterizing the kit reagents

Initially, a commercially available colorimetric ATPase assay (Sigma-Aldrich, Cat. No. MAK113-1KT) based on the malachite green molybdate chemistry, described in the previous section, was tested to determine the feasibility of investigating MutS ATPase activity in this manner. The kit supplies a 1 mM phosphate standard, an assay buffer (40 mM Tris, 80 mM NaCl, 8 mM $MgAc_2$, 1 mM EDTA, pH 7.5) and assay reagent, containing unknown amounts of malachite green and molybdate, and should cover approximately 200 reactions. For each experiment an appropriate phosphate standard curve has to be generated by diluting the 1 mM phosphate standard in Milli-Q. The amount of phosphate present in samples of interest can then be calculated based on the functional relation between the spectrophotometrically determined absorptivity and phosphate concentration in the standard curve series. Reactions are quenched by supplementing 200 µl of the highly acidic (pH ≈ 2) assay reagent after which the reactions are incubated for 35 min to allow the color to develop.

Since the supplied assay buffer was not compatible with our own assay buffer, we first tested whether our assay buffer was not contaminated with phosphate and was compatible with the kit reagents. The optical density measurements did not differ significantly from the assay buffer supplied by the kit (data not shown), indicating our buffer was not contaminated and was compatible with the kit reagents and could therefore be used during subsequent experiments.

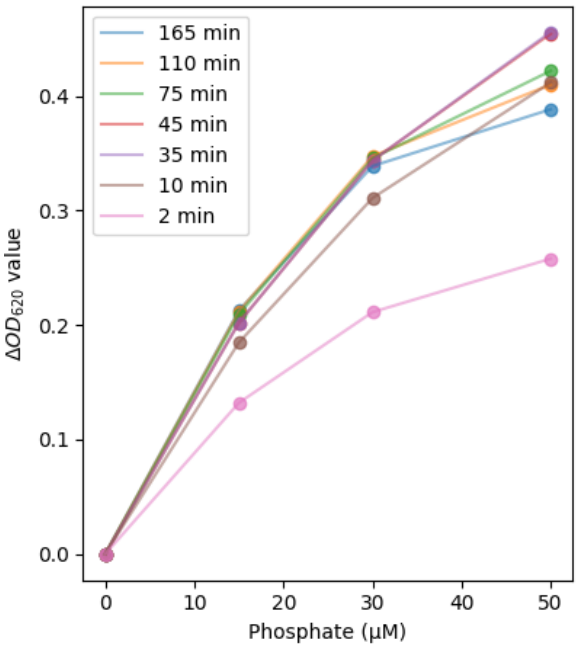

***Figure 32**. Exemplary data showing the development of the kit phosphate standard over time at different phosphate concentrations.*

Next, the standard curve from the kit was characterized by following its development over time. A standard curve ranging from 0 to 50 µM phosphate was generated. Subsequently, the absorptivity at 620 nm was measured over time (**Fig. 32**). The kit recommends measuring 30 min after quenching the reactions with the assay reagent, although it also states the optimal time may have to be determined experimentally. Indeed after 35 min the standard curve stabilizes for at least 10 min. However, after 75 min the measurement at the highest concentration (50 µM) was significantly lower compared to the measurement at 35 min. After 110 and 165 min this trend continued and the OD_{620} was reduced even further, suggesting crystallization and sedimentation of the malachite green phosphomolybdate complex, which is known to occur in the absence of a detergent at phosphate concentrations higher than 10 µM[86]. The standard curve also starts to deviate significantly from linearity at higher concentrations, suggesting the kit reagents can only be used to determine low amounts of phosphate accurately.

R.2.2.2 Initial validation of the commercial ATPase assay

To test the suitability of the colorimetric ATPase assay a first experiment was conducted using the kit. In this experiment 40 µl reactions with a final concentration of either 0.75 or 7.5 µM $MutS^{Wt}$ were incubated with 1 mM ATP for 6, 12, 30 and 60 min. Subsequently, the reactions were quenched with 200 µl of the assay reagent. Following a 35 min incubation, the absorptivity at 620 nm was measured. Furthermore, a standard curve ranging from 0 to 50 µM phosphate was fitted to a linear function and the phosphate concentrations from the two time series were calculated accordingly.

The data obtained from the samples where the final concentration of MutS was 0.75 µM followed a linear relation, as expected (**Fig. 33, blue dataset**). From literature it is known that at 1 mM ATP wildtype MutS reaches maximal steady-state turnover (V_{max}). After normalising the fitted velocity to the amount of protein, the apparent V_{max} was calculated to be 1.5 min^{-1} which agrees well with published values for the V_{max} of wildtype MutS[12,20,21,44,59,87,88].

In contrast, the measurements taken from the samples where the final concentration of MutS was 7.5 µM did not follow a linear relation but quickly plateaued, likely due to depletion of one of the assay components. The amount of phosphate produced in 60 min with a V_{max} of 1.5 min^{-1} is much less than the 1 mM ATP present in the reaction, therefore it seems that at high phosphate concentrations the malachite green or molybdate in the assay reagent is being depleted which would also explain why the standard curve does not follow a linear relation at high phosphate concentrations.

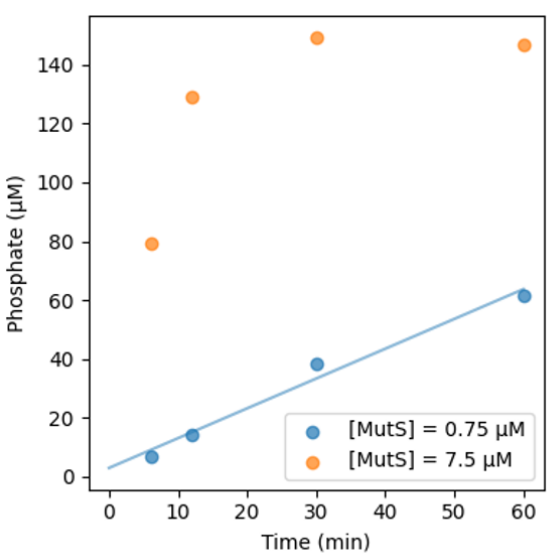

Furthermore, samples to which buffer instead of ATP was supplemented showed no significant increase in absorptivity over time. However, substituting the protein with buffer (i.e. no enzyme control) did result in a marked increase in absorptivity over time, indicating that ATP was spontaneously hydrolysed likely due to the low pH of the quenching reagents. To correct for this the values of the no enzyme control were subtracted from the sample values before comparison to the standard curve. Taken together, the data shows it is possible to determine steady-state turnover kinetics by MutS using the kit, although only for low amounts of phosphate and complicated by spontaneous ATP hydrolysis.

Figure 33. Initial ATPase experiment using the Merck kit*. Phosphate produced over time for final concentrations of 0.75 (**blue**) and 7.5 (**orange**) µM MutS^{Wt}. Linear fit is shown as solid blue line.*

R.2.3 Optimization and validation of a custom ATPase assay

R.2.3.1 Comparative analysis with the commercially available kit

Since the commercially available kit has some limitations and is relatively expensive, limiting analysis to small datasets, a custom colorimetric ATPase assay based on the malachite green molybdate chemistry described earlier was implemented (**see R.2.1**).

To increase the linear and dynamic range of the standard curve we tried to prevent agglutination and sedimentation of the dye-phosphomolybdate complexes by supplementing either Polyoxyethylene (20) sorbitan monolaurate or octylphenoxypolyethoxyethanol (commonly referred to as Tween-20 and Nonidet P-40 substitute, respectively) which are two non-ionic detergents[81,82].

The assay reagents are generated as described in **M.3.1**. To compare the efficacy of the custom-made reagents with those provided by the kit, spectral absorbance was recorded in 10 nm intervals across the 400-700 nm range for varying concentrations of phosphate (0, 15, 30, and 50 µM) (**Fig. 34c**). Moreover, the absorptivity of the reagents was determined at 620 nm using either the in-house 1 mM phosphate standard or the standard provided with the commercial kit (**Fig. 35**).

All absorbance spectra exhibited two distinct peaks at 440 nm and 620 nm, with the peak at 620 nm being most sensitive to changes in phosphate concentration, as expected (**Fig. 34c**). To determine the most sensitive combination of reagents, standard curves were generated using either the custom-

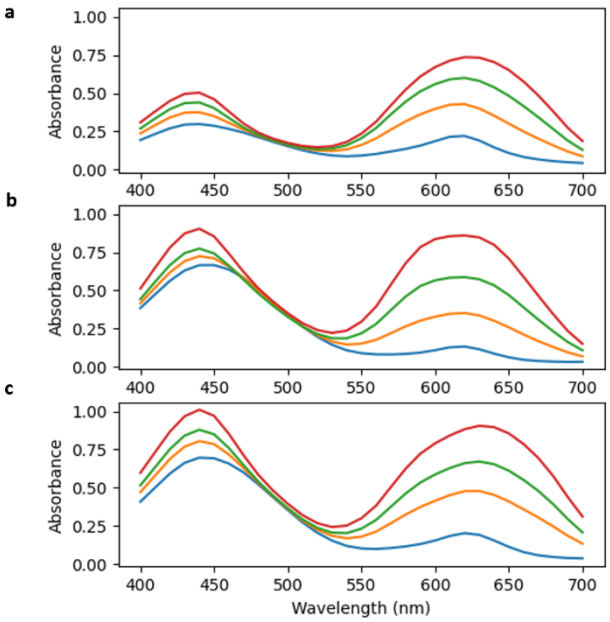

***Figure 34**. Absorption spectra for phosphate concentrations of 0 (blue), 15 (orange), 30 (green) and 50 (red) µM for reactions quenched using the kit (**a**) or custom made reagents including either NP-40 substitute (**b**) or Tween-20 (**c**).*

made 1 mM phosphate standard or the Merck kit phosphate standard. Subsequently, the blank corrected, ΔOD620, values were compared for the three different reagents (**Fig. 35a and b**). Both homemade reagents seem to outperform the kit reagent by being more sensitive to changes in phosphate concentration at 440 nm and 620 nm and by following a linear relation over a larger dynamic range, possibly due to the presence of the detergents or a higher concentration of one of the reagent components. Moreover, no significant differences were observable between the dataset generated using either the homemade or kit supplied 1 mM phosphate standard. Additionally, generating the reagents in house resulted in an approximately 1000-fold cost reduction for a standard 200 µl reaction from €2.22 to €0.0017, making it significantly more feasible to conduct large scale experiments. Collectively, these findings suggest that the homemade reagents are a more cost-effective and sensitive alternative to the commercial kit reagents and can be used reliably to determine phosphate levels over a wide range of concentrations.

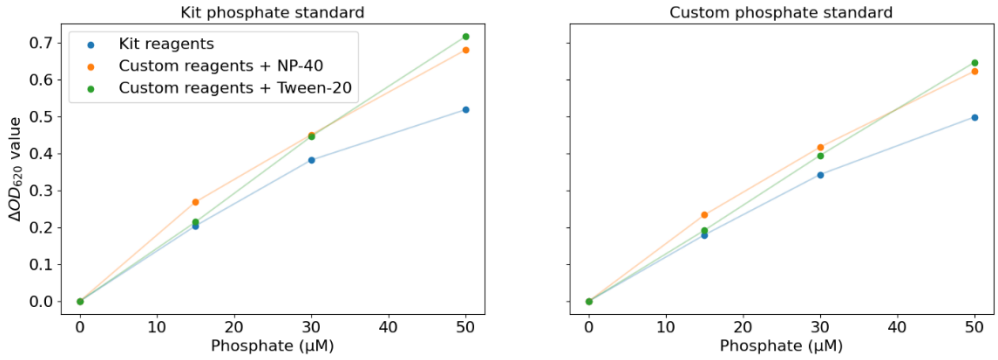

***Figure 35**. Blank corrected absorption values at 620 nm (ΔOD_{620}) for a range of phosphate concentrations prepared using the commercial (**left**) or custom-made (**right**) phosphate standard for reactions quenched using the kit (blue) or custom made reagents including either NP-40 substitute (orange) or Tween-20 (green). Data is shown as points and linear interpolations are shown as solid lines.*

R.2.3.2 Sodium citrate prevents spontaneous ATP hydrolysis

In order to further optimize the assay spontaneous hydrolysis of ATP due to the high acidity of the quenching reagents was addressed. Therefore, effects of supplementing Trisodium 2-hydroxypropane-1,2,3-tricarboxylate (sodium citrate) following quenching were investigated. When

dissolved sodium citrate increases the alkalinity of the solution and is therefore expected to prevent spontaneous ATP hydrolysis by neutralizing the reactions.

A dilution series of solutions containing either 0.125 mM, 0.25 mM, 0.5 mM or 1 mM ATP in assay buffer was generated and 40 µl of these solutions were quenched using 200 µl of the homemade quenching reagent. Subsequently, the absorptivity was measured for 50 min every 5 min starting from 15 min. As expected, a concentration dependent increase in A_{620} was observed over time (**Fig. 36**).

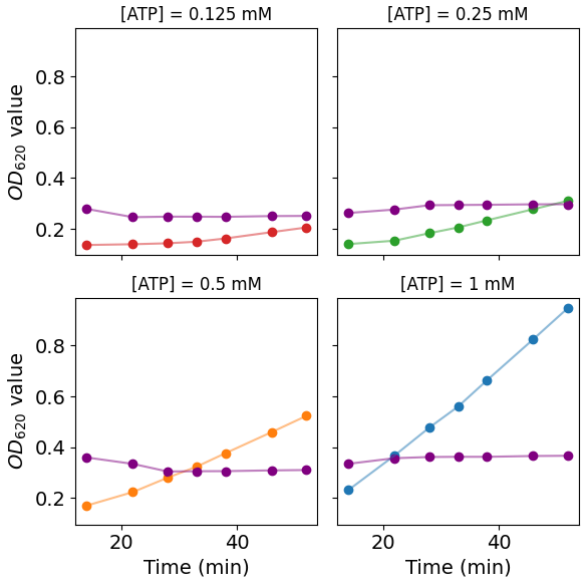

***Figure 36. Sodium citrate prevents spontaneous ATP hydrolysis**. Reactions containing 0.125 (**red**), 0.25 (**green**), 0.5 (**orange**) or 1 mM ATP (**blue**) were quenched and the optical density 600 was followed over time. Simultaneously, identical reactions to which sodium citrate was supplemented 2 min following quenching were followed (**purple**).*

When supplementing the reactions with 24 µl sodium citrate (~10% of the final volume), 2 min after quenching, the absorptivity did not increase significantly over time (**Fig. 36, purple traces**), indicating that sodium citrate prevents spontaneous hydrolysis of ATP. However, the background signal was also enhanced, thereby reducing the sensitivity of the assay. Collectively, the data indicate that sodium citrate prevents spontaneous hydrolysis of ATP when supplemented 2 min after quenching at the cost of a slight reduction in sensitivity. Given the significant improvement this trade off was deemed acceptable and sodium citrate was supplemented during subsequent experiments as well.

R.2.4 Determination of ATPase activity of MutS^{Wt}, MutS^{E694Q}, MutS^{E694D} and MutS^{E694N}

In order to biochemically characterize the effects of the amino acids substitutions, the ATPase activity of wildtype and mutant MutS purified from *mutS* deficient *E. coli* BL21(DE3)pLysS,mutS:Tn10 (**see M.2**) were investigated using the custom ATPase assay. To this end, enzymatic activity was monitored over time at various concentrations of ATP and analysed according to Michaelis-Menten kinetics (**see M.3.3**). Fitting the data in this manner results in values for the maximum steady-state ATP hydrolysis velocity (V_{max}) and binding affinity for ATP (K_m).

R.2.4.1 Determination of the kinetic parameters of the MutS^{Wt} ATPase activity

According to literature wildtype MutS is expected to have a V_{max} around 1-2 min^{-1} and a K_m for ATP in the range of 10-100 µM[20,21,44,57,59,87,88]. The lowest non-zero concentration of ATP for which to study ATPase activity was chosen to be 10 µM such that a K_m of 10 µM would still be measurable. Furthermore, in order to obtain signal above the lower detection limit of 5 µM and prevent substrate depletion, a time series of 10, 12 and 14 min was chosen in combination with a range of ATP concentrations from 0-1 mM (**Fig. 37**).

Reactions were initiated by supplementing 10 µl ATP to 30 µl enzyme in assay buffer A (**see M.3.2**) such that the final concentration of enzyme became 1 µM and that of ATP as specified (**Fig. 37**). This approach allowed for the investigation of multiple turnover kinetics for all ATP concentrations. Subsequently, the reactions were quenched 10, 12 or 14 min after supplementing ATP and neutralized with sodium citrate exactly 2 min thereafter. Following the addition of sodium citrate, the reactions were incubated for exactly 35 min before measuring the absorption at 620 nm. Measured absorption values were compared to a phosphate standard curve which spanned a concentration range of 0-100 µM phosphate. The phosphate levels in each reaction were determined based on this comparison (**see M.3.2**).

Control reactions in which either the enzyme or ATP was substituted with an equal volume of buffer were simultaneously assessed for activity. As expected, no increase in A_{620} was observed in either the controls lacking enzyme (data not shown) or ATP (**Fig. 37, see [ATP]=0**), indicating that all observed increases in A_{620} were due to enzymatic activity. Additionally, these results confirm that sodium citrate effectively prevented spontaneous ATP hydrolysis.

The velocity profile for each ATP concentration was calculated by linearly fitting the changes in phosphate concentration over time (**Fig. 37a**). These fitted velocities were plotted against the ATP concentrations and fitted to the Michaelis-Menten kinetics model (**Fig. 37b**).

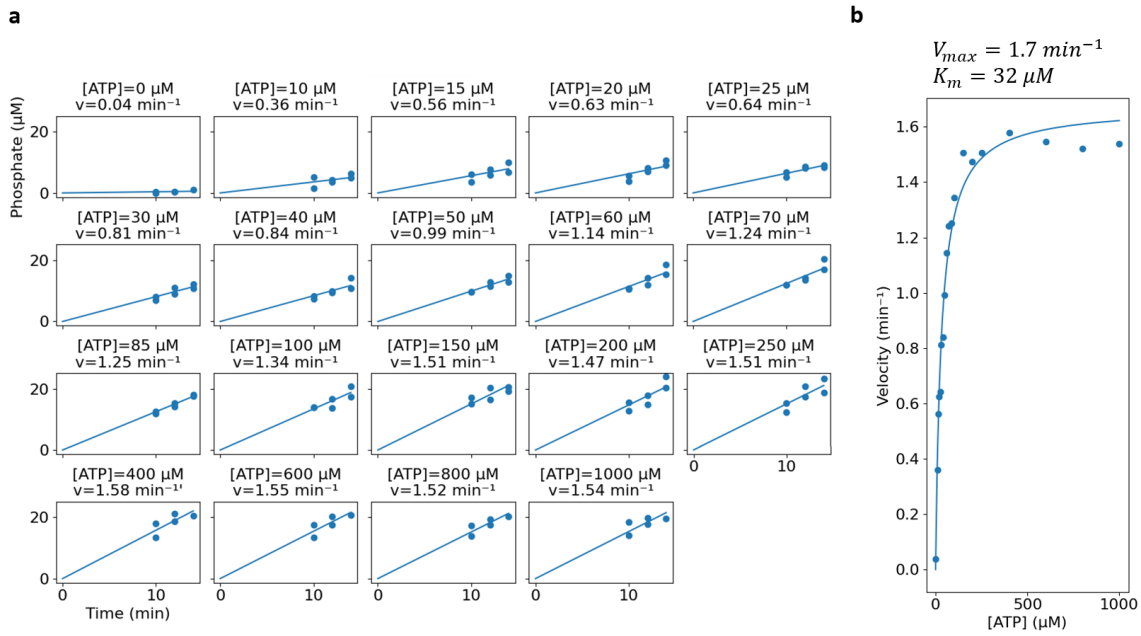

Figure 37. Exemplary dataset for the enzyme kinetics of MutS^{Wt}. ***a,*** *Velocity profiles for various concentrations of ATP ranging from 0 to 1000 µM. Subplots display absolute amount of phosphate produced over time.* ***b****, Michaelis-Menten fit to the fitted velocities shown in* ***a****. Fits are shown as solid blue lines.*

The data was fitted well by the Michaelis-Menten model (R^2 = 0.98) and values for V_{max} and K_m were calculated to be 1.8 ± 0.42 min^{-1} (Mean $\pm$ STD, N=4) and 43 ± 8.3 µM (Mean $\pm$ STD, N=3), respectively. The fitted values for the V_{max} and K_m agree well with values reported in literature[20,21,42,57,59,87], indicating it is feasible to use the custom ATPase assay to derive kinetic parameters of MutS in this manner. However, it should be noted that the determination of the V_{max} is based on differences in phosphate concentrations, whereas the K_m is determined based on absolute phosphate concentrations, therefore the value for the V_{max} is more accurate.

R.2.4.2 Determination of the kinetic parameters of the MutS^{E694Q} ATPase activity

Next, the ATPase activity of MutS^{E694Q} was investigated. Unfortunately, there is feeble literature on enzymatic activity of MutS^{E694Q}, however Junop et al. (2001) measured its V_{max} and K_m to be 0.19 min^{-1} and 15.6 µM, respectively[21]. Experiments were conducted as described before (**see R.2.4.1**) but with the alteration that enzymatic activity was assessed after 30, 45, 60 and 90 min incubations. Furthermore, a final concentration of 5 µM enzyme was chosen in order to make the experiments feasible timewise. Data was analysed as described before (**see R.2.4.1**) with the addition that fitted velocities were normalized to 1 µM protein.

As expected, the fitted velocities increased monotonically with increasing concentration of ATP (**Fig. 38**). Additionally, no increase in absorptivity was observed in either the controls lacking enzyme or ATP, indicating that all observed increases in absorptivity were due to enzymatic activity. The data was fitted well by the Michaelis-Menten model (R^2 = 0.99) and the V_{max} as well as the K_m were calculated to be 0.19 $\pm$ 0.017 min^{-1} and 33 $\pm$ 8.3 µM, respectively (Mean $\pm$ STD, N=3), in accordance with the value as determined by Junop et al. (2001). However the value for the K_m is slightly higher, although still in the same order of magnitude. The value of the K_m for ATP as determined by Junop et al. (2001) is significantly lower than the lowest concentration of ATP for which the hydrolysis velocity was determined in their assay and should therefore be considered less accurate[21].

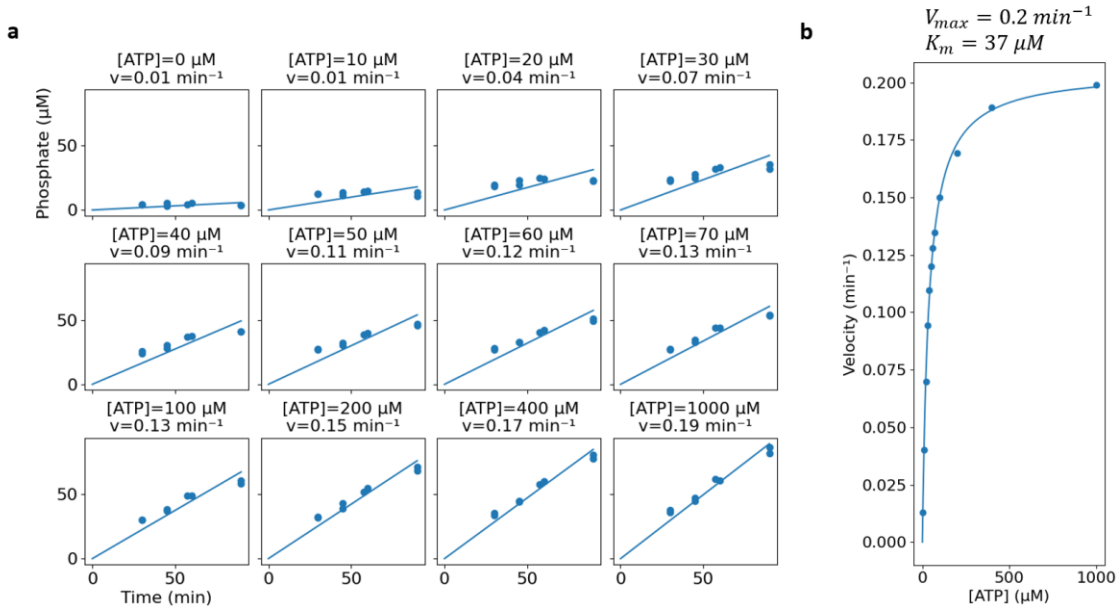

Figure 38. Exemplary dataset for the enzyme kinetics of MutS^{E694Q}. ***a,*** *Velocity profiles for various concentrations of ATP ranging from 0 to 1000 µM. Subplots display absolute amount of phosphate produced over time. Velocities shown on top are normalized to 1 µM enzyme.* ***b****, Michaelis-Menten fit to the fitted velocities shown in* ***a****. Fits are shown as solid blue lines.*

R.2.4.3 Determination of the kinetic parameters of the MutS^{E694D} ATPase activity

Subsequently, the ATPase activity of MutS^{E694D} was investigated. MutS^{E694D} is reduced in functionality to such an extent that minute changes in phosphate levels had to be detected in order to determine the K_m for ATP. Therefore, the measurement variation relative to the signal became so large multiple datasets obtained over different days were combined in order to obtain an estimate of the K_m for

ATP. A final concentration of 1 µM enzyme was used in reactions containing less than 40 µM ATP and reactions were incubated for 100, 120, 140, 160, 180 and 200 min after addition of ATP. Furthermore, the incubation time after addition of sodium citrate was increased from 35 min to 16 h in order for all the dye-phosphomolybdate complexes to form.

Lengthening the duration of complex formation worked well for low phosphate concentrations, as judged by the absence of elevated signal in controls lacking enzyme and enhanced signal in reactions containing enzyme. However, at high concentrations significant signal was detected in the controls lacking enzyme, indicating that over long periods of time ATP is hydrolysed spontaneously.

Therefore, the absorptivity of reactions with a final concentration of ATP above 40 µM were measured 35 min after addition of sodium citrate, whereas the absorptivity of reactions containing lower concentrations was measured ~16 h later. Furthermore, reactions containing concentrations above 40 µM ATP were incubated for 30, 60, 90 and 120 min after addition of ATP and were conducted with a final concentration of 5 µM enzyme.

In general, the fitted velocities increased with increasing concentration of ATP (**Fig. 39a**). By fitting the combined datasets (**Fig. 39b**) the V_{max} was calculated to be 0.054 $\pm$ 0.0085 min^{-1} (Mean $\pm$ STD, N=4) and the K_m for ATP was calculated to be 4.1 µM. Due to the relatively high measurement variation the fit was inaccurate (R^2 = 0.78), therefore the obtained K_m value should be considered as an estimate.

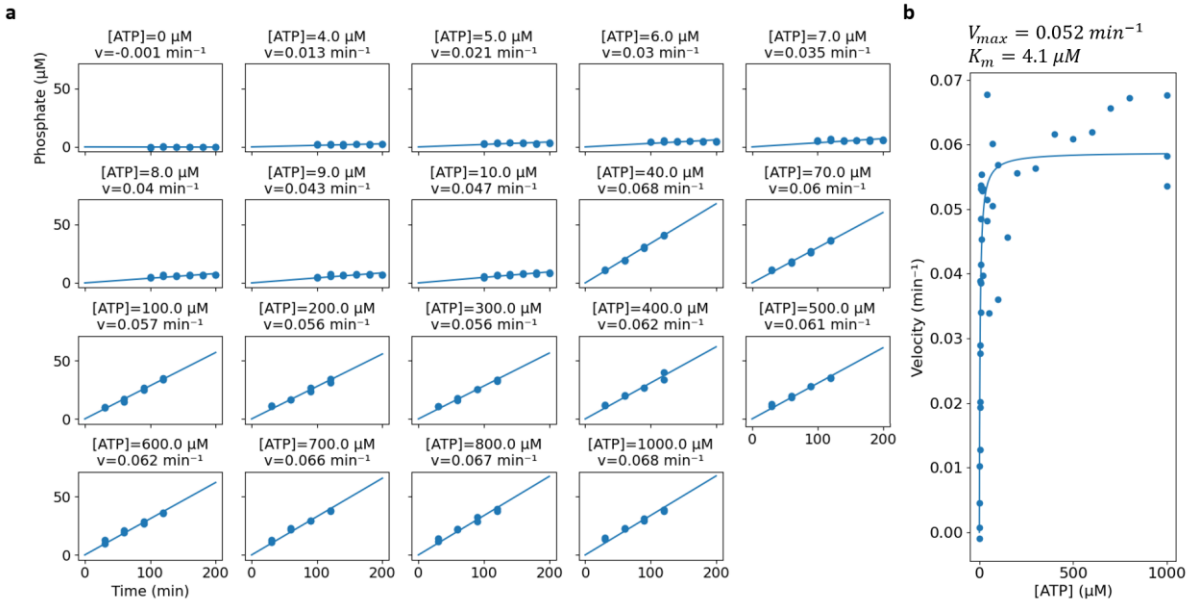

Figure 39. Exemplary dataset for the enzyme kinetics of MutS^{E694D}. a, *Exemplary velocity profiles for various concentrations of ATP ranging from 0 to 1000 µM. Subplots display absolute amount of phosphate produced over time. Velocities shown on top are normalized to 1 µM enzyme.* ***b****, Michaelis-Menten fit to the fitted velocities of all datasets. Fits are shown as solid blue lines.*

R.2.4.4 Determination of the kinetic parameters of the MutS^{E694N} ATPase activity and overall summary

Finally, the enzymatic activity of MutS^{E694N} was assessed. Based on the absence of a negatively charged carboxyl group in addition to a shortened sidechain compared to wildtype MutS this mutant was expected to be impaired in ATPase activity even more than MutS^{E694D}. Furthermore, initial tests

showed that the maximal steady state velocity was in the order of 0.01 min^{-1}, therefore a final concentration of 10 µM was used in order to make the experiment feasible timewise. This meant it was not possible to investigate multiple turnover kinetics for concentrations lower than 20 µM ATP. Therefore, only an upper bound was determined for the K_m.

Reactions were incubated with 0, 20, 40, 70, 150 or 1000 µM ATP for 2, 3 and 4 h and data was analysed as described before (**see R.2.4.1**) with the addition that calculated velocities were normalized to 1 µM protein.

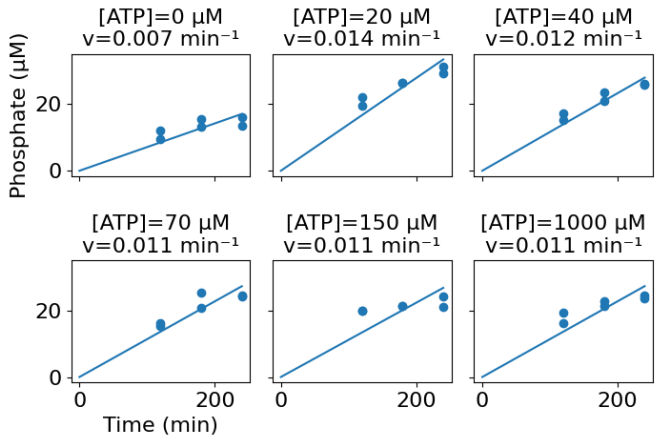

***Figure 40**. Velocity profiles for a range of different ATP concentrations for MutS^{E694N}. Subplots display absolute amount of phosphate produced over time. Velocities shown on top are normalized to 1 µM enzyme.*

The velocity profiles showed (**Fig. 40**) no significant increase from 20 to 1000 µM ATP, indicating that already at 20 µM the enzyme reached maximum steady-state turnover kinetics. Consequently, the K_m for ATP must be less than 20 µM. Furthermore, the V_{max} was calculated to be 0.012 ± 0.0012 min^{-1} (Mean ± STD, N=4). Unexpectedly, even in the absence of externally supplemented ATP, phosphate production was observed which did not occur in the control reactions lacking enzyme. Furthermore, it is known that the MutS is sporadically purified with nucleotides bound to the active site[38]. Therefore, the data suggest that prebound ATP is hydrolysed, resulting in production of phosphate even in the absence of externally supplemented ATP. This may reflect enhanced binding affinity and reduced ATPase activity of MutS^{E694N} compared to the wildtype. Finally, the kinetic parameters for both wildtype and mutant MutS are consolidated in **Figure 41.**

MutS	V_{max} (min^{-1})	K_m (μM)
Wild type	1.8 ± 0.42	43 ± 8.3
E694Q	0.19 ± 0.017	33 ± 8.3
E694D	0.052 ± 0.0074	4.1
E694N	0.012 ± 0.0012	< 20

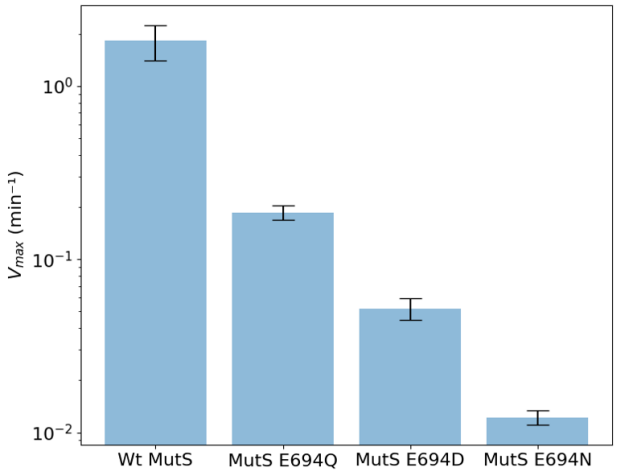

***Figure 41. Left,** Table summarising the kinetic parameters representing ATPase activity of wildtype and mutant MutS. **Right**, Bar plot showing the maximum steady-state hydrolysis velocity for wildtype and mutant MutS. Data is shown as mean ± std, N≥3.*

R.3 Nucleotide exchange

R.3.1 The principle behind the assay

To study nucleotide binding by wildtype and mutant MutS, nucleotide exchange (ADP release followed by ATP binding) was monitored in the absence and presence of DNA. Nucleotide exchange induces a conformational transition in mismatch bound MutS, resulting in the release of the mismatch and conversion into a sliding clamp, enabling MutL and subsequently MutH recruitment, leading to pathway activation. Moreover, ADP release is an integral step during the steady-state hydrolysis cycle which is thought to be rate limiting for $MutS^{Wt}$ in the absence of DNA[44,56,59]. Understanding how the E694 residue is implicated in this process is therefore of great interest.

One method to study nucleotide exchange is by using an analogue of ADP chemically linked to a chromophore, Mant-ADP, which upon binding by MutS results in enhanced fluorescence due to spatial confinement of the chromophore. Injection of ATP triggers nucleotide exchange in Mant-ADP-bound MutS, resulting in a decrease in fluorescence over time. By monitoring and comparing the rate of fluorescence decrease for the MutS mutants in the absence and presence of DNA, the effect of the introduced amino acid substitutions on nucleotide exchange was investigated.

R.3.2 The negatively charged carboxyl group of E694 enhances ADP release

In order to investigate Mant-ADP release kinetics by the MutS mutants, 2.5 µM wildtype or mutant MutS was incubated with 1 µM Mant-ADP for 5 min (**see M.5**). Furthermore, to investigate the effects of DNA on nucleotide exchange, a molar excess of 5 µM either heteroduplex or homoduplex 41-bp DNA oligonucleotides was added as well. Subsequently, Mant-ADP release was initiated by injecting 1 mM ATP and release was monitored in real-time by exciting the reactions at 355 nm and measuring emission at 405 nm at 1 Hz for 5 min.

DNA of any kind (**Fig. 42, AT and GT**) enhanced nucleotide exchange in $MutS^{Wt}$. Notably, heteroduplex DNA promoted faster nucleotide exchange than homoduplex DNA (**Fig. 42 compare GT and AT**). These findings are consistent with previous research, indicating that DNA promotes nucleotide exchange and that the effect is more significant for heteroduplex than homoduplex DNA[44,56,59]. Furthermore, no decrease in signal was observed when substituting Mant-ADP, MutS (wildtype or mutant), or ATP with an equal volume of buffer (data not shown), indicating that injection of ATP initiated Mant-ADP release from MutS, as expected.

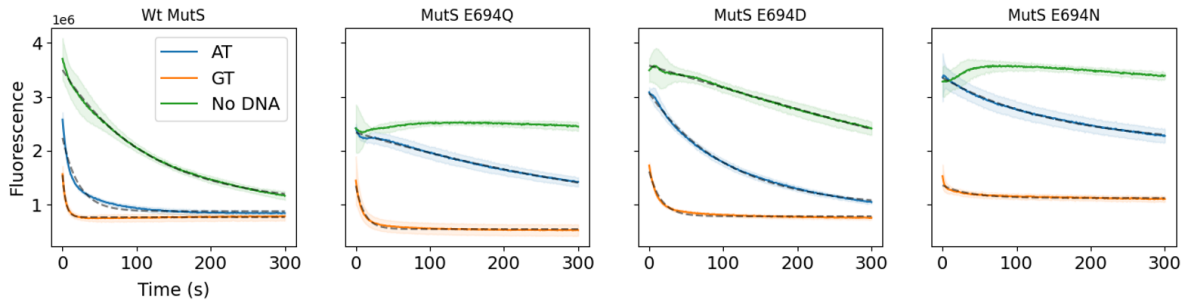

Figure 42. Nucleotide exchange for wildtype and mutant MutS*. Traces show Mant-ADP release after injection of 1 mM ATP either in the absence (green) or presence of homoduplex (blue) or heteroduplex (orange) DNA. Exponential fits are shown as dashed black lines. Data is represented as mean (solid lines) ± std (shaded regions), N=3.*

Acharya et al. (2003) proposed that the dissimilarity in nucleotide exchange observed between homo- and heteroduplex DNA could be attributed to the free ends of the homoduplex DNA[59]. To investigate this, the experiment was replicated with biotinylated oligonucleotides end-blocked with 10 µM streptavidin tetramer. In contrast to findings published by Acharya et al. (2003), end-blocking the ends of the DNA did not alter the release rate for $MutS^{Wt}$ (**Fig. 43 compare AT and GT with AT end-blocked and GT end-blocked, respectively**).

Furthermore, similar trends were observed when investigating Mant-ADP release by the MutS mutants. However, the results revealed that the release rate of Mant-ADP from the MutS mutants was notably slower than release from the wildtype. $MutS^{E694D}$ showed the fastest release rate, while $MutS^{E694Q}$ and $MutS^{E694N}$ displayed only a marginal rate of exchange (**Fig. 42**). The fluorescence decay was fitted well by single exponentials (with R^2 values ≥ 0.98), except for $MutS^{E694Q}$ and $MutS^{E694N}$ in the absence of DNA. The fluorescence decrease in $MutS^{E694Q}$ and $MutS^{E694N}$ in the absence of DNA was so small that it was not possible to fit the data. Additionally, no marked differences were observed in ADP-release by the MutS mutants when substituting DNA with free ends for end-blocked DNA, in accordance with data obtained using $MutS^{Wt}$ (**Fig. 43**). The fluorescence decay rates over time for wildtype and mutant MutS are summarized in **Table 1**.

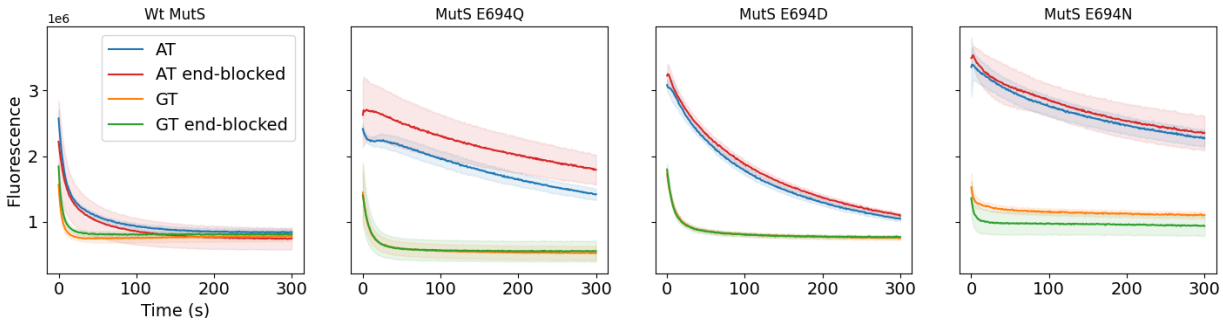

Figure 43. The effect of free DNA ends of nucleotide exchange for wildtype and mutant MutS*. Traces show Mant-ADP release after injection of 1 mM ATP in the presence of homoduplex (blue and red) or heteroduplex (orange and green) DNA in the absence (blue and orange) or presence (red and green) of end-blocks. Data is represented as mean (solid lines) ± std (shaded regions).*

	$ADP\ exchange, k_{off}^{ADP}\ (s^{-1})$		
MutS	**No DNA**	**Homoduplex DNA (AT)**	**Mismatched DNA (GT)**
Wild type	0.009 ± 0.001	0.046 ± 0.001	0.22 ± 0.02
E694Q	-	0.0022 ± 0.001	0.082 ± 0.02
E694D	0.001 ± 0.001	0.0093 ± 0.001	0.062 ± 0.006
E694N	-	0.0064 ± 0.0005	0.034 ± 0.02

Table 1. *Summary of the kinetic parameters of nucleotide exchange by wildtype and mutant MutS. Data is shown as mean ± std, N=3.*

5

Results

Affinity for DNA and nucleotide

R.4 Surface Plasmon Resonance

R.4.1 The principles of Surface Plasmon Resonance

DNA binding as well as the response of MutS to ATP binding were studied by surface plasmon resonance (SPR) in order to investigate whether the active site mutations in the MutS mutants influenced these properties of MutS. SPR enables real-time analysis of binding kinetics, based on changes in refractive index (**Fig. 44**). One of the main components of an SPR apparatus is the sensor surface which consists of a glass slide coated with a thin gold film covered by a dextran matrix. The dextran matrix acts as a substrate to which ligands can be conjugated. In this study, streptavidin tetramers were conjugated, enabling immobilization of biotinylated oligonucleotides onto the surface. Furthermore, an integrated microfluidic system enables the controlled flow of a solution containing analytes of interest over the sensor surface. As molecules bind to the sensor surface, the refractive index near the surface changes, leading to a shift in the angle of minimum reflective intensity. This shift in angle is proportional to the mass of material bound, enabling real-time monitoring of binding kinetics.

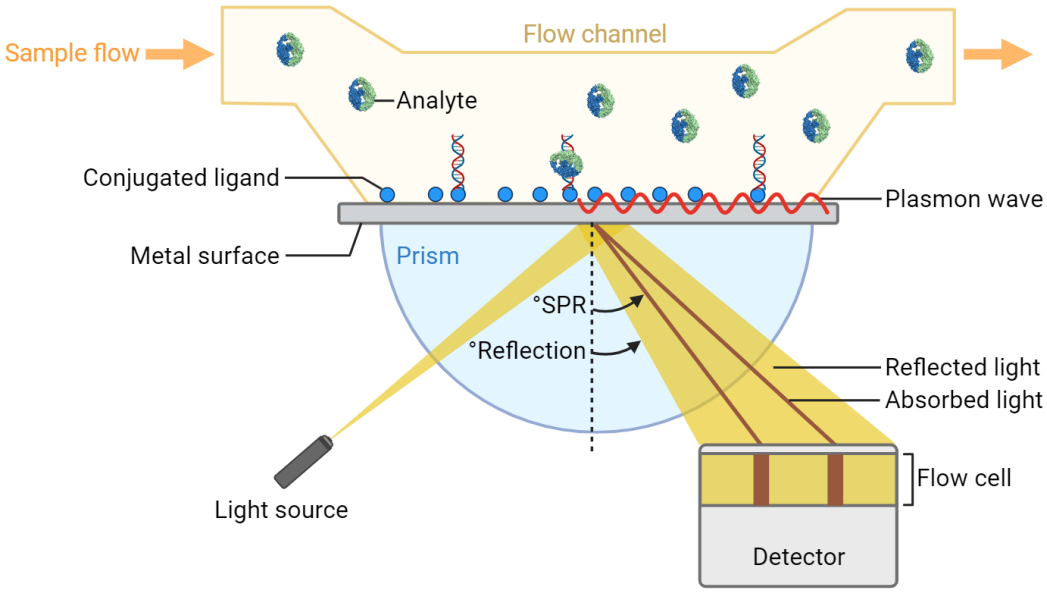

Figure 44. Schematic representation of the SPR detection principle*. The analyte of interest is flown over the sensor surface by an integrated microfluidics system. Binding to the surface alters the refractive index close to the surface, influencing the angle of minimum reflective intensity. The shift in this angle is proportional to the mass of the material bound, enabling real-time investigation of binding kinetics. Created with BioRender.com.*

In this manner, binding of wildtype and mutant MutS (analyte) to immobilized heteroduplex or homoduplex oligonucleotides (ligand) was assessed under various experimental conditions. In general any experiment can be divided into three distinct and consecutive phases: association, dissociation and regeneration. During the association phase (**Fig. 45, 2**) MutS binds to the surface immobilized DNA until either equilibrium between association and dissociation is reached or injection is halted (**Fig. 45, 3**). Subsequently, during buffer injection, MutS dissociates from the DNA leading to a decrease in signal (**Fig. 45, 4**). Finally, a regenerating solution is flown over the sensor surface to remove any remaining MutS, regenerating the surface and enabling a new cycle of binding and unbinding to be studied (**Fig. 45, 5**).

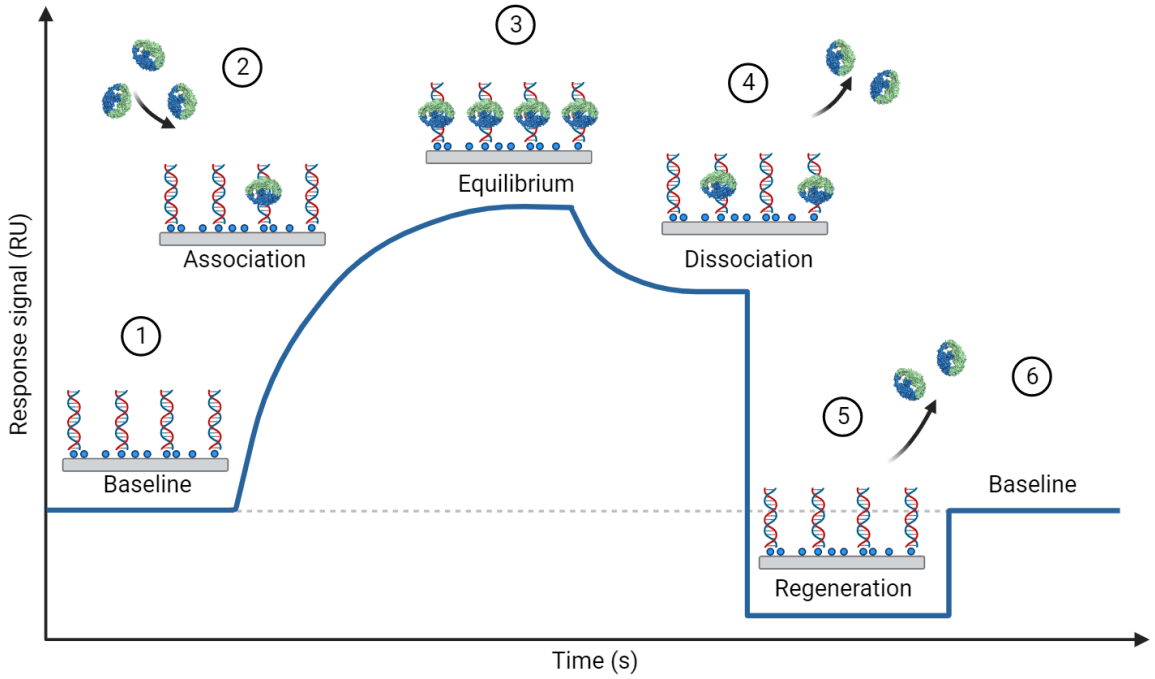

***Figure 45. Schematic overview of the distinct stages that occur in SPR**. During association (**2**) MutS binds to the surface immobilized DNA, leading to a significant rise in signal compared to the baseline (**1**), until reaching a state of equilibrium (**3**). Conversely, in the dissociation phase (**4**), MutS disengages from the DNA, causing a marked drop in signal. Finally, the sensor surface is regenerated in stage (**5**), which eliminates all remaining MutS that might still be attached to the DNA, returning the signal amplitude to the baseline. Created with BioRender.com.*

R.4.2 The MutS mutants are impaired in DNA binding

Initially, DNA binding by wildtype and mutant MutS for homoduplex as well as heteroduplex DNA was investigated to find out whether the active site mutations in the ATPase domain influenced DNA binding. To achieve this, the equivalent of ~15 response units (RU) of 41-bp biotinylated heteroduplex or homoduplex oligonucleotides were immobilized onto surface conjugated streptavidin tetramers (~2400 RU) (**see M.6**). Subsequently, various concentrations wildtype or mutant MutS, ranging from 0 to 1.6 µM, were injected and association as well as subsequent dissociation were monitored for 5 min.

Based on literature MutS is expected to have a higher affinity for heteroduplex DNA than homoduplex DNA, therefore binding levels were expected to be significantly lower on homoduplex DNA compared to heteroduplex DNA[12,18,42,89,90].

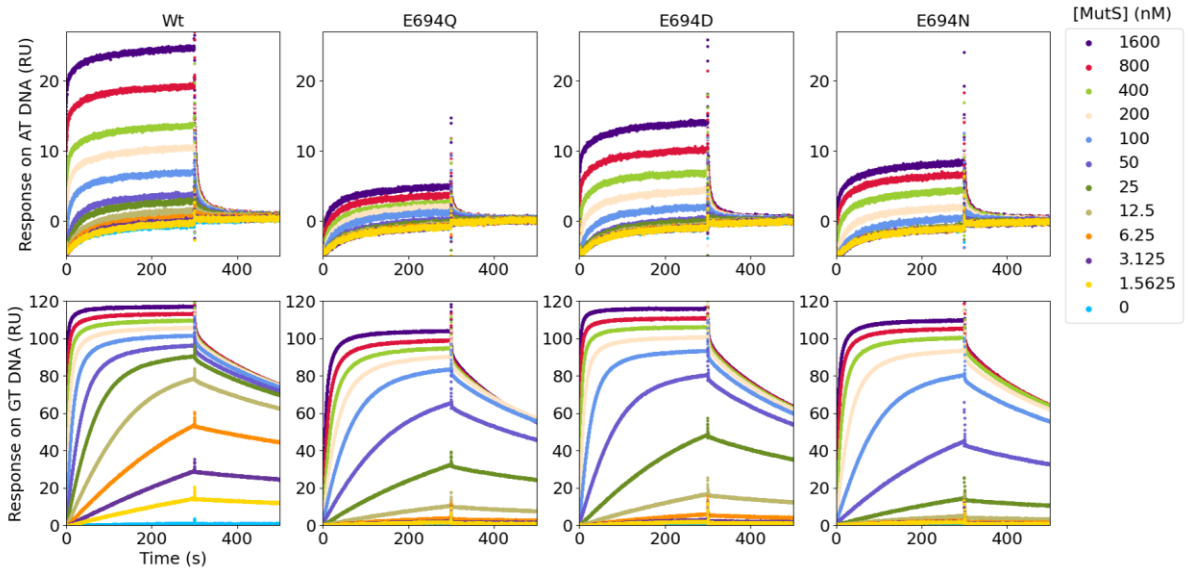

Figure 46. Exemplary SPR sensorgrams showing DNA binding by wildtype and mutant MutS at different protein concentrations*. Association and dissociation curves to homoduplex (AT, first row) and heteroduplex (GT, second row) DNA for increasing concentrations of MutS^{Wt} (first column), MutS^{E694Q} (second column), MutS^{E694D} (third column) and MutS^{E694N} (fourth column).*

As expected, both wildtype and mutant MutS showed a significantly lower binding response to homoduplex compared to heteroduplex DNA (**Fig. 46**), indicating that the active site mutations did not markedly alter the discriminatory capacity against homoduplex DNA (see below for small effect in relative discrimination of E694Q and E694N). Binding increased monotonically with increasing protein concentration, however at high concentrations (>200 nM) a significant fraction of MutS (>10%) started binding non-specifically to the DNA, as evidenced by the biphasic dissociation kinetics on mismatch-containing DNA and a marked increase in homoduplex DNA binding.

Strikingly, all MutS mutants were significantly impaired in binding to either homoduplex or heteroduplex DNA compared to the wildtype. Interestingly, binding by MutS^{E694D} was least affected, indicating the importance of the negatively charged carboxyl group of E694 in DNA binding.

Furthermore, the wildtype was observed to have the highest binding response on homoduplex DNA, reaching a maximum of ~22 RU after 5 min at a concentration of 1.6 µM. However, the mutants exhibited significantly lower binding to homoduplex DNA, reaching a maximum of ~5, ~15 and ~10 RU for MutS^{E694Q}, MutS^{E694D} and MutS^{E694N}, respectively. A similar trend was observed for heteroduplex DNA, with a maximum binding response of ~100-110 RU after 5 min at a concentration of 1.6 µM. However, whereas binding by MutS^{E694N} to homoduplex DNA seems higher than that of MutS^{E694Q} this trend is inverted for heteroduplex DNA, indicating that the discriminatory capacity is altered by the active site mutations.

R.4.3 ATP reduces DNA binding by wildtype and mutant MutS

Next, the effect of ATP on DNA binding by MutS was investigated by mixing wildtype or mutant MutS with various concentrations of ATP prior to injection. Based on literature MutS is expected to transition into a closed conformation with reduced DNA binding affinity upon ATP binding[12,15,62]. Moreover, upon ATP hydrolysis MutS is expected to revert to a state with enhanced DNA binding affinity. Therefore, reactions containing 200 nM wildtype or mutant MutS and various concentrations

of ATP (0 - 1024 µM) were injected and association as well as subsequent dissociation were monitored for 2 min.

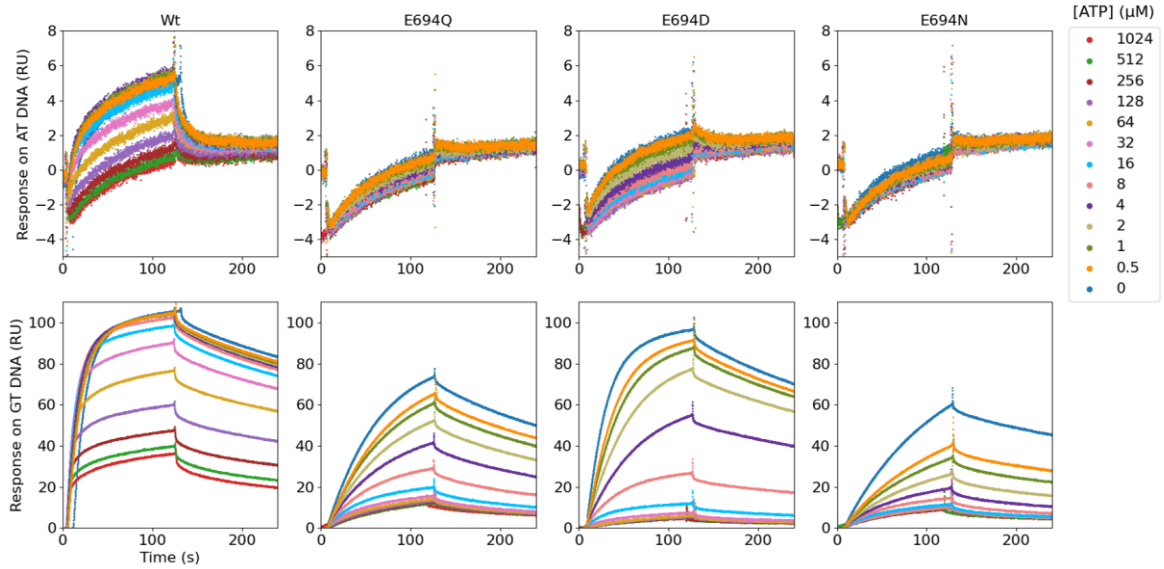

Figure 49. Exemplary SPR sensorgrams showing DNA binding by wildtype and mutant MutS premixed with different concentrations of ATP*. Association and dissociation curves to homoduplex (first row) and heteroduplex (second row) DNA for MutS^{Wt} (first column), MutS^{E694Q} (second column), MutS^{E694D} (third column) and MutS^{E694N} (fourth column) mixed with various concentrations of ATP.*

As expected, the relative binding response at the end of the 2 min association phase decreased monotonically with increasing concentration of ATP for the MutS mutants as well as the wildtype (**Fig. 49**). Moreover, as previously observed (**see R.4.2**), binding of MutS to homoduplex DNA was significantly lower compared to heteroduplex DNA, indicating that nearly all observed binding was mismatch specific.

Furthermore, the cooccurring decrease in binding with increasing ATP concentration was enhanced for the MutS mutants compared to the wildtype, with the sensitivity of MutS^{E694N} being the most extreme. This trend is in accordance with previous findings showing that ATP binding is enhanced for the MutS mutants compared to the wildtype and that the maximal steady-state ATP hydrolysis velocity is markedly reduced for the mutants (**see R.3.2.4**). Since both a reduction in ATP hydrolysis rate and enhanced ATP binding are expected to shift the equilibrium between closed ATP-bound and open ADP-unbound MutS complexes towards the closed ATP-bound state that is reported to be unable to bind to DNA[15].

Taken together, the data indicate that ATP binding induces a conformational transition in MutS leading to a state reduced in DNA binding. Moreover, sensitivity to ATP correlates with ATPase activity and ATP binding, indicating that ATP hydrolysis reverts the reduced DNA binding state of MutS to an open conformation enhanced in DNA binding.

R.4.4 Mismatch binding by MutS mutants is more sensitive to the addition of ATP than for wildtype MutS

Lastly, release of the mismatch upon ATP injection by preassembled MutS-DNA complexes was studied by preassembling wildtype or mutant MutS onto the DNA and injecting various concentrations of ATP. Addition of ATP to preassembled MutS-DNA complexes is expected to trigger nucleotide

exchange, resulting in sliding clamp formation. Since the surface immobilized oligonucleotides are not end-blocked, the sliding clamps are expected to diffuse off the free DNA end, resulting in a rapid reduction in signal.

In order to investigate this, reactions containing 200 nM wildtype or mutant MutS were injected and association was monitored for 2 min. Directly thereafter, a second solution containing varying concentrations of ATP (0 - 1024 µM) was injected and dissociation was followed for 2 min.

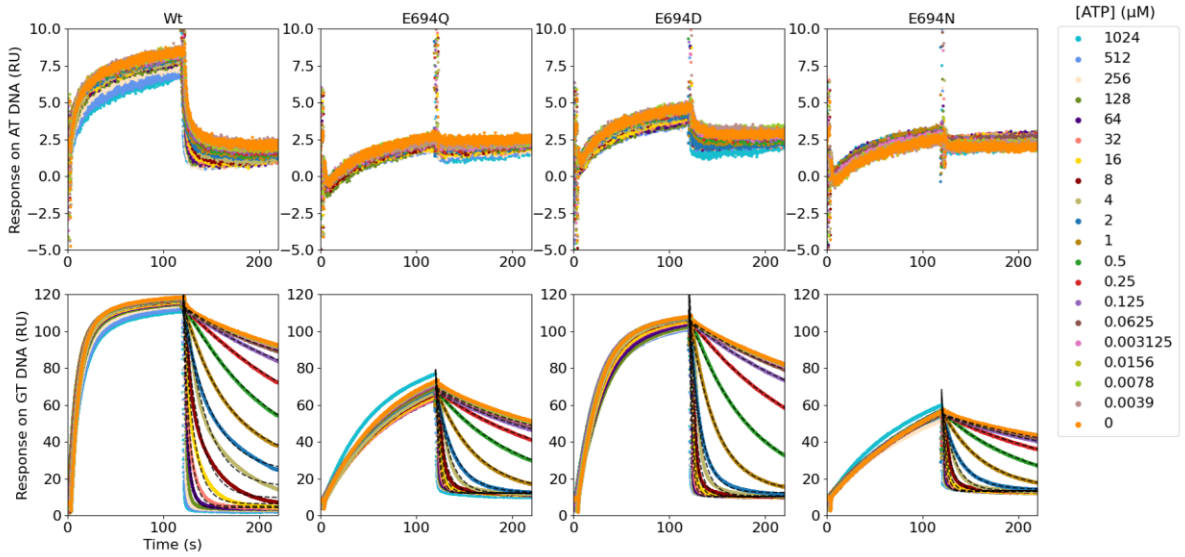

Figure 50. Exemplary sensorgrams showing the stimulatory effect of ATP on the dissociation rate of preassembled MutS-DNA complexes. *Association and dissociation curves to homoduplex (first row) and heteroduplex (second row) DNA for MutS^{Wt} (first column), MutS^{E694Q} (second column), MutS^{E694D} (third column) and MutS^{E694N} (fourth column). Exponential fits to the dissociation phase are shown as dashed black lines.*

As anticipated, the dissociation rate for both wildtype and mutant MutS monotonically increased with increasing concentration of ATP (**Fig. 50**). This trend was also observed on homoduplex DNA, although relative binding levels were significantly lower consistent with previous findings (**see R.4.2 and R.4.3**).

Furthermore, all MutS mutants were more sensitive to changes in ATP concentration compared to the wildtype. Dissociation measured for ATP concentrations ranging from 0-64 µM was well ($R^2 \geq 0.97$) fitted by exponential functions (**see M.6**) and the resulting rate constants were plotted against concentration of ATP (**Fig. 51**). Data collected at higher concentrations were excluded from the analysis, as dissociation at higher concentrations was too rapid to fit properly. To determine the concentration of ATP ($K_{\frac{1}{2}}^{ATP}$) at which half of the maximum dissociation rate is achieved, **Eq. 6** was fitted to the rates obtained from the exponential fits. The $K_{\frac{1}{2}}^{ATP}$ for MutS^{Wt}, MutS^{E694Q}, MutS^{E694N} and MutS^{E694D} were calculated to be 46 ± 4.7, 15 ± 2.0, 16 ± 3.8 and 20 ± 3.9 µM (mean ± std, N=3), respectively.

Moreover, in the limit where the concentration of ATP goes to infinity, the maximum dissociation rate (r_{max}) was fitted to be 0.39 ± 0.014, 0.34 ± 0.042, 0.47 ± 0.085 and 0.41 ± 0.060 s^{-1} for MutS^{Wt}, MutS^{E694Q}, MutS^{E694N} and MutS^{E694D}, respectively (mean ± std, N=3). These values are similar (difference < 1.5-fold), indicating that the maximum rate at which the DNA can be released is not substantially altered for the MutS mutants.

$$r([ATP]) = \frac{r_{max}[ATP]}{[ATP] + K_{\frac{1}{2}}^{ATP}} \quad (6)$$

Collectively, the results suggest that the MutS mutants exhibit a higher degree of responsiveness to alterations in ATP concentration compared to the wildtype. This is likely due to an increase in the binding affinity of the mutants for ATP, which is supported by the results of the colorimetric ATPase assay (**see R.2.4.4**).

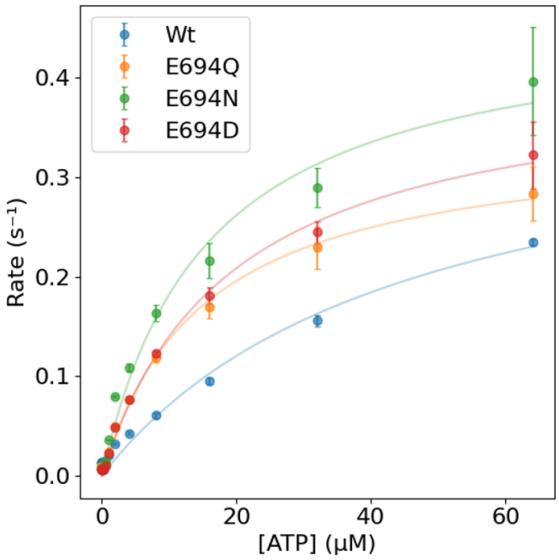

MutS	$K_{\frac{1}{2}}^{ATP}$ (μM)	r_{max} (s^{-1})
Wild type	46 ± 4.7	0.39 ± 0.014
E694Q	15 ± 2.0	0.34 ± 0.042
E694N	16 ± 3.8	0.47 ± 0.085
E694D	20 ± 3.9	0.41 ± 0.060

***Figure 51. The MutS mutants are enhanced in ATP binding compared to the wildtype**. **Left**, Rates obtained from exponential fits to the dissociation phase at various concentrations of ATP as shown in **Fig. 50** for $MutS^{Wt}$ (blue), $MutS^{E694Q}$ (orange), $MutS^{E694D}$ (red) and $MutS^{E694N}$ (green). Fits are shown as solid lines. **Right**, Table summarizing the fitted values. All data is represented as mean ± std, N=3.*

6

Results

MutH recruitment & activation

R.5 State-of-the-art in vitro assays to investigate pathway activation

To further functionally characterize the MutS mutants, the kinetics of MMR pathway initiation were investigated in the context of an *in vitro* reconstituted *E. coli* MMR pathway, enabling investigation of the kinetics of MMR initiation by monitoring MutH recruitment and activation kinetics.

R.5.1 Reconstituted in vitro gel-electrophoresis based MutH activation assay

To investigate *E. coli* MMR initiation an *in vitro* reconstituted gel-electrophoresis based MutH activation assay was employed. In this assay purified wildtype or mutant MutS, MutL and MutH are combined in various ways, depending on the experiment, with fluorescently labelled heteroduplex (GT#1^{AF647}) or homoduplex (AT#1^{AF647}) DNA constructs containing a hemi-methylated GATC site (**see M.7**) which is irreversibly incised once MutH is activated. The fraction of incised DNA is therefore a marker for the amplitude of MutH activation at any given timepoint. Since incision of the unmethylated strand serves as entry point for downstream MMR activities this assay reports the amplitude of MMR initiation (**Fig. 52**).

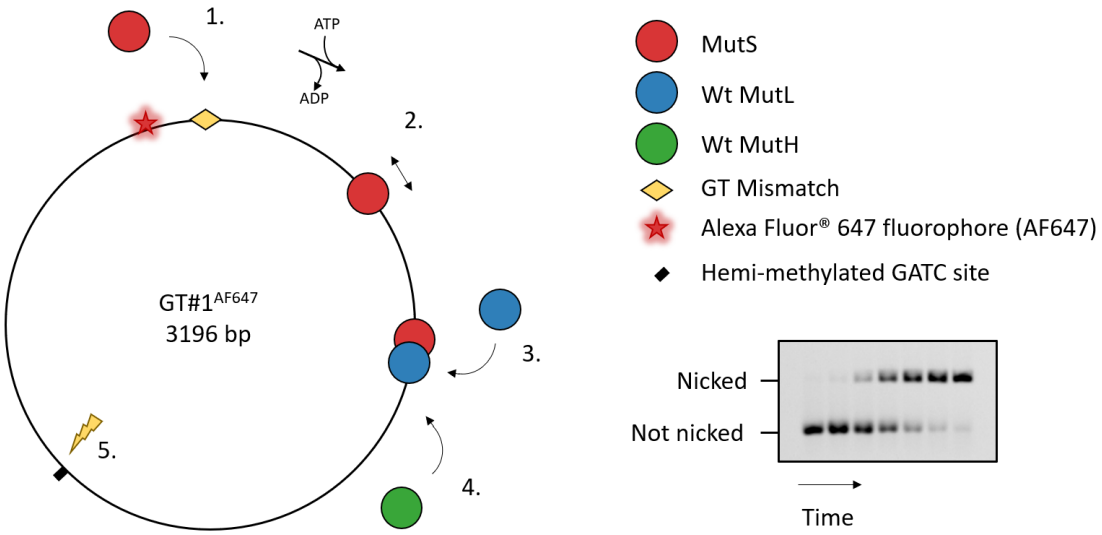

Figure 52. Schematic representation of MutH activation assay principle. *Following mismatch binding (**1.**) and sliding clamp formation (**2.**) MutS is able to recruit and activate MutL (**3.**) and subsequently MutH (**4.**) ultimately leading to an incision at the hemi-methylated GATC site (**5.**). Bottom right shows and exemplary 0.8% agarose gel in which the progression from unnicked to nicked substrate is visualized over time.*

Activation of MutH results in the incision of the DNA constructs at the GATC site, specifically 5' to the Guanine in the unmethylated strand GATC motif, causing the DNA to transition from a covalently closed to a relaxed circular conformation. To determine the extent of strand incision over time, samples are taken and protein activity is terminated by aliquoting these in an equal volume of stop solution containing sodium dodecyl sulphate as denaturing agent.

Subsequently, the samples are run on a 0.8% agarose gel containing 2 µM chloroquine for 16 h at 20 V to separate the reaction products. Chloroquine is a DNA intercalator, known to positively supercoil DNA[91]. When the plasmid is nicked, circularity will remain, but nick in one strand will permit rotation

around the phosphodiester bond in the other strand, causing the DNA to remain relaxed. The nicked conformation is therefore less compact than the supercoiled conformation of the uncut substrate, hence it is expected to run slower during electrophoresis, resulting in separation of the incised and uncut reaction products on the gel.

Following gel-electrophoresis, the separated products can be quantified by measuring the fluorescence which directly correlates with the number of DNA molecules, since each molecule contains exactly 1 fluorophore. In this manner it is possible to quantitatively monitor incision, and therefore pathway activation, over time in a reconstituted *E. coli* MMR system.

R.5.1.1 On short timespans only MutS^{Wt} results in significant MutH activation under conditions mimicking in vivo MMR

To mimic *in vivo E. coli* MMR initiation, where MutS, MutL, MutH, and ATP are present prior to mismatches which arise during replication, 100 nM of either wildtype or mutant MutS was incubated with 100 nM MutL, 50 nM MutH and 1 mM ATP in assay buffer A for 5 min (**see M.7**). Subsequently, 0.5 nM GT#1^{AF647} or AT#1^{AF647} (homoduplex control) was introduced and the reactions were monitored for 1 min (**Fig. 53a**). The samples collected during the experiment were then visualized and quantified as described in section **M.7.2**.

Under these experimental conditions MutS is expected to be in a closed ATP-bound state prior to addition of DNA[15]. Therefore, MutS has to hydrolyse the bound ATP to transition to an open conformation, enabling mismatch binding and subsequently pathway activation. Since ATP is in large molar excess compared to the DNA, it is likely for MutS to encounter another ATP molecule instead of DNA once ATP is hydrolysed and the nucleotide binding site is vacated. Therefore it is possible that the complex will have to repeatedly complete the hydrolysis cycle before being able to bind to the DNA. Based on the experimentally determined values for the maximum steady state hydrolysis velocity, the wildtype is expected to be able to do so rapidly, however due to severely impaired ATPase activity the mutants are not, effectively lowering the affinity for DNA.

As anticipated, the majority of fluorescently labelled DNA was incised within 1 min in the presence of MutS^{Wt} (**Fig. 53b**). The data was well fitted (R^2 = 0.997) to a sigmoidal function with a rate of 1.4 ± 0.08 min^{-1} (mean ± std, N=3). Only minor MutH activation was observed when using MutS^{E694Q} (~2% of substrate incised after 1 min), however no activation was observed when either MutS^{E694D} or MutS^{E694N} was employed. Furthermore, MutH activation was mismatch specific as evidenced by the low amplitude of activation (~4%) observed when substituting the heteroduplex (GT#1^{AF647}) with homoduplex (AT#1^{AF647}) DNA constructs, containing the Watson-Crick AT base pair at the position of the GT mismatch in GT#1^{AF647}. This low amplitude of activation is likely due to stochastic activation of the system, which is known to occur on homoduplex DNA and/or in the presence of lesions on a small fraction of the homoduplex DNA batch. Furthermore, the observed mismatch specific activation of MutH is in accordance with the reduced affinity of MutS^{Wt} for homoduplex compared to heteroduplex DNA as determined by SPR (**see R.4.2**). Additionally, no activation was observed when MutS, MutL, MutH, or ATP was substituted with an equal volume of buffer (data not shown), indicating that the observed activation is pathway specific.

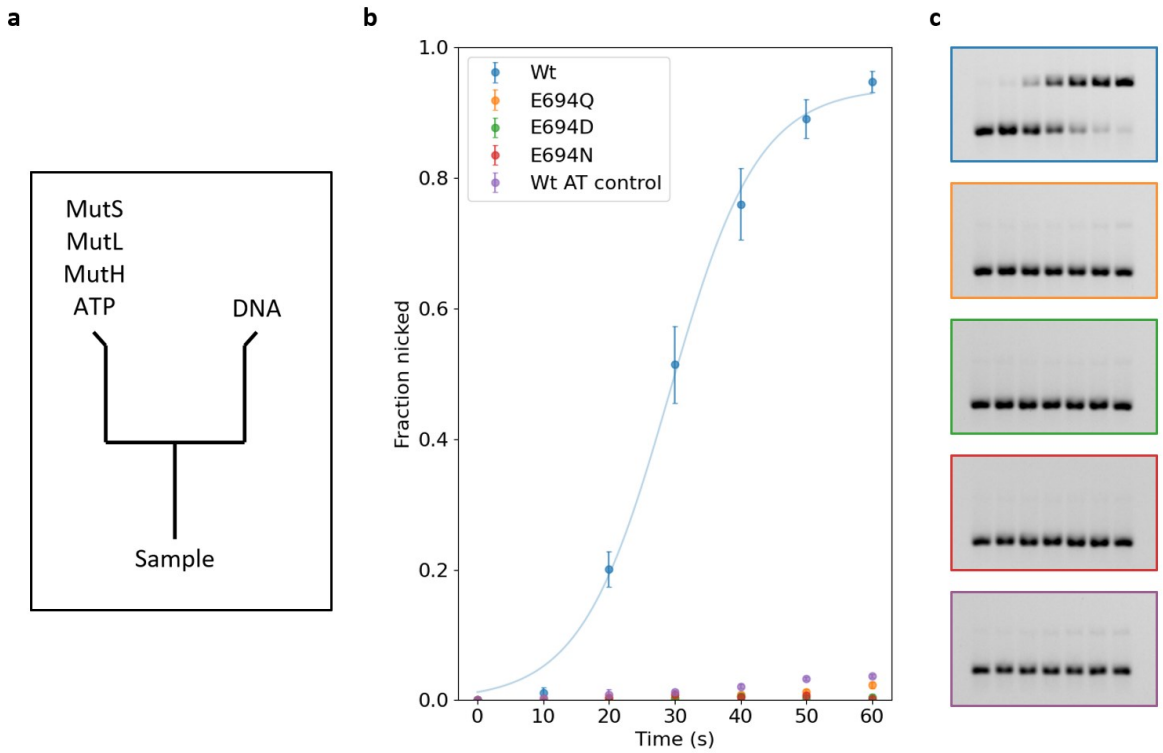

***Figure 53. MutH activation during 1 min by wildtype and mutant MutS. a**, Schematic summary of the order of addition. **b**, Activation over time is shown for MutS^{Wt} (blue), MutS^{E694Q} (green), MutS^{E694D} (red), MutS^{E694N} (purple) and a homoduplex control (orange). Sigmoidal fit to data obtained using MutS^{Wt} is shown as solid line. Data is shown as mean ± std, N=3. **c**, Exemplary gel data of corresponding traces.*

Collectively the data demonstrate that under these conditions and on this timescale MutS^{Wt} can bind to the mismatch and undergo nucleotide-mediated conformational changes, resulting in the recruitment and activation of MutL and subsequently MutH, whereas the mutants cannot.

R.5.1.2 Over extended timescales the MutS mutants induce significant MutH activation as well

Subsequently, reactions containing mutant MutS were monitored over an extended period of time in order to investigate whether activation under these conditions correlates with ATPase activity, as expected. The experimental conditions described in the previous section were replicated. However, in this instance, MutH activation by MutS^{E694Q} and MutS^{E694D} was monitored by intermittently sampling the reactions every 1.5 min for a duration of 45 min. Additionally, MutH activation in the presence of MutS^{E694N} was monitored for 4 h by intermittently sampling the reactions every 30 min, due to extremely low activity.

Since the V_{max} of MutS^{E694Q} was calculated to be larger than that of MutS^{E694D} and the V_{max} of MutS^{E694D} was larger than that of MutS^{E694N}, MutS^{E694Q} was expected to result in faster MutH activation than MutS^{E694D} which in turn was expected to result in faster activation than MutS^{E694N}.

Reactions conducted using AT#1^{AF647} did not result in significant activation for any of the MutS mutants, indicating all observed activity was mismatch specific. As anticipated, MutS^{E694Q} caused MutH to be activated more rapidly than MutS^{E694D} as all DNA was already incised within 30 min, whereas this took significantly longer when MutS^{E694D} was employed (**Fig. 54**). Furthermore, MutH activation in the

presence of MutS^{E694N} was much slower compared to activation in the presence of any of the other MutS variants (**Fig. 55**).

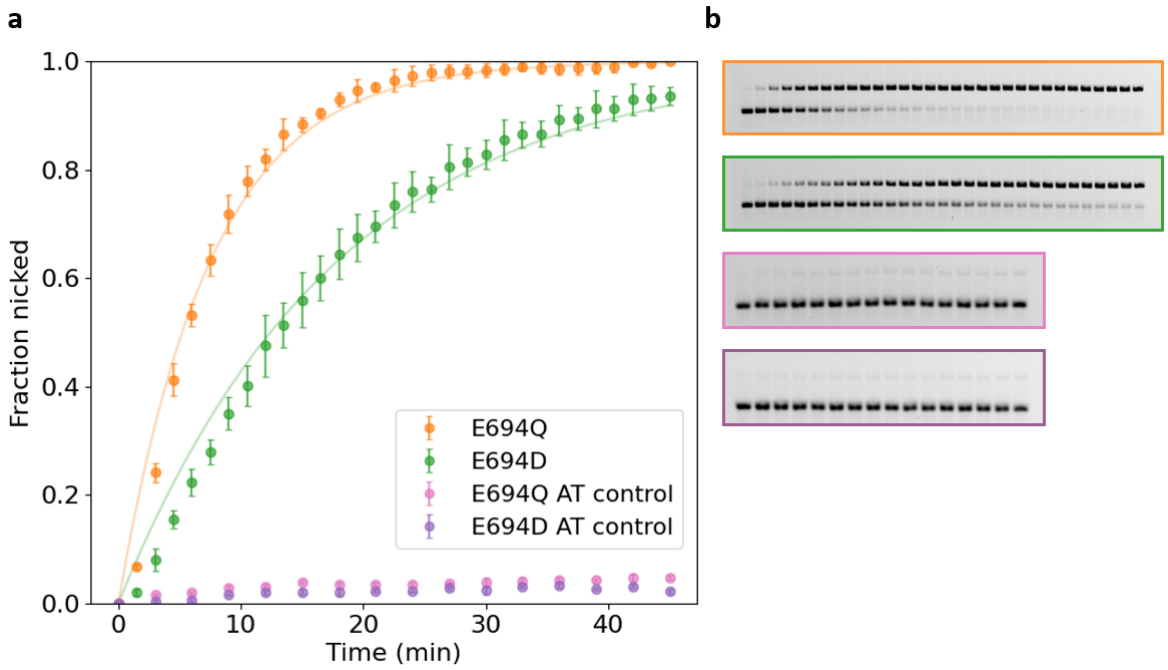

Figure 54. MutH activation during 45 min by MutS^{E694Q} and MutS^{E694Q}. a, *Activation over time is shown for MutS^{E694Q} and MutS^{E694D} on heteroduplex (orange and green, respectively) as well as homoduplex (pink and purple, respectively) DNA. Data is shown as mean ± std, N=3.* ***b****, exemplary gel data of corresponding traces.*

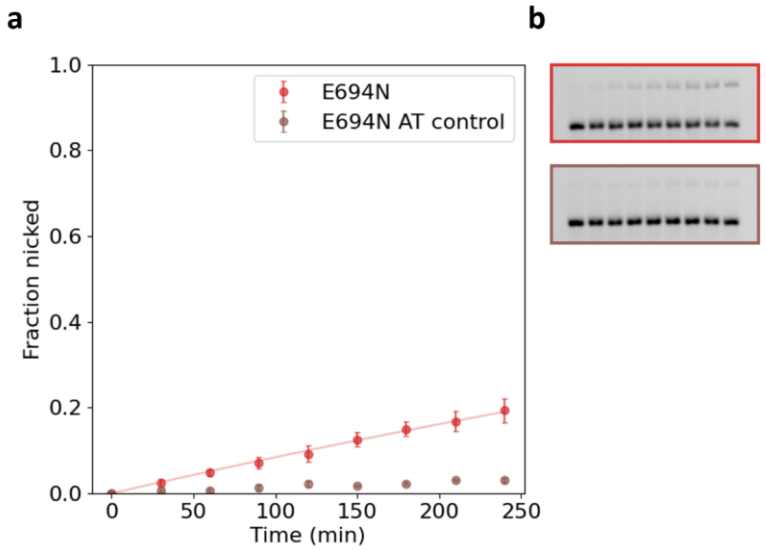

Figure 55. MutH activation during 4 H by MutS^{E694N}. a, *Activation over time is shown for MutS^{E694N} heteroduplex (red) and homoduplex (brown) DNA. Data is shown as mean ± std, N=3.* ***b****, Exemplary gel data of corresponding traces.*

Finally, by fitting an exponential function (**see M.7 Eq. 2, with $\alpha = 1$ and $r_2 = 0$**) to the average fraction of nicked heteroduplex DNA over time, the rate of MutH activation was determined to be 0.13 ± 0.01 min^{-1}, 0.056 ± 0.006 min^{-1} and 0.00088 ± 0.00014 min^{-1} (mean ± std, N=3) for MutS^{E694Q}, MutS^{E694D} and MutS^{E694N}, respectively. The coefficient of determination (R^2) was computed to be 0.997 for the fit to data obtained using MutS^{E694N} and 0.988 for fits to data obtained using MutS^{E694Q} and MutS^{E694D}, indicating that the models agree well with the acquired data.

Taken together, the data shows that over extended periods of time the mutants also lead to significant mismatch specific MutH activation under conditions mimicking *in vivo* MMR. Moreover, activation rates obtained by exponentially fitting progressive MutH activation reveal a correlation between MutH activation and ATPase activity (**Table 2**).

MutS	V_{max} (min^{-1})	Rate (min^{-1})
Wild type	1.8 ± 0.42	1.4 ± 0.08
E694Q	0.19 ± 0.017	0.13 ± 0.01
E694D	0.052 ± 0.0074	0.056 ± 0.006
E694N	0.012 ± 0.0012	0.00088 ± 0.00014

Table 2. ATPase activity of wildtype and mutant MutS correlates with MutH activation under conditions mimicking in vivo MMR. *Nicking rates determined for wildtype and mutant MutS as well as maximum steady-state hydrolysis velocities are shown. Data is shown as mean ± std, N≥3.*

R.5.1.3 Preassembly of MutS on DNA results in enhanced MutH activation

To investigate whether preassembly of MutS onto the DNA would restore or resolve any differences observed in MutH activation between wildtype and mutant MutS, MutS was preassembled to the DNA prior to addition of MutL, MutH and ATP. According to prevailing MMR models the post-mismatch recognition states of MutS are ATP hydrolysis independent. These models state that ATP hydrolysis is only required for the dissociation of MutS from the DNA or return to a mismatch-binding competent state. Consequently, it is expected that preassembly of the MutS mutants onto the mismatch would either restore MutH activation or resolve any differences in MutH activation that are dependent on ATP hydrolysis.

To study this, reactions containing 100 nM of either wildtype or mutant MutS were incubated with 0.5 nM GT#1^{AF647} for 1 min. Subsequently, a mixture of 100 nM MutL, 50 nM MutH and 1 mM ATP was supplemented and MutH activation was monitored by intermittently sampling the reactions every 10 s for 1 min (**Fig. 56a**).

In the presence of MutS^{Wt} almost all fluorescently labelled DNA molecules were incised within 1 min (**Fig. 56b**). All MutS mutants led to enhanced MutH activation compared to experiments in which MutS was not prebound to the DNA (**see R.5.1.1**). Strikingly, the different MutS mutants showed varying degrees of MutH activation, which corresponded with the ATPase activity of the mutants. All data was well fitted ($R^2 \geq 0.99$) by sigmoidal functions. In the limit of time to infinity, MutH activation amplitudes were calculated to be (mean ± std, N=3) 95 ± 1.4%, 50 ± 6.1%, 43 ± 2.2% and 8.2 ± 0.81% for MutS^{Wt}, MutS^{E694Q}, MutS^{E694D} and MutS^{E694N}, respectively. These results suggest that bypass of mismatch binding enables MutH activation by the MutS mutants and that there may be a step during MMR initiation that is dependent on ATP hydrolysis by the MutS sliding clamp.

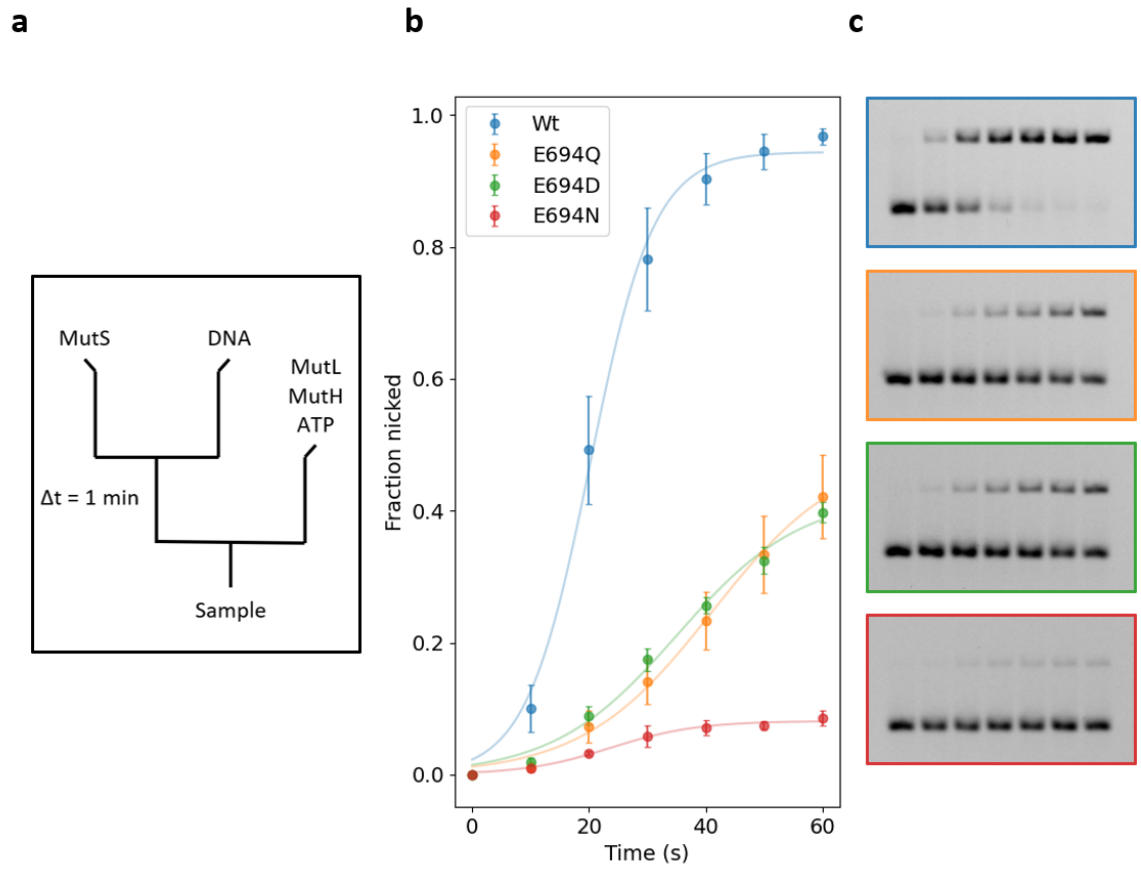

Figure 56. MutH activation by MutS prebound to GT#1^{AF647}. ***a****, Schematic summary of the order of addition.* ***b****, MutH activation over time is shown for MutS^{Wt} (blue), MutS^{E694Q} (orange), MutS^{E694D} (green) and MutS^{E694N} (red). Sigmoidal fits are shown as solid lines. Data is shown as mean ± std, N=3.* ***c****, Exemplary gel data of corresponding traces.*

R.5.1.4 Extent of MutH activation is dependent on incubation time prior to addition of MutL and MutH

To further investigate whether the correlation described in the previous section (**see R.5.1.3**) might be due to a yet unknown ATP hydrolysis dependent conformational transition of the MutS sliding clamp, we hypothesised that increasing the incubation period of sliding clamp MutS prior to addition of MutL and MutH would increase the amplitude of MutH activation observed in the presence of the MutS mutants. By introducing this incubation period between sliding clamp formation and addition of MutL as well as MutH, the MutS sliding clamp is allowed to hydrolyse ATP such that it is able to transition into a different conformational state. Therefore, over time an increasing fraction of the sliding clamp population would mature into the post hydrolysis state, resulting in faster MutL and subsequently MutH activation.

To investigate whether there is a time dependency, 100 nM wildtype or mutant MutS was incubated with 0.5 nM GT#1^{AF647} for 1 min. Subsequently, 1 mM ATP was supplemented and the reactions were incubated for 2.5 H. Thereafter, a mixture of 100 nM MutL and 50 nM MutH was supplemented and MutH activation was monitored by intermittently sampling the reactions every 10 s for 1 min (**Fig. 57a**).

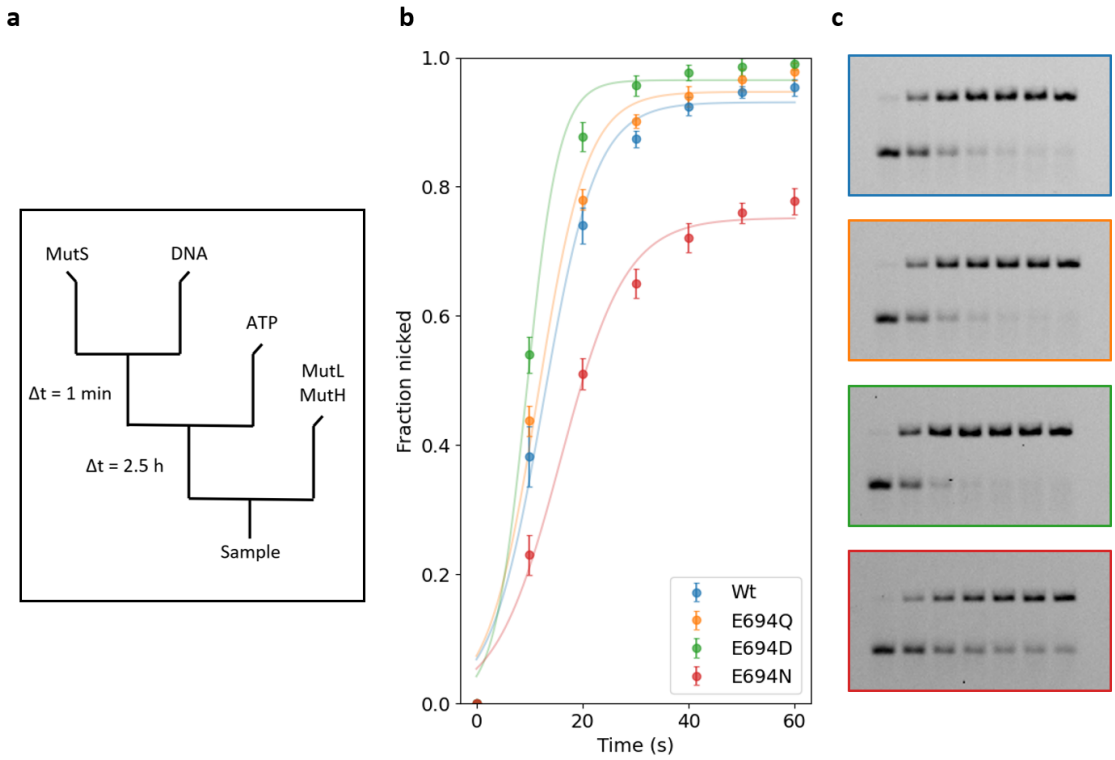

Figure 57. Preincubating preassembled MutS sliding clamps prior to addition of MutL and MutH enhances the extent of MutH activation. ***a****, Schematic summary of the order of addition.* ***b****, MutH activation over time is shown for MutS^{Wt} (blue), MutS^{E694Q} (orange), MutS^{E694D} (green) and MutS^{E694N} (red). Sigmoidal fits are shown as solid lines. Data is shown as mean ± std, N=3.* ***c****, Exemplary gel data of corresponding traces.*

All MutS mutants led to enhanced MutH activation compared to identical experimental conditions in which the reactions were not incubated prior to addition of MutL and MutH (**see R.5.1.3, Fig. 57b**). All data was well fitted ($R^2 \geq 0.99$) by sigmoidal functions and in the limit of time to infinity, MutH activation amplitudes were calculated to be (mean ± std, N=3) 93 ± 1.1%, 95 ± 1.4%, 97 ± 1.2% and 75 ± 1.8% for MutS^{Wt}, MutS^{E694Q}, MutS^{E694D} and MutS^{E694N}, respectively. Moreover, MutH activation was significantly faster after the 2.5 h incubation for MutS^{Wt} (**Fig. 58**), as evidenced by the time to reach half of the maximum obtainable MutH activation amplitude which was reduced from 20 ± 2.1 s to 13 ± 1.0 s (mean ± std, N=3).

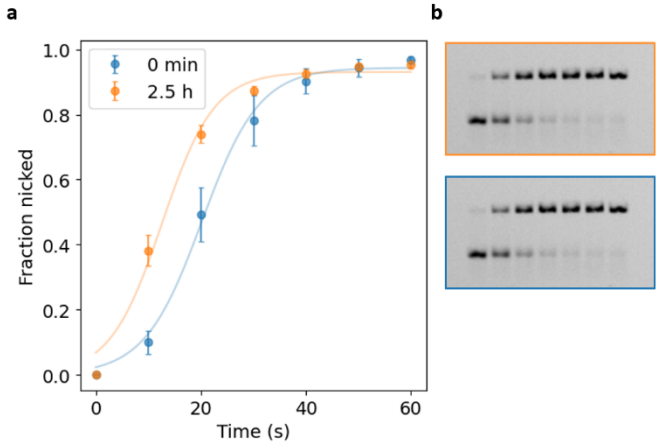

Figure 58. Preincubation of preassembled MutS^{Wt} sliding clamps prior to addition of MutL and MutH leads to faster MutH activation. ***a****, MutH activation over time is shown for MutS^{Wt} which was not incubated (blue) or incubated for 2.5 h (orange) prior to addition of MutL and MutH. Sigmoidal fits are shown as solid lines. Data is shown as mean ± std, N=3.* ***b****, Exemplary gel data of corresponding traces.*

The effect of the 2.5 h incubation was most significant for experiments conducted using MutS^{E694N} which upon prebinding resulted in an approximate nine-fold increase in MutH activation. Therefore, to investigate this phenomenon in more detail, the experiment was repeated for various incubation times ranging from 1 min to 2.5 h in the presence of 100 nM MutS^{E694N}.

As anticipated, the amplitude of MutH activation monotonically increased with increasing incubation time (**Fig. 59a, see appendix Fig. 72 for gel data**). Moreover, the data was well fitted ($R^2 \geq 0.98$) by exponential functions. Plotting the amplitude of MutH activation reached in the limit of time to infinity versus incubation time revealed an exponential dependency (**Fig. 59b**). Indeed, the amplitude of MutH activation achieved as time tends to infinity was well fitted ($R^2 \geq 0.99$) by an exponential. From this fit the incubation time to reach half of the maximum achievable MutH activation amplitude was calculated to be 10.5 min.

Furthermore, the fitted MutH activation rates were similar. The time needed to reach half of the maximum amplitude of MutH activation after addition of MutL and MutH ($t_{\frac{1}{2}}$) was independent of incubation time prior to addition of MutL and MutH (**Fig. 59c**). Moreover, the mean $t_{\frac{1}{2}}$ was calculated to be 21.2 ± 1.5 s which is similar to the rate of wildtype MutS, see above.

Collectively, the data clearly indicate that the amplitude of MutH activation correlates with incubation time of the MutS sliding clamp prior to addition of MutL and MutH, whereas the rate of activation is independent of incubation time. Suggesting that the MutS sliding clamp matures in a time-dependent fashion, resulting in enhanced pathway activation.

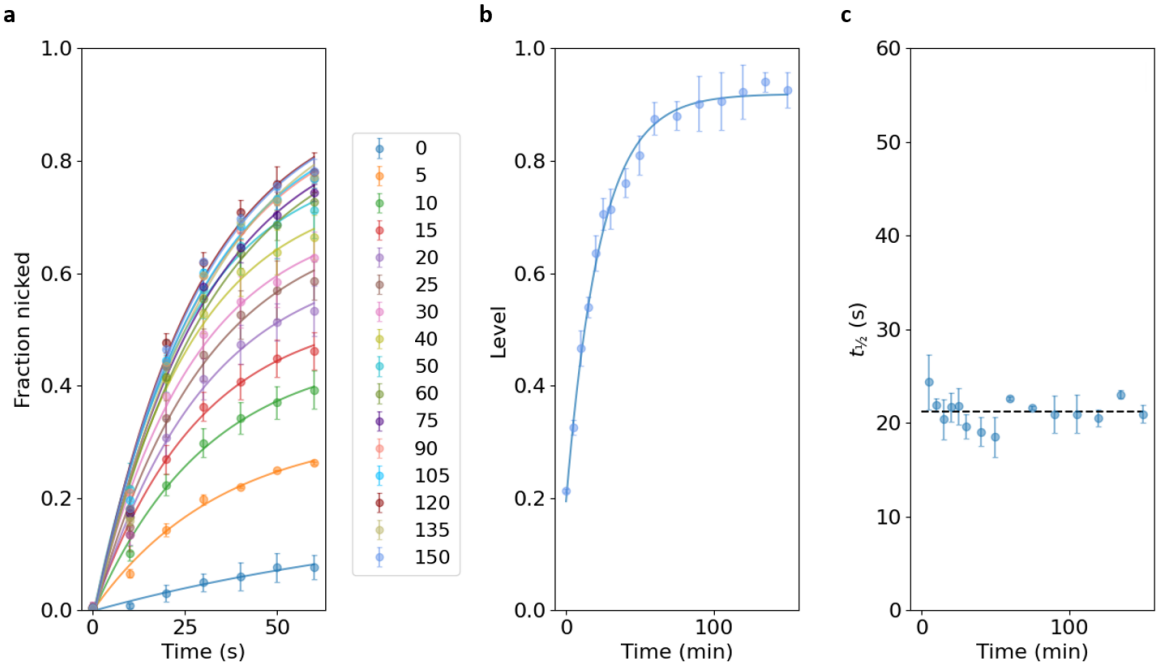

***Figure 59. Incubation time of MutS^{E694N} sliding clamps correlates with extent of MutH activation. a**, MutH activation monitored for 2 min after various incubation periods with ATP. Colored legend denotes incubation time in min prior to addition of MutL and MutH. **b**, Fitted plateau values from **a** plotted versus incubation time with ATP. **c**, Fitted MutH activation rates from **a** plotted versus incubation time with ATP. Fits are shown as solid lines. Data is shown as mean ± std, N=3.*

R.5.1.5 End-blocked competitor oligonucleotides prevent multiple loading

Although the correlation found in the previous section might be due to a hydrolysis-dependent conformational change of the MutS sliding clamp, the observed time dependency could also arise by loading of multiple MutS complexes over time on the same DNA molecule once the mismatch site is vacated, a phenomenon we term "multiple loading". The longer the system is kept in a state where this is allowed to take place, the more MutS sliding clamps accumulate on the same DNA molecule. Once MutL and MutH are supplemented the concentration of sliding clamps would therefore be significantly higher, resulting in enhanced MutH activation (**Fig. 60**).

Additionally, it could be that MutS^{E694N} complexes which initially failed to form sliding clamps dissociated from the DNA and were able to slowly bind another DNA molecule in a second attempt. If given enough time this process could repeat until the complex was able to successfully form a sliding clamp, leading to enhanced MutH activation with increasing incubation time.

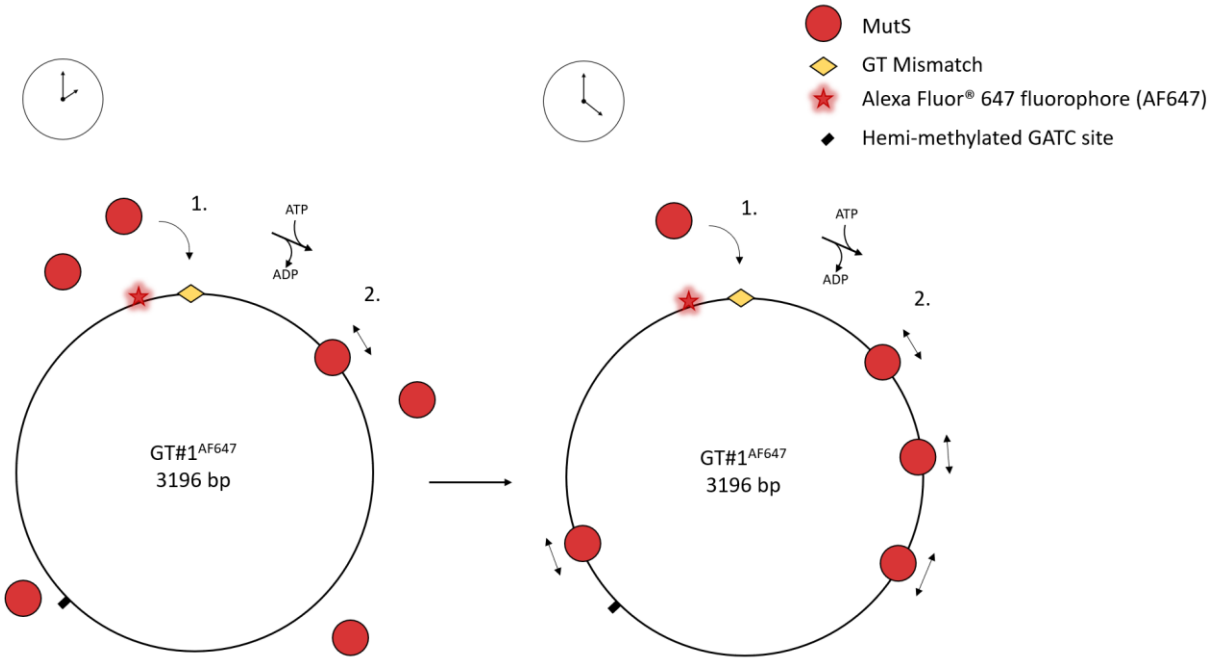

Figure 60. The "multiple loading" principle. *Following mismatch binding (**1.**) and sliding clamp formation (**2.**) the mismatch site is vacated and another MutS molecule from solution is able to bind to the mismatch and form a sliding clamp as well, resulting in accumulation of sliding clamps over time.*

Therefore we established single turnover conditions wherein only the MutS initially bound to the mismatch was able to proceed and activate MutH. To this end, 41 bp long dsDNA oligonucleotide competitors end-blocked with streptavidin tetramers (trap) were employed. The trap molecules contain a centrally located GT mismatch to which MutS is able to bind. However, due to the end-blocks MutS is "trapped" on the oligonucleotide once bound. Since the oligonucleotides are only 41 bp in length MutS can be trapped but not MutL. We hypothesised that supplementing a molar excess of trap mixed with ATP to preassembled MutS-mismatched DNA complexes would inhibit additional loading after mismatch release by the first MutS complex, resulting in the formation of exactly one MutS sliding clamp on each DNA construct and preventing additional loading on DNA molecules that failed to retain the MutS sliding clamps during the preloading phase, ensuring only single turnover events were observed (**Fig. 61**).

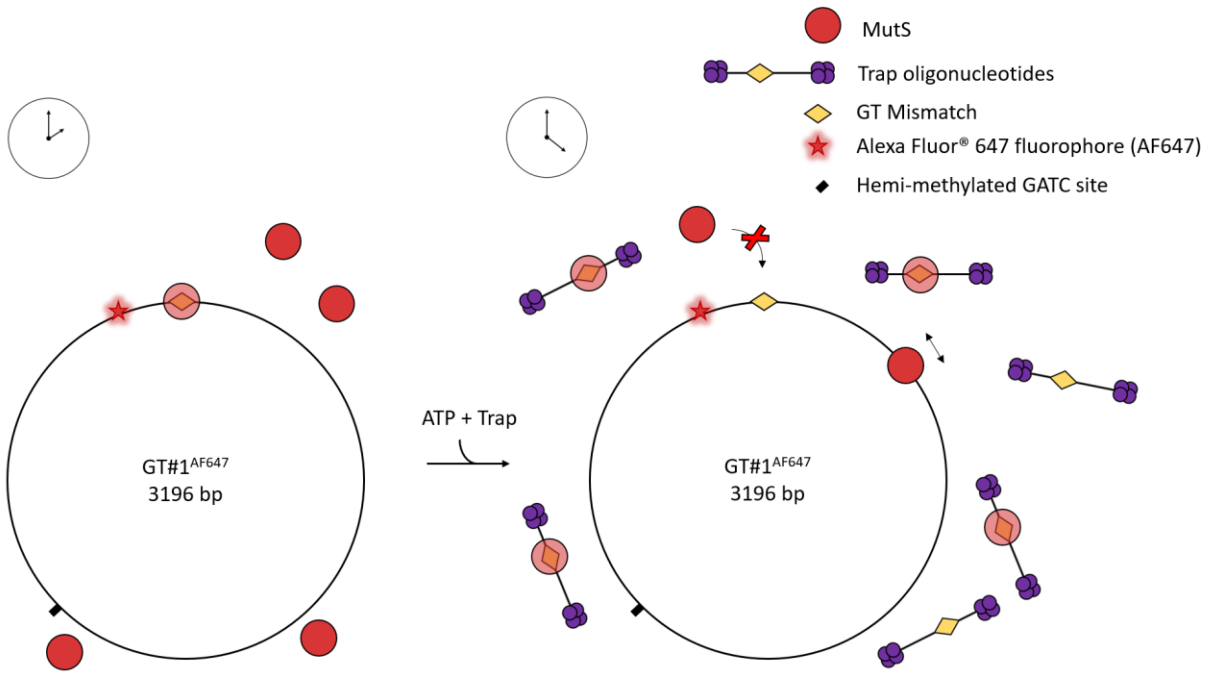

Figure 61. Competitor oligonucleotides prevent multiple loading. *Following mismatch binding (**1.**) and sliding clamp formation (**2.**) the mismatch site is vacated and mismatch binding by additional MutS complexes from solution is prevented by supplementing a molar excess of competitor oligonucleotides, resulting in a single sliding clamp per fluorescently labelled DNA construct.*

Initially, the effect of the trap was characterized on MutH activation in the presence of $MutS^{Wt}$. Therefore, 100 nM $MutS^{Wt}$ was incubated with 0.5 nM $GT\#1^{AF647}$ for 1 min. Subsequently, a mixture of 1 µM trap (2000-fold molar excess over $GT\#1^{AF647}$ and 10-fold over protein), 100 nM MutL, 50 nM MutH and 1 mM ATP was supplemented and the reaction was intermittently sampled for 2 min every 10 s (**Fig. 62c, "Trap"**).

Based on findings by Hermans et al. (2016) the trap was expected to significantly reduce the extent of MutH activation to approximately 50% maximum amplitude[75]. Moreover, based on these results, mixing a molar excess of trap molecules with $GT\#1^{AF647}$ was expected to inhibit almost all incision.

As expected, MutH activation reached a maximum amplitude of ~40% in a 2 min timespan, indicating that the trap resulted in a marked decrease in the amount of $GT\#1^{AF647}$-bound $MutS^{Wt}$, likely due to competition with $GT\#1^{AF647}$ (**Fig. 62a**). Alternatively, this could indicate that only 40% of the DNA was able to retain MutS sliding clamps during the first single turnover. The data was well ($R^2 = 0.99$) fitted by an exponential. According to the fit, in the limit as time tends to infinity 46 ± 1.2% of the DNA would be incised at a rate of 1.2 ± 0.062 min^{-1}.

Furthermore, negative control reactions in which 100 nM $MutS^{Wt}$ was incubated with 0.5 nM $GT\#1^{AF647}$ mixed with 1 µM trap for 1 min and subsequently supplemented with 100 nM MutL, 50 nM MutH and 1 mM ATP showed no MutH activation, indicating that all MutS complexes were sequestered by the trap before being able to bind to $GT\#1^{AF647}$ (**Fig. 62c, "Trap first"**). Additionally, positive control reactions in which 100 nM $MutS^{Wt}$ was incubated with 0.5 nM $GT\#1^{AF647}$ for 1 min after which a mixture of 2 µM streptavidin tetramer, 100 nM MutL, 50 nM MutH and 1 mM ATP but no trap oligonucleotides was supplemented, resulted in maximum MutH activation (**Fig. 62c, "Mock"**). Fitting the data by a sigmoidal function ($R^2 = 0.99$) revealed that in the limit as tends to infinity all DNA is incised at a rate of 2.14 ± 0.099 min^{-1}.

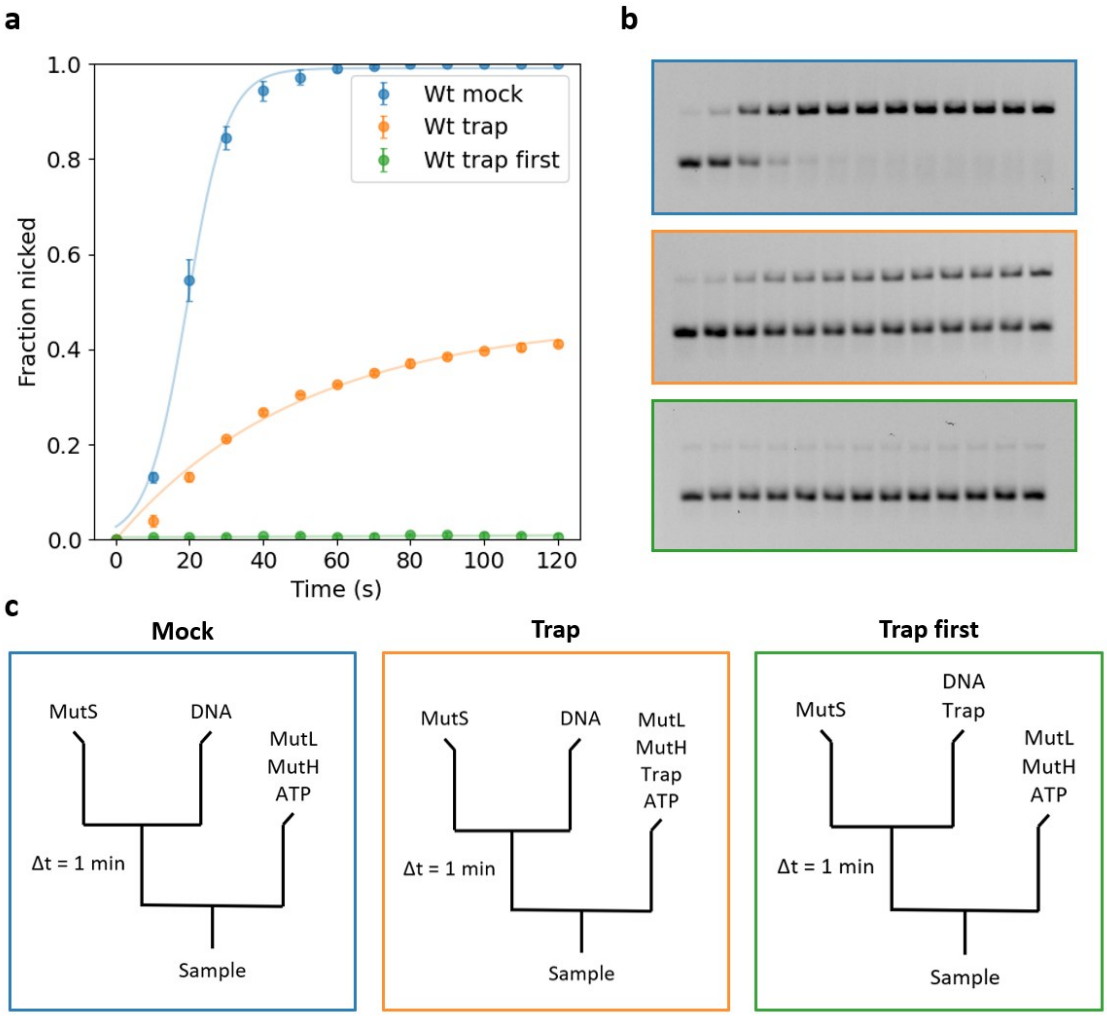

Figure 62. The effect of trap oligonucleotides on MutH activation by MutS^{Wt}. ***a****, MutH activation over time is shown for MutS^{Wt} in the absence of the trap (blue) or presence of trap either mixed with (green) GT#1^{AF647} or MutL, MutH and ATP (orange). Fits are shown as solid lines. Data is shown as mean ± std, N=3.* ***b****, Exemplary gel data of corresponding traces.* ***c****, Schematic summary of the order of addition for corresponding traces.*

Taken together the data indicate that the trap successfully prevents multiple loading by sequestering all MutS not bound to GT#1^{AF647}, enabling investigation of MutH activation on DNA constructs bound by a single MutS complex in bulk, although at the cost of reduction in signal, in accordance with findings by Hermans et al. (2016)[75].

R.5.1.6 MutH activation by the MutS mutants is biphasic and takes significantly longer than activation by MutS^{Wt} in the presence of trap oligonucleotides

Subsequently, MutH activation by the MutS mutants was investigated under single turnover conditions to find out whether MutH activation correlates with ATPase activity. If there is a hydrolysis-dependent conformational transition in the MutS sliding clamp which is required to activate MutH, the expectation is that under single turnover conditions MutH activation correlates with ATPase activity. However, it should be noted that one of the assumptions underlying this hypothesis is that the hierarchy in ATPase activity of the different MutS mutants, as determined by measuring the

maximum steady-state velocity in the absence of DNA, is similar to the hierarchy in ATPase activity on DNA.

Therefore, 100 nM MutS^{E694Q}, MutS^{E694D} or MutS^{E694N} was incubated with 0.5 nM GT#1^{AF647} for 1 min. Subsequently, a mixture of 1 µM trap (2000-fold molar excess over DNA, 10-fold molar excess over MutS), 100 nM MutL, 50 nM MutH and 1 mM ATP was supplemented and the reaction was intermittently sampled. Reactions conducted using MutS^{E694Q} and MutS^{E694D} were monitored for 30 min and reactions conducted using MutS^{E694N} for 3 h.

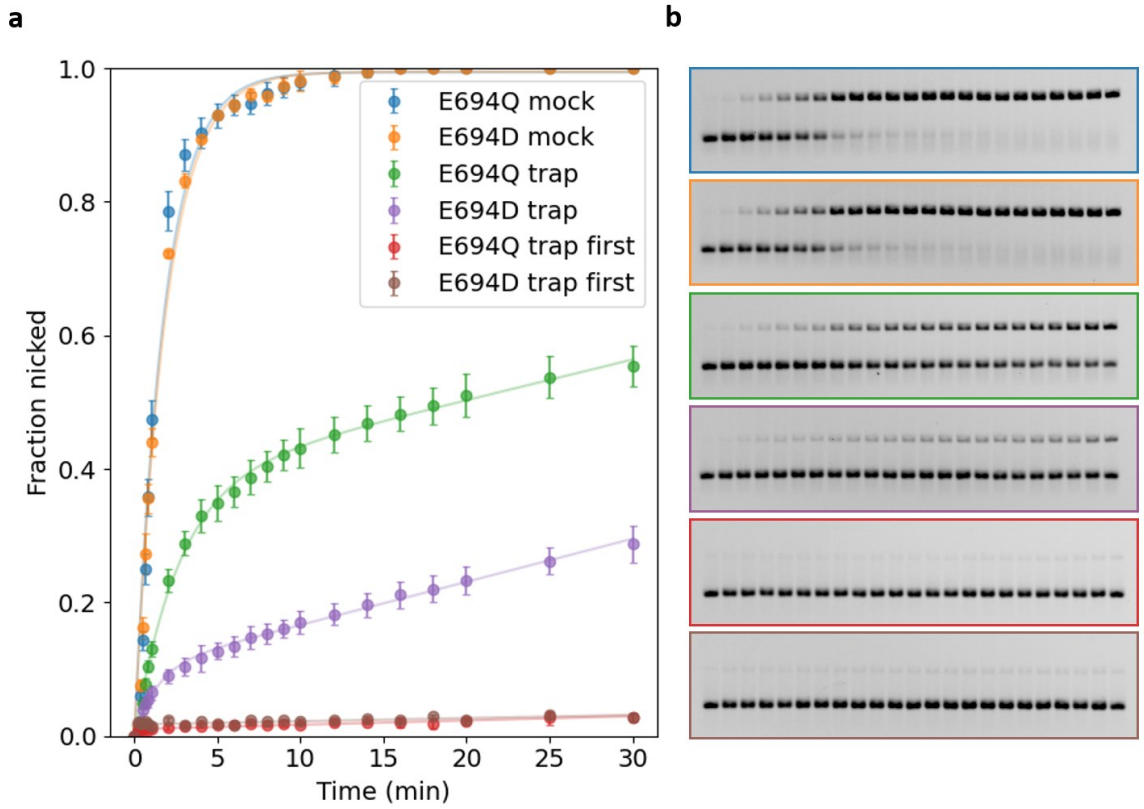

Figure 63. MutH activation by MutS^{E694Q} and MutS^{E694D} preassembled on GT#1^{AF647} in the presence of trap oligonucleotides. ***a****, MutH activation in the presence of MutS^{E694Q} and MutS^{E694D} for positive control reactions containing no trap ("mock", blue and orange, respectively), negative control reactions in which the trap is mixed with GT#1^{AF647} ("trap first", red and brown, respectively) and reactions in which trap is added together with ATP, MutL and MutH ("trap", green and purple, respectively). Fits are shown as solid lines. Data is shown as mean ± std, N=3.* ***b****, Exemplary gel data of corresponding traces.*

As expected, no activation was observed in negative control reactions in which a mixture of GT#1^{AF647} and trap DNA was used during preassembly, showing that the trap successfully sequesters all mutant MutS from solution (**Fig. 63 and Fig. 64**). Additionally, when the competitor oligonucleotides were substituted with an equal volume of buffer all DNA was incised within 30 min when employing MutS^{E694Q} and MutS^{E694D}.

Data obtained in the absence of the trap (mock) was well ($R^2 \geq 0.98$) fitted by exponentials and revealed that in the limit as time tends to infinity reactions containing both MutS^{E694Q} and MutS^{E694D} resulted in complete incision with similar rates of 0.57 ± 0.041 min^{-1} and 0.54 ± 0.022 min^{-1}, respectively.

Under these conditions MutS^{E694N} also resulted in enhanced MutH activation, leading to incision of approximately 80% of all DNA molecules within 3 h, in accordance with previous observations (**see R.3.1.4**). Fitting the data to **Eq. 2** (**see M.7**) showed that under these conditions nearly all DNA (95 ± 1.4%) would be nicked in the limit of time to infinity with a requiring 24 ± 1.3 min to reach half of this fraction.

In the presence of the trap all use of MutS resulted in biphasic activation of MutH (**Fig. 63 and Fig. 64, trap**). Fitting the biphasic activation patterns with a combination of an exponential and a linear function resulted in near perfect fits ($R^2 \geq 0.99$). The fast rates obtained from the exponential phases were determined to be 0.37 ± 0.014 min^{-1}, 0.73 ± 0.09 min^{-1} and 0.28 ± 0.086 min^{-1} and the slow linear rates 0.0061 ± 0.00042 min^{-1}, 0.0064 ± 0.00050 min^{-1} and 0.0013 ± 0.00023 min^{-1} for MutS^{E694Q}, MutS^{E694D} and MutS^{E694N}, respectively. Fitted parameters obtained from fits to "Trap" data are consolidated in **Table 3**.

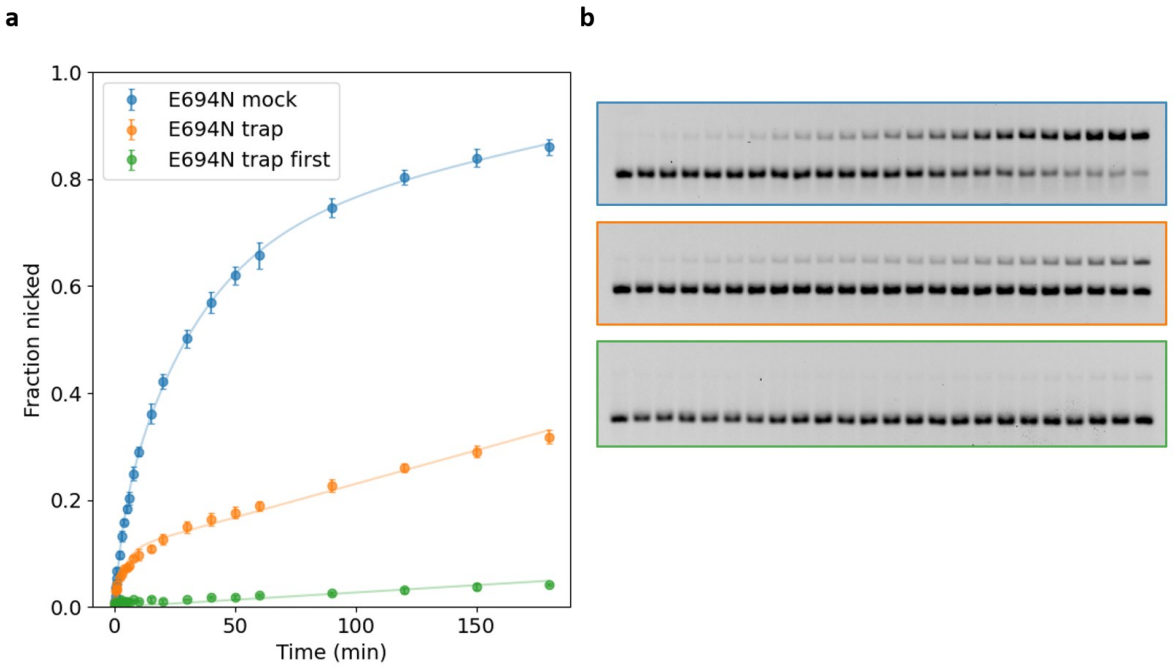

Figure 64. MutH activation by MutS^{E694N} preassembled on GT#1^{AF647} in the presence of trap oligonucleotides. ***a****, MutH activation in the presence of MutS^{E694N} for positive control reactions containing no trap ("mock", blue), negative control reactions in which the trap is mixed with GT#1^{AF647} ("trap first", green) and reactions in which trap is added together with ATP, MutL and MutH ("trap", orange). Fits are shown as solid lines. Data is shown as mean ± std, N=3.* ***b****, Exemplary gel data of corresponding traces.*

MutS	r_1 (min^{-1})	α (%)	r_2 (min^{-1})
Wild type	2.14 ± 0.099	46 ± 1.2	-
E694Q	0.37 ± 0.014	38 ± 2.1	0.0061 ± 0.00042
E694D	0.73 ± 0.09	10 ± 1.1	0.0064 ± 0.00050
E694N	0.28 ± 0.086	10 ± 1.2	0.0013 ± 0.00023

***Table 3**. Kinetic parameters of MutH activation in the presence of trap oligonucleotides for wildtype and mutant MutS. Data is shown as mean ± std, N=3.*

R.5.1.7 Maturation of the MutS^{E694N} sliding clamp results in enhanced MutH activation

Finally, to investigate the earlier observed time dependency of MutH activation by the MutS^{E694N} sliding clamp, the time dependency was studied in the presence of the trap oligonucleotides in order to rule out multiple loading.

Therefore, 100 nM MutS^{E694N} was incubated with 0.5 nM GT#1^{AF647} for 1 min. Subsequently, 1 mM ATP and 1 µM trap was supplemented and the reactions were incubated for various durations ranging from 1 min to 3 h. Thereafter, a mixture of 100 nM MutL and 50 nM MutH was supplemented and MutH activation was followed by intermittently sampling the reactions for 2 min (**Fig. 65**).

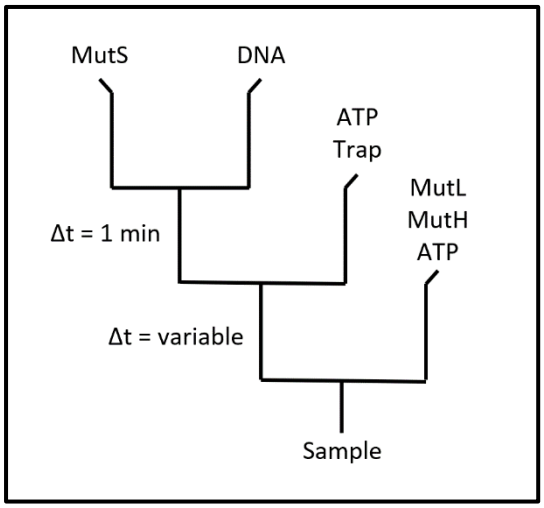

***Figure 65**. Schematic summary of the order of addition.*

As expected, the amplitude of MutH activation monotonically increased with increasing incubation time as evidenced by the increase in plateau height over time (**Fig. 66, see appendix Fig. 73 for gel data**). The maximum amplitude of activation obtainable was ~20%, agreeing well with previous experimental observations obtained under similar conditions (**Fig. 64**). This reduction in maximum obtainable activation amplitude compared to MutH activation observed in the absence of the trap (**Fig. 59**) is likely due to competition by the trap oligonucleotides.

Furthermore, fitting each trace by an exponential function and plotting the plateau value obtained in the limit of time to infinity versus incubation time with the trap and ATP mixture revealed that the extent of MutH activation was exponentially dependent on the incubation time. The data was well fitted by an exponential function (R^2 = 0.986) and yielded a plateau of 22%. By taking the inverse of the mean rate obtained by fitting the exponential, the mean time required to reach half of the maximum MutH activation amplitude was calculated to be 13.9 min.

Moreover, plotting the rates obtained from each exponential fit to the traces (**Fig. 66a**) versus incubation time showed that there was no incubation time dependency on the rates. Furthermore, taking the average of all rates yielded a mean MutH activation rate of 22 s.

Taken together the data clearly shows that the MutS^{E694N} sliding clamps mature in a time dependent fashion prior to addition of MutL and MutH. Moreover, the data show that under these conditions the entire population of sliding clamps has matured after 2.5 h.

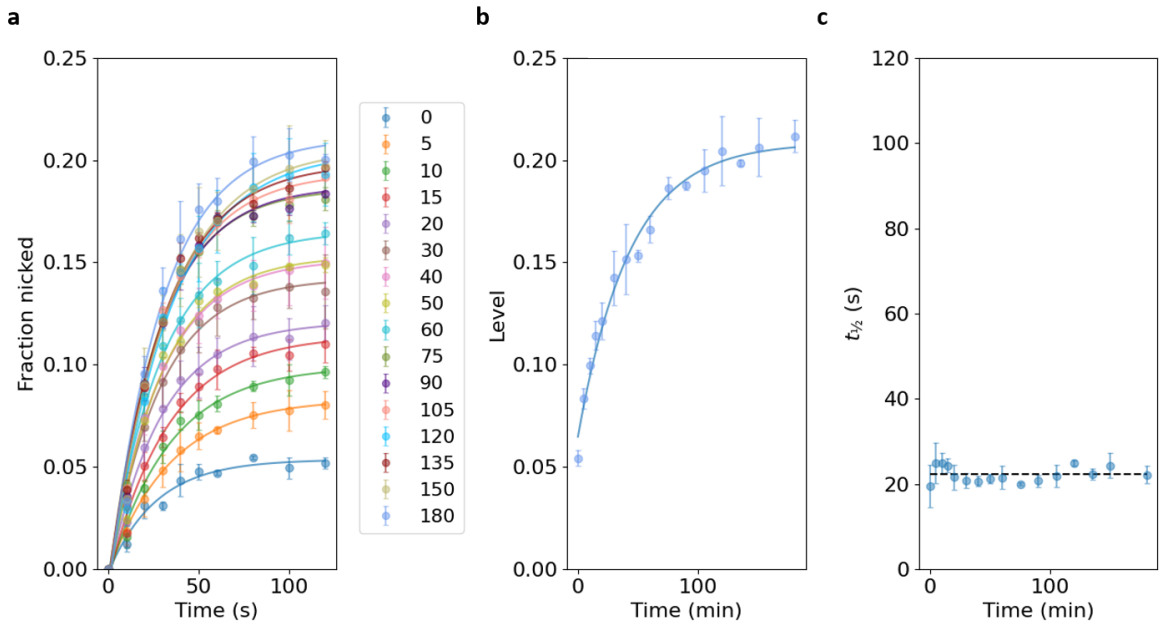

Figure 66. Incubation time of MutS^{E694N} sliding clamps in the presence of trap oligonucleotides correlates with MutH activation amplitude. ***a****, MutH activation monitored for 2 min after various incubation periods with ATP and trap. Colored legend denotes incubation time in min prior to addition of MutL and MutH.* ***b****, Fitted plateau values from* ***a*** *plotted versus incubation time with ATP and trap.* ***c****, Fitted MutH activation rates from* ***a*** *plotted versus incubation time with ATP and trap. Fits are shown as solid lines. Data is shown as mean ± std, N=3.*

R.5.2 Reconstituted in vitro FRET assay to investigate MutH recruitment in real-time

In addition to MutH activation, MutH recruitment was investigated based on a recently developed state-of-the-art real-time FRET assay adapted from Kunetsky et al. (2021)[92]. The assay is based on energy transfer between a DNA intercalator and a fluorescently labelled MutH variant when in close proximity, leading to a FRET signal (**Fig. 67**).

The DNA intercalator utilized during the recruitment assays is SYBR Green I (SG), a cyanine dye that experiences substantial fluorescence enhancement upon binding to duplex DNA[93]. This fluorescence amplification is attributed to SG's aromatic rings, which intercalate into the minor groove of dsDNA. Binding to DNA results in spatial limitations, which restrain the chromophore's internal motion through electrostatic interaction with the DNA backbone. As a consequence, SG adopts a fixed conformational state that enhances the fluorescence signal.

Additionally, Alexa Fluor® 647 fluorophore (AF647) labelled single cysteine MutH variant ($^{MutH156C\text{-}AF647}$) in combination with purified MutS and MutL were employed. Upon MutH recruitment AF647 comes into close proximity to the SG intercalated DNA, allowing for energy transfer from SG (donor), when excited at 485 nm, to AF647 (acceptor). Consequently, AF647 emits a FRET signal at 680 nm, enabling real-time monitoring of MutH recruitment to the DNA. 3196 bp heteroduplex (GT#1) or homoduplex (AT#1) circular DNA constructs containing a hemi-methylated GATC site were constructed as described (**see M.4**) and were used as substrate during the FRET experiments and.

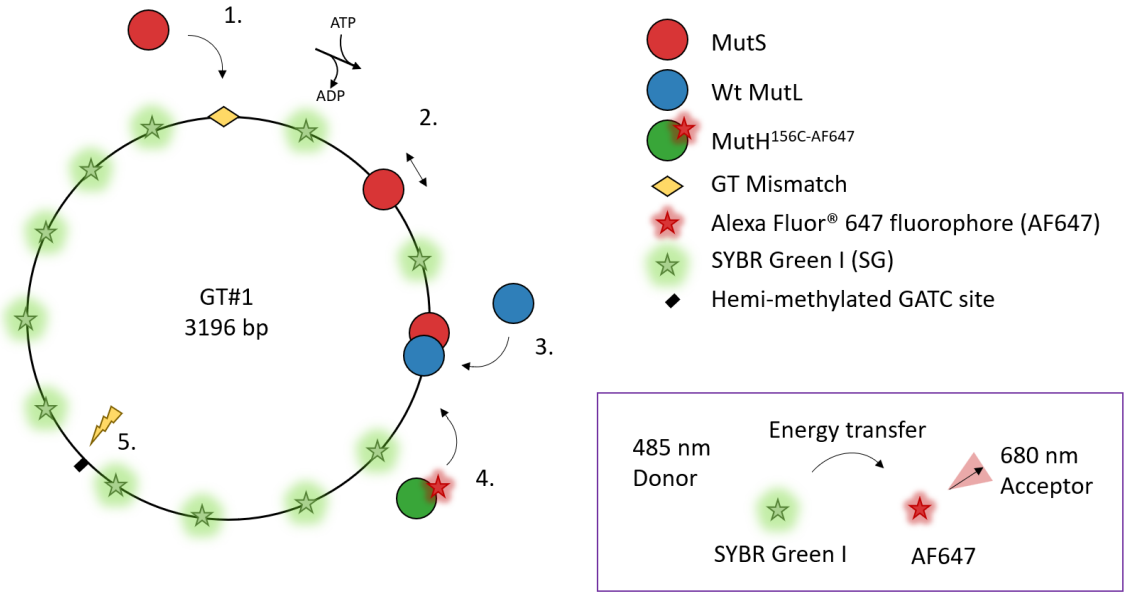

Figure 67. Schematic representation of MutH recruitment assay principle. *Following mismatch binding (**1.**) and sliding clamp formation (**2.**) MutS is able to recruit and activate MutL (**3.**) and subsequently MutH$^{156C\text{-}AF647}$ (**4.**) which results in FRET between the SG and AF647 and ultimately in incision at the hemi-methylated GATC site (**5.**).*

R.5.2.1 Analysis of spectral bleed-through during MutH recruitment assay

To ensure that there was no spectral bleed-through from the donor and the acceptor into the FRET channel, spectral bleed-through coefficients of the donor and acceptor in the donor, acceptor and FRET channels were experimentally determined.

Reactions comprised of 100 nM MutS^{Wt}, 100 nM MutL, 1 mM ATP and 0.5 nM GT#1 were conducted either with or without SG (donor) and with either wildtype MutH (no acceptor) or MutH$^{156C\text{-}AF647}$ (acceptor).

Prior to addition of ATP, fluorescence in the donor and acceptor channels was assessed by exciting the reactions at 485 nm and 620 nm, respectively, and monitoring emission at 535 nm and 680 nm, respectively, for 1 minute at 1 Hz. Additionally, the FRET signal was evaluated by exciting at 485 nm and measuring emission at 680 nm for 10 min at 1 Hz after injecting ATP. The obtained measurements were averaged and are presented as a heatmap in **Figure 68**.

In the absence of the acceptor but presence of the donor (+/-), excitation at 485 nm is expected to lead to emission of only the donor (535 nm). Moreover, in the absence of the donor but presence of the acceptor (-/+), excitation of the acceptor at 620 nm is expected to lead to emission of only the acceptor at 680 nm. In the presence of both donor and acceptor (+/+) signal is expected in all three channels. Finally, in the absence of both the donor and the acceptor (-/-), no signal is expected in any of the channels.

As anticipated, the FRET signal was notably diminished when the donor (+/-), acceptor (-/+), or both (-/-) were absent, in contrast to measurements performed in the presence of both (+/+). These observations suggests that there is negligible spectral bleed-through of the donor and acceptor into

the FRET channel. Indeed, spectral bleed-through coefficients calculated as described[94] from the donor (S1) and acceptor (S2) into the FRET channel were found to be nearly zero. These outcomes demonstrate that the vast majority of the signal detected in the FRET channel was generated by FRET between SG and AF647, in line with expectations.

Moreover, no substantial signal was detected in the donor channel when both the donor and acceptor were absent (-/-) or only the acceptor was present (-/+). However, significant signal was observed in reactions containing the donor (+/- and +/+) with the strongest signal detected in the absence of the acceptor (+/-), indicating that in the presence of the acceptor, energy transfer occurs, resulting in a decline in signal (compare +/+ and +/-), as anticipated.

Additionally, no signal was detected in the acceptor channel in the absence of the acceptor (+/- and -/-). However, significant signal was detected in the presence of the acceptor (-/+ and +/+). Spectral bleed-through coefficients from the donor into the acceptor (S3) and acceptor into the donor (S4) channels were calculated to be nearly zero, indicating that there was negligible bleed-through between all channels. All coefficients as well as excitation and emission wavelengths are summarized in **Table 4**.

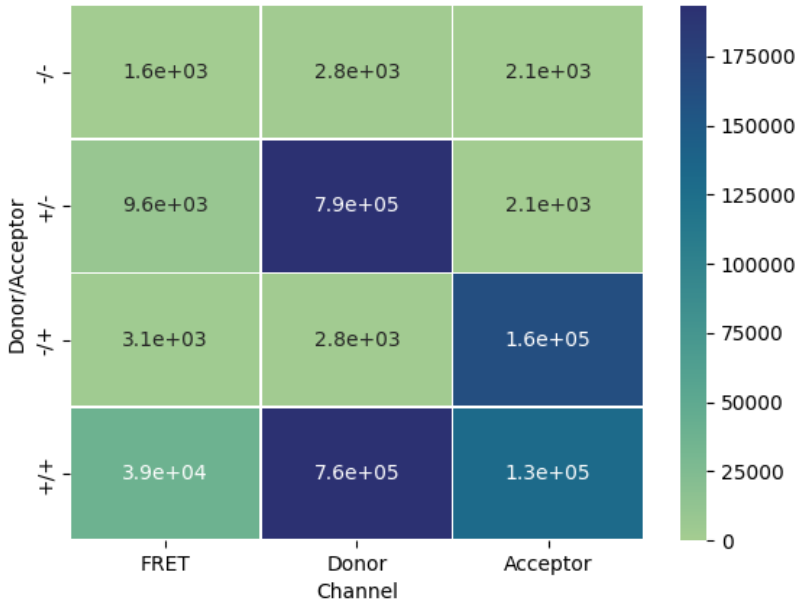

Figure 68. Heatmap of spectral bleed-through measurements. *Averaged fluorescence in FRET, donor and acceptor channels are shown in the presence of only the donor (+/-), acceptor (-/+), both (+/+) or in the absence of both donor and acceptor (-/-).*

				Channel					
				Donor		**Acceptor**		**FRET**	
S_1	**S_2**	**S_3**	**S_4**	**Ex**	**Em**	**Ex**	**Em**	**Ex**	**Em**
0.012	0.019	0.0027	0.018	485	535	620	680	485	680

Table 4. Spectral bleed-through coefficients as well as excitation and emission wavelengths*. Spectral bleed-through coefficients from the donor into the FRET (S_1) or acceptor (S_3) channel, as well as the spectral bleed-through coefficients of the acceptor into the FRET (S_2) or donor (S_4) channel. All*

excitation (Ex) and emission (Em) wavelengths are in nm. Excitation and emission bandwidth are 15 nm and 25 nm, respectively.

R.5.2.2 MutH recruitment by preassembled MutS-DNA complexes correlates with ATPase activity.

After establishing that there was no significant spectral bleed-through from the donor and acceptor into the FRET channel, MutH recruitment was investigated in real-time using wildtype or mutant MutS preassembled onto GT#1. In addition, samples from each reaction were analyzed by gel-electropheresis in order to investigate MutH activation, allowing for simultaneous monitoring of recruitment and activation in a single experimental setup.

To achieve this, reactions containing 100 nM of either wildtype or mutant MutS, 100 nM MutL, 200 nM SG and 50 nM $MutH^{156C\text{-}AF647}$ were incubated with 0.5 nM GT#1 for 5 min (**see M.8.1**). Subsequently, the reactions were initiated by injecting 1 mM ATP (**Fig. 69a**). Following addition of ATP, fluorescence was measured by exciting the reactions at 485 nm and measuring emission at 680 nm for 10 min at 1 Hz. Afterwards 10 µl samples were taken and aliquoted in an equal volume of stop solution (**see M.8.1**). The samples were then analysed by gel-electrophoresis in order to study MutH activation in addition to recruitment. Following gel-electrophoresis the DNA was stained with SYBR gold, a cyanine dye DNA intercalator that exhibits >1000-fold fluorescence enhancement upon DNA binding, to visualize the DNA (**see M.8.2**).

FRET signals were normalized with respect to the fluorescence of the $MutS^{Wt}$ reaction at 10 min, after background subtraction. As anticipated, the MutS mutants led to varying degrees of $MutH^{156C\text{-}AF647}$ recruitment (**Fig. 69b**). $MutH^{156C\text{-}AF647}$ was recruited most rapidly in the presence of $MutS^{Wt}$, while $MutS^{E694Q}$ and $MutS^{E694D}$ exhibited similar levels of recruitment, with $MutS^{E694Q}$ exhibiting slightly higher recruitment. Moreover, $MutS^{E694N}$ resulted in a very low FRET signal, indicative of almost no recruitment. Additionally, the SYBR Gold-stained gel exhibited a similar trend (**Fig. 69c**). However, the gel data indicates that after 10 min nearly all DNA molecules were incised in reactions containing $MutS^{Wt}$, $MutS^{E694Q}$ or $MutS^{E694D}$ emphasizing the disparity between MutH recruitment and activation. Despite almost all DNA being incised under these circumstances, MutH recruitment had not yet reached steady state.

Furthermore, only a slight increase in FRET signal was observed when substituting GT#1 for AT#1 (homoduplex control), indicating that the observed activity was mismatch specific. Additionally, no recruitment was observed when MutS, MutL or ATP was substituted with an equal volume of buffer, showing all activity was pathway specific. In accordance with the absence of a FRET signal, no significant fraction of DNA was incised in any of the controls, indicating MutH was not recruited or activated.

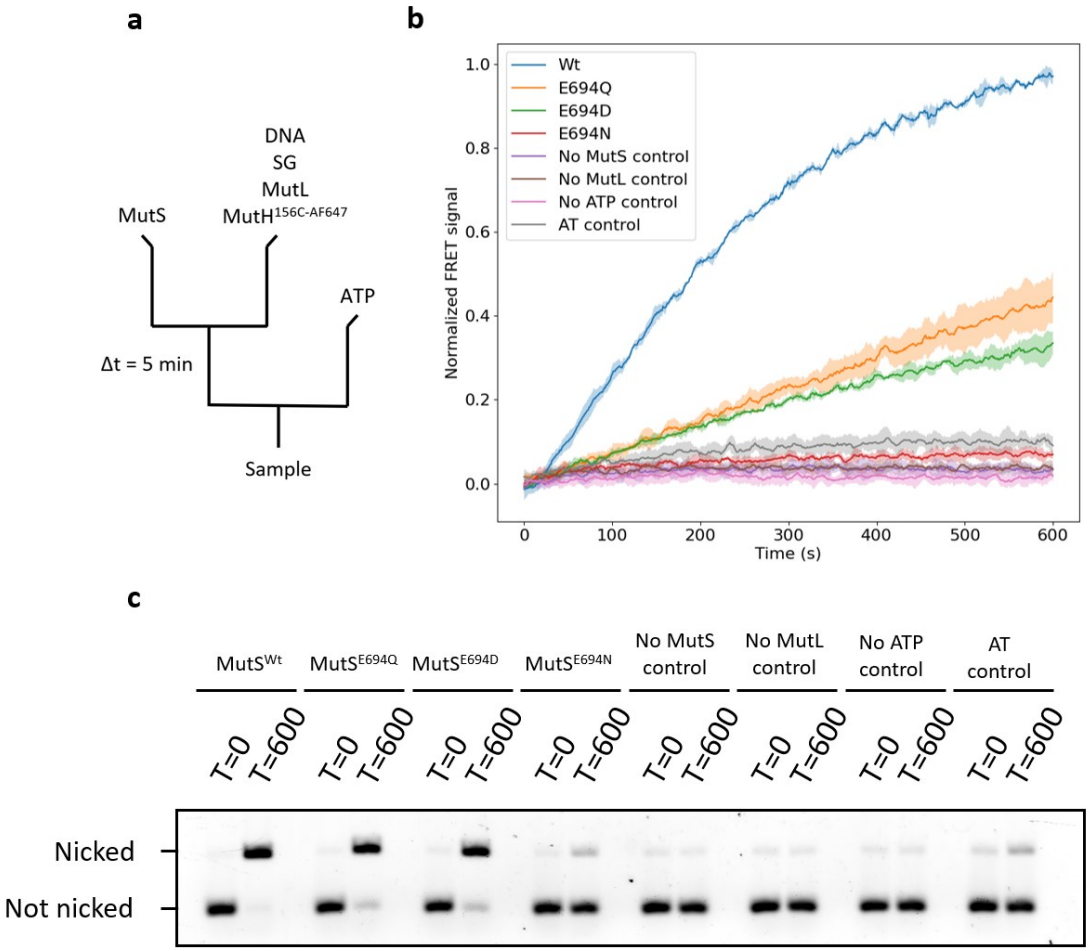

***Figure 69. MutH$^{156C\text{-}AF647}$ recruitment by preassembled MutS-DNA complexes. a**, Schematic summary of the order of addition. **b**, Normalized FRET signal obtained in the presence of MutS^{Wt} (blue), MutS^{E694Q} (orange), MutS^{E694D} (green) and MutS^{E694N} (red) as well as control reactions in which MutS (purple), MutL (brown) or ATP (pink) was substituted with buffer or in which heteroduplex DNA was substituted with homoduplex DNA (grey). Data is represented as mean (solid lines) ± std (shaded regions), N=3. **c**, SYBR Gold stained gel showing MutH activation at zero time (T=0) and after 10 min (T=600) for corresponding traces in **b**.*

Taken together the data show that MutH is being recruited to the DNA in a pathway specific manner by the combined action of MutS and MutL, where upon activation MutH leads to incision. Moreover, this data agrees well with the observation that preassembly of MutS on DNA leads to enhanced MutH activation, as described in **section R.5.1.3**. We propose that upon dimerization of the N-terminal MutL domains a high affinity MutH binding site is created which enables MutH recruitment to the DNA, in accordance with our data.

R.5.2.3 Nucleotide-bound MutS results in significantly reduced MutH recruitment compared to DNA-bound MutS

Next, MutH recruitment by nucleotide bound MutS was investigated. Based on MutH activation observations as described earlier (**see R.3.1.1**) MutH recruitment was expected to be reduced compared to recruitment by preassembled MutS-DNA complexes.

Reactions containing 100 nM of either wildtype or mutant MutS, 100 nM MutL, 1 mM ATP and 50 nM $MutH^{156C\text{-}AF647}$ were incubated for 5 min. Subsequently, the reactions were initiated by injecting a solution containing 200 nM SG and 0.5 nM GT#1 (**Fig. 70a**). Following addition of the SG intercalated DNA, fluorescence was measured by exciting the reactions at 485 nm and measuring emission at 680 nm for 10 min at 1 Hz. Afterwards 10 µl samples were taken and aliquoted in an equal volume of stop solution (**see M.8.2**). The samples were then analysed by gel-electrophoresis as described in the previous section (**see R.3.2.2**).

FRET signals were normalized with respect to fluorescence corresponding to steady-state MutH recruitment in the presence of $MutS^{Wt}$ after background subtraction. Under these conditions the normalized FRET signals for the mutants were significantly lower compared to experiments in which MutS was preassembled on the DNA. Furthermore, recruitment correlated with ATPase activity. These findings agree well with data described in **section R.3.1.1**, supporting the hypothesis that MutS is in a closed ATP-bound state prior to addition of DNA and that ATP hydrolysis enables conformational transition to an open conformation, enabling mismatch binding and subsequently pathway activation.

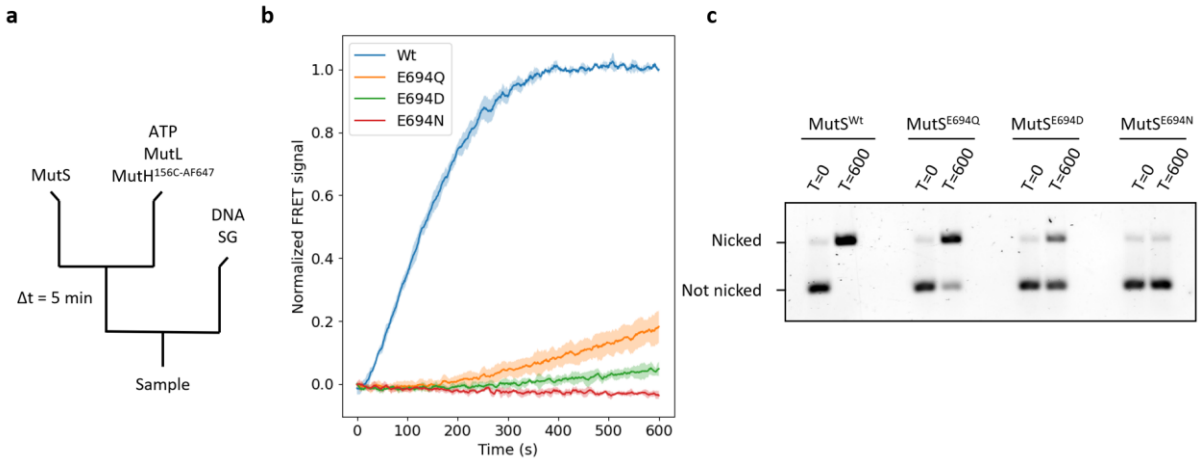

***Figure 70. MutH$^{156C\text{-}AF647}$ recruitment by nucleotide-bound MutS. a**, Schematic summary of the order of addition. **b**, Normalized FRET signal obtained in the presence of $MutS^{Wt}$ (blue), $MutS^{E694Q}$ (orange), $MutS^{E694D}$ (green) and $MutS^{E694N}$ (red). Data is represented as mean (solid lines) ± std (shaded regions), N=3. **c**, SYBR Gold stained gel showing MutH activation at zero time (T=0) and after 10 min (T=600) for corresponding traces in **b**.*

Moreover, the gel data indicates that after 10 min all DNA molecules were incised in reactions containing $MutS^{Wt}$. The amplitude of MutH activation was lower for $MutS^{E694Q}$, even lower in the presence of $MutS^{E694D}$ and absent in the presence of $MutS^{E694N}$, in agreement with earlier observations.

Collectively the data indicate that prebinding of the MutS mutants to ATP leads to a reduction in MutH recruitment compared to preassembled MutS-DNA complexes and that this correlates with ATPase activity indicating that MutH recruitment by preassembled MutS-DNA complexes dependent upon ATP hydrolysis.

Conclusions, discussion & future prospects

This section summarises the conclusions obtained from this study and discusses the results by placing these into the context of the literature. Additionally, ideas for future investigations are proposed and discussed. The most noteworthy kinetic parameters obtained from this study are summarised in **Table 5**.

	ATPase actvity		*Nucleotide exchange*, k_{off}^{ADP} (s^{-1})			*SPR*	*MutH activation*		
MutS	V_{max} (min^{-1})	K_m (μM)	**No DNA**	**Homoduplex DNA (AT)**	**Mismatched DNA (GT)**	$K_{\frac{1}{2}}^{ATP}$ (μM)	r_1 (min^{-1})	α (%)	r_2 (min^{-1})
Wild type	1.8 ± 0.42	43 ± 8.3	0.009 ± 0.001	0.046 ± 0.001	0.22 ± 0.02	46 ± 4.7	2.14 ± 0.099	46 ± 1.2	-
E694Q	0.19 ± 0.017	33 ± 8.3	-	0.0022 ± 0.001	0.082 ± 0.02	15 ± 2.0	0.37 ± 0.014	38 ± 2.1	0.0061 ± 0.00042
E694D	0.052 ± 0.0074	4.1	0.001 ± 0.001	0.0093 ± 0.001	0.062 ± 0.006	20 ± 3.9	0.73 ± 0.09	10 ± 1.1	0.0064 ± 0.00050
E694N	0.012 ± 0.0012	< 20	-	0.0064 ± 0.0005	0.034 ± 0.02	16 ± 3.8	0.28 ± 0.086	10 ± 1.2	0.0013 ± 0.00023

Table 5. *Summary of the kinetic parameters. Data is shown as mean ± std, N≥3.*

C.1 The implication of E694 in ATP binding and hydrolysis in MutS

To conclude, constructs coding for MutS^{E694Q} and MutS^{E694D} were generated, sequence verified and subsequently utilized in combination with constructs coding for MutS^{Wt} to successfully purify MutS^{Wt}, MutS^{E694Q} and MutS^{E694D}. Subsequently, a colorimetric ATPase assay was successfully implemented, optimized and utilized to determine the ATPase activity of wildtype and mutant MutS. The kinetic parameters for MutS^{Wt} and MutS^{E694Q} agree well with literature[21,22,44,56,57,59]. Moreover, the data revealed that the mutants are impaired in ATP hydrolysis (reduced V_{max}, **Table 5**) but with apparent enhanced ATP binding (reduced K_m, **Table 5**). Specifically, MutS^{E694Q}, MutS^{E694D} and MutS^{E694N} exhibit reductions in maximum steady-state ATP hydrolysis velocities compared to the wildtype of approximately 10, 35 and 150-fold, respectively.

These observations support previous findings stating that the E694 residue is imperative to ATPase activity of MutS. Particularly, this indicates the critical role of the negative charge on the glutamic acid residue. This residue is thought to participate in destabilisation of the β-γ phosphate bond of ATP, resulting in an elevated energetic state of the enzyme-substrate complex such that the energy barrier of the transition state is overcome more easily. However, we deem it unlikely that E694 acts as the catalytic base during ATP hydrolysis, since the difference between the carboxyl group of this moiety and the γ-phosphate of ATP is 3.2 Å which disqualifies it as bonafide catalytic base. Lamers et al. (2000) speculate that H728 may act as catalytic base, although the χ_1 dihedral angle of H728 in their structure is in a suboptimal orientation for the residue to act as catalytic base[68]. However, H728 is ideally positioned (with a distance of 2.8 Å) in structures of ATP or AMPPNP-bound MutS[15,56]. In support of this hypothesis, the equivalent of H728 in Rad50 (also an ABC ATPase) is thought to activate a water molecule to perform nucleophilic attack on the γ-phosphate of ATP and this finding was corroborated by recent quantum mechanical modelling of the ABC transporter HlyB[71,72]. Taken together the data therefore indicate that E694 destabilizes the β-γ bond such that a water molecule activated by H728 can perform nucleophilic attack, ultimately resulting in ATP hydrolysis.

Furthermore, since the aspartic acid residue introduced in MutS^{E694D} is one CH_2 group shorter than the glutamine residue found in MutS^{E694Q}, the data suggest that the sidechain length of E694 is more important for enzymatic activity than the charge of the carboxyl group. That both the sidechain length and charge are imperative for enzymatic activity is further supported by removal of both the negative

charge and a CH_2 group (E694N) which results in the most extreme reduction in activity. Further shortening the length of the sidechain does not lead to an additional decrease in activity as shown by the activity of the E694A mutant (V_{max} = 0.02 min^{-1}), extensively studied in literature[12,21,70]. Any residual ATPase activity from the E694N mutant is therefore likely a holistic effect of the active site rather than originating from the residue at position 694.

Additionally, the K_m values for ATP indicate that the affinity for ATP by all MutS mutants is enhanced compared to that of the wildtype, presumably due to decreased electrostatic repulsion of the γ-phosphate of ATP. In support of this hypothesis, affinity for ATP has also been observed to be enhanced for the E694A mutant[70]. These findings were further supported by SPR data, showing that compared to the wildtype the MutS mutants were more sensitive to changes in ATP concentration, leading to enhanced ATP induced dissociation by preassembled MutS-DNA complexes (reduced $K_{\frac{1}{2}}^{ATP}$, **Table 5**). The ATP induced dissociation likely reflects the formation of sliding clamps which subsequently diffuse off the free end of the DNA, in accordance with data obtained using the eukaryotic ortholog of MutS (MutSα) by Mazur et al. (2006) and observations by Lebbink et al. (2010)[56,62].

Moreover, data obtained by Mazur et al. (2006) suggest that sliding clamps are only formed when ATP is bound by both subunits, indicating that the ATP induced release off the free end of the DNA reflects binding to the low affinity nucleotide binding site in MutS. Therefore, the $K_{\frac{1}{2}}^{ATP}$ values as determined by SPR spectroscopy (**Table 5**) reflect ATP affinity of the low affinity binding site in MutS. Additionally, observations by Fernandez-Leiro et al. (2021) showed that on end-blocked DNA higher concentrations of ATP lead to an enhanced binding response for wildtype MutS, indicating that sliding clamps are formed more readily at higher concentrations of ATP, leading to faster vacancy of the mismatch enabling multiple sliding clamps to be loaded[11].

Furthermore, the affinity for ATP of $MutS^{E694D}$ and $MutS^{E694N}$ is more affected than that of $MutS^{E694Q}$, indicating that the sidechain length of E694 is more important for ATP binding than the negatively charged carboxyl group. However, it should be noted that these observations are in contrast to published findings indicating that removal of the carboxylate of Glu in the Walker B motif usually reduces Mg^{2+} binding and hence ATP affinity in ATPases, see Junop et al. (2001)[21,95].

Unfortunately, it was not possible to study multiple turnover kinetics by $MutS^{E694N}$ for concentrations below 20 µM ATP using the current assay, due to the relatively high ATP affinity and heavily impaired steady-state hydrolysis velocity of the protein. Recently, however, Gaché et al (2020) showed that the stability and sensitivity of colorimetric ATPase assay reagents is enhanced by the addition of perchloric acid and Pluronic F68, lowering the detection limit to 0.22 µM, enabling more sensitive and reliable determination of kinetic parameters[85]. Therefore further optimizing the colorimetric ATPase assay would be an interesting next step for future research into the implications of the active site mutations presented here. However, it should be noted that proper safety measures have to be taken since perchloric acid is highly corrosive and flammable.

Additionally, investigating ATPase activity of MutS on DNA would be interesting as DNA is expected to alter the activity. This can be achieved using a fluorescent ATPase assay which enables monitoring of pre-steady-state ATP hydrolysis using a phosphate binding protein which enters into an enhanced fluorescent state upon phosphate binding[20,61]. The advantage of this method is that ATPase activity of MutS on DNA can be studied in a sensitive manner using a stopped flow fluorimeter.

C.2 The role of the negatively charged carboxyl of E694 in ADP and DNA binding in MutS

The findings obtained from nucleotide exchange experiments (**Table 5**) agree well with the hypothesis that the negatively charged carboxyl group of E694 is imperative for nucleotide release in the absence of DNA by electrostatic repulsion of the negatively charged β-phosphate of ADP. Only in $MutS^{Wt}$ and $MutS^{E694D}$ does the amino acid on position 694 contain a negatively charged carboxyl group, whereas this group is not present in $MutS^{E694Q}$ and $MutS^{E694N}$. Moreover, this would explain the reduced exchange rate observed for $MutS^{E694D}$, since its sidechain is one CH_2 group shorter compared to the wildtype, leading to reduced charge repulsion between the carboxyl group and the phosphate tail, resulting in a reduced Mant-ADP release rate. However, it should be noted that other residues in the active site also participate in nucleotide binding and that a shift in local electrostatics may change the ability of other residues to participate in nucleotide binding and hydrolysis. Therefore, it would be interesting to obtain structures (Cryo-EM or X-ray) of the active site mutants to investigate whether the observed differences are direct or indirect effects of the active site mutations.

Furthermore, since ADP release is an integral step of the ATP hydrolysis cycle, the extremely low ADP release rate observed for $MutS^{E694Q}$ and $MutS^{E694N}$ in the absence of DNA may explain, at least partially, the reduced steady-state hydrolysis velocity as determined using the colorimetric ATPase assay. Therefore the data indicates that besides lowering the energetic barrier of the transition state, E694 also enhances steady-state ATP hydrolysis by facilitating ADP release. Literature on ADP-release by $MutS^{Wt}$ indicates that during steady-state ATP hydrolysis ADP release is rate limiting in accordance with the data presented here[56]. Moreover, under these conditions where the ratio MutS monomer: Mant-ADP is approximately 2:1, Mant-ADP is expected to bind only to the high affinity nucleotide binding site in MutS, indicating that release kinetics represent release by the high affinity site.

Additionally, the data show that DNA stimulates nucleotide exchange for both wildtype and mutant MutS and that this stimulatory effect is enhanced for heteroduplex compared to homoduplex DNA, in accordance with published findings[44,56,59]. End-blocking the free ends of the oligonucleotides did not alter the release kinetics in contrast to observations by Acharya et al. (2003). We therefore propose that the reduced ADP release rate observed in the presence of homoduplex DNA reflects specific effects of the DNA mismatch and/or the reduced affinity for homoduplex DNA by MutS, resulting in a larger fraction of unbound MutS in which ADP release is not stimulated by the DNA[59]. This hypothesis is supported by SPR data indicating that for both wildtype and mutant MutS binding to heteroduplex DNA was significantly higher than binding to homoduplex DNA.

Moreover, SPR spectroscopy revealed that the amino acid residue at position 694 plays a pivotal role in mismatch binding, emphasizing the communication between the C-terminal ATPase and N-terminal mismatch binding domains and demonstrating the implication of this residue in the mode of communication between these distal domains. Specifically, the negative charge of this residue appears to be essential for effective communication, as mismatch binding of $MutS^{E694D}$ is only slightly reduced compared to that of the wildtype, whereas the affinities of both $MutS^{E694Q}$ and $MutS^{E694N}$ are greatly diminished (reduced $k_{a,app}$, **Table 5**). Moreover, both wildtype and mutant MutS displayed enhanced binding to heteroduplex compared to homoduplex DNA, indicating that the active site mutations did not markedly alter the discriminatory capacity against homoduplex DNA, however small but consistent changes in discriminatory capacity were observed.

Whether the reduced binding response is a direct effect of the ATPase active site mutations on DNA binding, or an indirect effect of the mutations on nucleotide binding that in turn modulates DNA binding, remains to be investigated. It has been shown that $MutS^{Wt}$ is purified with nucleotide bound which is also expected for the active site mutants due to enhanced affinity for nucleotide[12,38]. This may

also explain the production of phosphate by MutS^{E694N} in the absence of externally supplied ATP, as measured by the colorimetric ATPase assay. For future investigations it may therefore be interesting to investigate the nucleotide content of the MutS mutants which can be achieved by various experimental approaches as described[12,38].

Furthermore, as a next step, monitoring ATP binding instead of ADP release could aid in understanding the role of E694 in nucleotide exchange. This could be achieved using a fluorescent analogue of ATP, Mant-ATP. The expectation is that upon injection Mant-ATP binds to MutS, resulting in spatial confinement of the chromophore, leading to an increase in fluorescence. The rate of increase is expected to be enhanced by DNA, particularly heteroduplex DNA such that an inverse trend is observed compared to the Mant-ADP release data presented here. We conducted an initial experiment using MutS^{E694N} and the results indicate that this approach is promising (**Fig. 71**), however the assay needs to be optimized.

Moreover, more sensitive equipment such as a stopped flow fluorimeter would enable a significant reduction of the time between injection and start of the measurements, leading to more reliable data, which is especially interesting for fast release kinetics as observed in the presence of DNA.

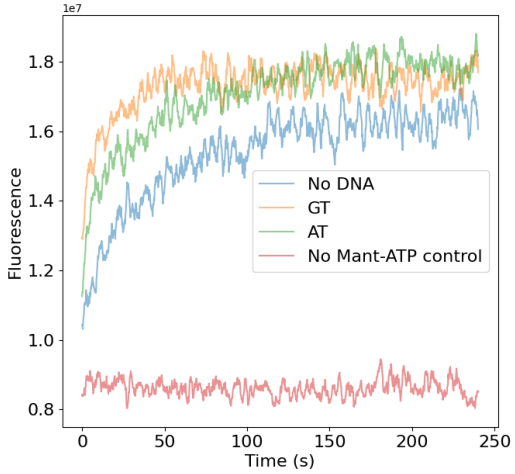

***Figure 71**. Explorative experiment showing Mant-ATP binding by MutS^{E694N} in the absence (blue) or presence of either homoduplex (green) or heteroduplex (orange) DNA. In the absence of Mant-ATP no signal was observed (red).*

C.3 The role of ATP hydrolysis in MutS in its pre- and post-mismatch recognition states

In addition to data obtained by SPR spectroscopy, findings on MutH recruitment and activation clearly show that prebinding of ATP to MutS results in reduced DNA binding, MutH recruitment and pathway activation, in a fashion correlating with ATPase activity. In these experiments MutS is in constant exposure to ATP while scanning the DNA for a mismatch which is similar to *in vivo* circumstances where mismatches may arise during DNA replication. These findings indicate that under these conditions, ATP hydrolysis by the MutS mutants seems to be the rate limiting step in pathway activation. These observations likely reflect closure of MutS upon nucleotide binding, resulting in a conformational state with decreased affinity for DNA which reverts upon ATP hydrolysis, as supported by recent Cryo-EM structures of nucleotide bound MutS[15]. Furthermore, these findings are in accordance with published observations showing that ATP induces a low affinity DNA binding conformation in MutS^{E694A}, which is also impaired in ATPase activity[70]. Moreover, Baitinger et al. (2003) showed that in the absence of Mg^{2+}, DNA binding by MutS^{Wt} and MutS^{E694A} mixed with 1 mM ATP is impaired compared to identical conditions in the presence of Mg^{2+} [12]. This likely reflects reduced ATPase activity due to the absence of Mg^{2+}, in agreement with the hypothesis that ATP hydrolysis is required to revert to an open conformation with enhanced affinity for DNA.

Therefore it is expected that any of the introduced active site mutations leads to severely impaired MMR initiation *in vivo,* resulting in a mutator phenotype. *In vivo* complementation assays conducted with MutS^{E694Q} and MutS^{E694A} show that this is indeed the case[21,22]. Moreover, since the MutS^{E694Q} mutant is least affected in ATPase activity, it is expected that MutS^{E694D} and MutS^{E694N} will also lead to a mutator phenotype *in vivo*.

Preassembly of MutS to the DNA was shown to enhance MutH recruitment as well as activation. Moreover, MutH activation by preassembled MutS-DNA complexes correlates with ATPase activity and was shown to be dependent upon incubation time prior to addition of MutL and MutH. Although preincubation led to enhanced MutH activation for MutS^{E694N}, the rate of activation was shown to be independent of the incubation time prior to addition of MutL and MutH. These findings indicate that communication between mismatch recognition and DNA incision may be dependent upon ATP hydrolysis by the MutS sliding clamp.

In contrast to current dogma in the field, which states that ATP hydrolysis by MutS is only required for dissociation from the DNA, Hao et al. (2020) recently showed that the MutS sliding clamp is continuously hydrolysing ATP, enabling recurrent mismatch binding, which is thought to keep MutS in the vicinity of the mismatch as well as to reset MutS into a mismatch binding competent state[20]. To further narrow down on the actual mode of communication it would be worthwhile to investigate whether dimerization of the N-terminal MutL domains (LN40) also correlates with ATPase activity of MutS or whether MutS-MutL complex dissociation is dependent on ATP hydrolysis by MutS.

Recently, the Friedhoff laboratory (Gießen, Germany) has generated fluorescently labelled MutL mutants which upon dimerization of the N-terminal ATPase domains (closure), result in FRET (personal communication). Investigation of MutL closure in an *in vitro* reconstituted reaction in combination with the MutS mutants presented here may reveal whether ATP hydrolysis by the MutS sliding clamp is required for MutL closure, further narrowing down the seeming dependency on ATP hydrolysis by MutS during MMR initiation. Additionally, MutS-MutL dissociation could be investigated by FRET using fluorescently labelled MutS and MutL mutants as described in Winkler et al. (2011)[96].

The use of trap oligonucleotides allowed for the investigation of single-turnover kinetics by preventing multiple loading and repeated attempts to form sliding clamps. However, this approach also caused a significant decrease in maximum MutH activation, both for wildtype and mutant MutS. Under single-turnover conditions, the degree of MutH activation remained reliant on the pre-incubation time prior to addition of MutL and MutH. We propose that the decrease in maximum obtainable MutH activation amplitude as observed in the presence of competitor oligonucleotides and MutS^{E694N} is due to competition with the fluorescent DNA constructs (GT#1^{AF647}). It is likely that due to severely impaired ATPase activity MutS^{E694N} is unable bind a vacated mismatch site after addition of ATP, hence the observed decrease in the presence of the trap is not due to inability to load multiple sliding clamps but competition by the trap. That the trap competes with the circular DNA constructs is further supported by data from Fernandez-Leiro et al. (2021) who recently showed that crosslinking the MutS sliding clamp rescued MutH activation in the presence of end-blocked competitor oligonucleotides[11]. Therefore, it would be interesting to generate a MutS^{E694N} variant which can be crosslinked in a similar manner as described by Fernandez-Leiro et al. (2021) in order to rescue MutH activation such that activation in the presence of MutS^{E694N} can be compared more readily to activation observed in the presence of wildtype MutS.

Furthermore, MutH activation under single-turnover conditions revealed biphasic activation kinetics for all MutS mutants. The data indicates that for all mutants there appear to be three distinct populations of DNA molecules; One fraction which is incised rapidly, another which is incised slowly

and one which is not incised at all. The population which is not incised represents DNA molecules that were not bound by MutS during pre-incubation or failed to retain sliding clamps after addition of ATP in the presence of the trap. The rapid phase may contradict the hypothesis that the mode of communication between mismatch recognition and DNA incision is reliant on ATP hydrolysis by the MutS sliding clamp, since already within the first minute relatively high amplitudes of MutH activation are observed for all mutants. The population which is rapidly incised may represent DNA on which MutS, MutL and MutH are properly loaded with MutH on the unmethylated strand. Since the rate of activation does not correlate with ATPase activity and is rapid the data indicates that for this population ATP hydrolysis is not required to lead to incision.

However, slow incision was only observed in the presence of the mutants and may therefore indicate that it is reliant on ATP hydrolysis. However, rates obtained in the presence of $MutS^{E694Q}$ and $Muts^{E694D}$ were similar. We speculate that the slow phase could represent MutS, MutS-MutL or even MutS-MutL-MutH complexes which are loaded in a suboptimal conformation, leading to impaired pathway activation. These complexes may require a rearrangement or exchange of components that could be dependent on ATP hydrolysis. For example, it could be that MutH has to be released by MutL and subsequently reloaded at another site in order to lead to incision. Additionally, it could be that MutL has to be released by MutS and needs to be reloaded at the other binding site on MutS. Another option would be that MutS is loaded in a suboptimal conformation where the Phe36 is stacking on the Guanine residue instead of the Thymidine of the mismatch. Alternatively, a subpopulation of the preassembled MutS complexes may form tetramers with MutS complexes on different DNA constructs. These super complexes may well be impaired in pathway activation, resulting in a slow phase, as described[90].

Finally, investigating the effect of different ATP analogues such as ATPyS or AMPPNP on activation by preassembled MutS-DNA complexes could further aid in understanding whether the mode of communication between mismatch recognition and MutH activation is dependent on ATP hydrolysis in MutS. If MutH activation under single-turnover conditions by preassembled $MutS^{Wt}$-DNA complexes is dependent upon incubation time by $MutS^{Wt}$ sliding clamps formed using a slowly hydrolysable ATP analogue prior to addition of MutL and MutH, this would support the hypothesis that ATP hydrolysis by the MutS sliding clamp is required for downstream MMR activation.

References

1. Modrich, P. Strand-specific mismatch repair in mammalian cells. *J. Biol. Chem.* **272**, 24727–24730 (1997).

2. Kunkel, T. A. & Erie, D. A. DNA mismatch repair. *Annu. Rev. Biochem.* **74**, 681–710 (2005).

3. Fishel, R. Mismatch repair. *J. Biol. Chem.* **290**, 26395–26403 (2015).

4. Wimmer, K. & Etzler, J. Constitutional mismatch repair-deficiency syndrome: Have we so far seen only the tip of an iceberg? *Hum. Genet.* **124**, 105–122 (2008).

5. Jiricny, J. The multifaceted mismatch-repair system. *Nat. Rev. Mol. Cell Biol.* **7**, 335–346 (2006).

6. Iyer, R. R., Pluciennik, A., Burdett, V. & Modrich, P. L. DNA Mismatch Repair : Functions and Mechanisms. *Chem. Rev.* **106**, 302–323 (2006).

7. Ponti, G., Castellsagué, E., Ruini, C., Percesepe, A. & Tomasi, A. Mismatch repair genes founder mutations and cancer susceptibility in Lynch syndrome. *Clin. Genet.* **87**, 507–516 (2015).

8. Lynch, H. T. & de la Chapelle, A. Hereditary Colorectal Cancer. *N. Engl. J. Med.* **348**, 919–932 (2003).

9. Henry T. Lynch Trudy G. Shaw, C. D. H. and M. P. H. Milestones in Lynch: 1985-2015. *Nat. Rev.* **15**, 181–194 (2015).

10. Jensen, U. B. *et al.* Mismatch repair defective breast cancer in the hereditary nonpolyposis colorectal cancer syndrome. *Breast Cancer Res. Treat.* **120**, 777–782 (2010).

11. Fernandez-Leiro, R. *et al.* The selection process of licensing a DNA mismatch for repair. *Nat. Struct. Mol. Biol.* **28**, 373–381 (2021).

12. Baitinger, C., Burdett, V. & Modrich, P. Hydrolytically deficient MutS E694A is defective in the MutL-dependent activation of MutH and in the mismatch-dependent assembly of the MutS.MutL.heteroduplex complex. *J. Biol. Chem.* **278**, 49505–49511 (2003).

13. Groothuizen, F. S. *et al.* MutS/MutL crystal structure reveals that the MutS sliding clamp loads MutL onto DNA. *Elife* **4**, 1–24 (2015).

14. Kolodner, R. D., Mendillo, M. L. & Putnam, C. D. Coupling distant sites in DNA during DNA mismatch repair. *Proc. Natl. Acad. Sci. U. S. A.* **104**, 12953–12954 (2007).

15. Borsellini, A., Kunetsky, V., Friedhoff, P. & Lamers, M. H. Cryogenic electron microscopy structures reveal how ATP and DNA binding in MutS coordinates sequential steps of DNA mismatch repair. *Nat. Struct. Mol. Biol.* **29**, 59–66 (2022).

16. Jeong, C. *et al.* MutS switches between two fundamentally distinct clamps during mismatch repair. *Nat. Struct. Mol. Biol.* **18**, 379–385 (2011).

17. Blackwell, L. J., Martik, D., Bjornson, K. P., Bjornson, E. S. & Modrich, P. Nucleotide-promoted release of hMutSα from heteroduplex DNA is consistent with an ATP-dependent translocation mechanism. *J. Biol. Chem.* **273**, 32055–32062 (1999).

18. Blackwell, L. J., Wang, S. & Modrich, P. DNA Chain Length Dependence of Formation and Dynamics of hMutSα·hMutLα·Heteroduplex Complexes. *J. Biol. Chem.* **276**, 33233–33240

(2001).

19. Allen, D. J. *et al.* MutS mediates heteroduplex loop formation by a translocation mechanism of hemimethylated heteroduplex DNA is subject to correc-Genetic and biochemical experiments have implicated ten products in the methyl-directed reaction [MutS, binding protein (SSB), e. *EMBO J.* **16**, 4467–4476 (1997).

20. Hao, P. *et al.* Recurrent mismatch binding by MutS mobile clamps on DNA localizes repair complexes nearby. *Proc. Natl. Acad. Sci. U. S. A.* **117**, 17775–17784 (2020).

21. Junop, M. S., Obmolova, G., Rausch, K., Hsieh, P. & Yang, W. Composite active site of an ABC ATPase: MutS uses ATP to verify mismatch recognition and authorize DNA repair. *Mol. Cell* **7**, 1–12 (2001).

22. Junop, M. S., Yang, W., Funchain, P., Clendenin, W. & Miller, J. H. In vitro and in vivo studies of MutS, MutL and MutH mutants: Correlation of mismatch repair and DNA recombination. *DNA Repair (Amst).* **2**, 387–405 (2003).

23. Jiricny, J. Postreplicative mismatch repair. *Cold Spring Harb. Perspect. Biol.* **5**, 1–23 (2013).

24. Lujan, S. A. & Kunkel, T. A. Stability across the Whole Nuclear Genome in the Presence and Absence of DNA Mismatch Repair. *Cells* **10**, (2021).

25. Arana, M. E. & Kunkel, T. A. Mutator phenotypes due to DNA replication infidelity. *Semin. Cancer Biol.* **20**, 304–311 (2010).

26. Tham, K. C. *et al.* Mismatch repair inhibits homeologous recombination via coordinated directional unwinding of trapped DNA structures. *Mol. Cell* **51**, 326–337 (2013).

27. Yoshioka, K., Yoshioka, Y. & Hsieh, P. ATR Kinase Activation Mediated by MutSα and MutLα in Response to Cytotoxic O6-Methylguanine Adducts. *Mol. Cell* **22**, 501–510 (2006).

28. Rayssiguier, C., Thaler, D. S. & Radman, M. The barrier to recombination between Escherichia coli and Salmonella typhimurium is disrupted in mismatch-repair mutants. *Nature* **342**, 396–401 (1989).

29. Shimodaira, H., Yoshioka-Yamashita, A., Kolodner, R. D. & Wang, J. Y. J. Interaction of mismatch repair protein PMS2 and the p53-related transcription factor p73 in apoptosis response to cisplatin. *Proc. Natl. Acad. Sci. U. S. A.* **100**, 2420–2425 (2003).

30. Modrich, P. & Lahue, R. Mismatch repair in replication fidelity, genetic recombination, and cancer biology. *Annu. Rev. Biochem.* **65**, 101–133 (1996).

31. Kolodner, R. D. & Marsischky, G. T. Eukaryotic DNA mismatch repair. *Curr. Opin. Genet. Dev.* **9**, 89–96 (1999).

32. Duckett, D. R. *et al.* Human MutScv recognizes damaged DNA base pairs containing. **93**, 6443–6447 (1996).

33. Transduction, C. S. *et al.* Role of Postreplicative DNA Mismatch Repair in the Cytotoxic Action of Thioguanine. **273**, 1109–1111 (1996).

34. Containing, D. N. A., Waters, T. R. & Swann, P. F. Cytotoxic Mechanism of 6-Thioguanine : hMutS R , the Human Mismatch Binding. **2960**, 2501–2506 (1997).

35. Yan, T., Berry, S. E., Desai, A. B. & Kinsella, T. J. DNA Mismatch Repair (MMR) Mediates 6-Thioguanine Genotoxicity by Introducing Single-strand Breaks to Signal a G 2 -M Arrest in MMR-proficient RKO Cells 1. **9**, 2327–2334 (2003).

36. Aebi, S. *et al.* Loss of DNA mismatch repair in acquired resistance to cisplatin. *Cancer Res.* **56**, 3087–3090 (1996).

37. Higgins, C. F. & Linton, K. J. The ATP switch model for ABC transporters. *Nat. Struct. Mol. Biol.* **11**, 918–926 (2004).

38. Lamers, M. H., Winterwerp, H. H. K. & Sixma, T. K. The alternating ATPase domains of MutS control DNA mismatch repair. *EMBO J.* **22**, 746–756 (2003).

39. Warren, J. J. *et al.* Structure of the Human MutSα DNA Lesion Recognition Complex. *Mol. Cell* **26**, 579–592 (2007).

40. Mendillo, M. L., Putnam, C. D. & Kolodner, R. D. Escherichia coli MutS tetramerization domain structure reveals that stable dimers but not tetramers are essential for DNA mismatch repair in vivo. *J. Biol. Chem.* **282**, 16345–16354 (2007).

41. Schofield, M. J. *et al.* The Phe- X -Glu DNA Binding Motif of MutS. *J. Biol. Chem.* **276**, 45505–45508 (2001).

42. Lebbink, J. H. G. *et al.* Dual role of MutS glutamate 38 in DNA mismatch discrimination and in the authorization of repair. *EMBO J.* **25**, 409–419 (2006).

43. Tessmer, I. *et al.* Mechanism of MutS Searching for DNA Mismatches and Signaling Repair. *J. Biol. Chem.* **283**, 36646–36654 (2008).

44. Lebbink, J. H. G. *et al.* Dual role of MutS glutamate 38 in DNA mismatch discrimination and in the authorization of repair. *EMBO J.* **25**, 409–419 (2006).

45. Gorman, J. *et al.* Dynamic Basis for One-Dimensional DNA Scanning by the Mismatch Repair Complex Msh2-Msh6. *Mol. Cell* **28**, 359–370 (2007).

46. Gradia, S. *et al.* hMSH2-hMSH6 forms a hydrolysis-independent sliding clamp on mismatched DNA. *Mol. Cell* **3**, 255–261 (1999).

47. Yang, X. W. *et al.* MutS functions as a clamp loader by positioning MutL on the DNA during mismatch repair. *Nat. Commun.* **13**, 5808 (2022).

48. Ban, C. & Yang, W. Crystal structure and ATPase activity of MutL: Implications for DNA repair and mutagenesis. *Cell* **95**, 541–552 (1998).

49. Inouye, M. & Rinku, D. GHKL, an emergent ATPase / kinase superfamily Rinku Dutta and. *Trends Biochem. Sci.* 24–28 (2000) doi:PII: S0968-0004(99)01503-0.

50. Borsellini, A., Lebbink, J. H. G. & Lamers, M. H. MutL binds to 3' resected DNA ends and blocks DNA polymerase access. *Nucleic Acids Res.* **50**, 6224–6234 (2022).

51. Charbonnier, Jean-baptiste & Guarné, A. Insights from a decade of biophysical studies on MutL : Roles in strand discrimination and mismatch removal. *Prog. Biophys. Mol. Biol.* **117**, 149–156 (2015).

52. Mardenborough, Y. S. N. *et al.* The unstructured linker arms of MutL enable GATC site incision beyond roadblocks during initiation of DNA mismatch repair. *Nucleic Acids Res.* **47**, 11667–11680 (2019).

53. Guarné, A. *et al.* Structure of the MutL C-terminal domain: A model of intact MutL and its roles in mismatch repair. *EMBO J.* **23**, 4134–4145 (2004).

54. Pluciennik, A., Burdett, V., Lukianova, O., O'Donnell, M. & Modrich, P. Involvement of the β clamp in methyl-directed mismatch repair in vitro. *J. Biol. Chem.* **284**, 32782–32791 (2009).

55. Pluciennik, A. *et al.* Extrahelical (CAG)/(CTG) triplet repeat elements support proliferating cell nuclear antigen loading and MutLa endonuclease activation. *Proc. Natl. Acad. Sci. U. S. A.* **110**, 12277–12282 (2013).

56. Lebbink, J. H. G. *et al.* Magnesium coordination controls the molecular switch function of DNA mismatch repair protein MutS. *J. Biol. Chem.* **285**, 13131–13141 (2010).

57. Bjornson, K. P., Allen, D. J., Modrich, P., Carolina, N. & October, R. V. Modulation of MutS ATP Hydrolysis by DNA Cofactors †. *Biochemistry* **39**, 3176–3183 (2000).

58. Biswas, I. & Vijayvargia, R. mismatch repair protein from Thermus aquaticus. *Biochemistry* **886**, 881–886 (2000).

59. Acharya, S., Foster, P. L., Brooks, P. & Fishel, R. The coordinated functions of the E. coli MutS and MutL proteins in mismatch repair. *Mol. Cell* **12**, 233–246 (2003).

60. Blackwell, L. J., Bjornson, K. P., Allen, D. J. & Modrich, P. Distinct MutS DNA-binding Modes That Are Differentially Modulated by ATP Binding and Hydrolysis. *J. Biol. Chem.* **276**, 34339–34347 (2001).

61. Antony, E. & Hingorani, M. M. Asymmetric ATP Binding and Hydrolysis Activity of the Thermus aquaticus MutS Dimer Is Key to Modulation of Its Interactions with Mismatched DNA. *Biochemistry* **43**, 13115–13128 (2004).

62. Mazur, D. J., Mendillo, M. L. & Kolodner, R. D. Inhibition of Msh6 ATPase Activity by Mispaired DNA Induces a Msh2(ATP)-Msh6(ATP) State Capable of Hydrolysis-Independent Movement along DNA. *Mol. Cell* **22**, 39–49 (2006).

63. Bjornson, K. P. & Modrich, P. Differential and simultaneous adenosine di- and triphosphate binding by MutS. *J. Biol. Chem.* **278**, 18557–18562 (2003).

64. Hingorani, M. M. Mismatch binding, ADP-ATP exchange and intramolecular signaling during mismatch repair. *DNA Repair (Amst).* **38**, 24–31 (2016).

65. Sharma, A., Doucette, C., Biro, F. N. & Hingorani, M. M. Slow Conformational Changes in MutS and DNA Direct Ordered Transitions between Mismatch Search, Recognition and Signaling of DNA Repair. *J. Mol. Biol.* **425**, 4192–4205 (2013).

66. Obmolova, G., Ban, C., Hsieh, P. & Yang, W. Crystal structures of mismatch repair protein MutS and its complex with a substrate DNA. *Nature* **407**, 703–710 (2000).

67. Joshi, A., Sen, S. & Rao, B. J. ATP-hydrolysis-dependent conformational switch modulates the stability of MutS-mismatch complexes. *Nucleic Acids Res.* **28**, 853–861 (2000).

68. Lamers, M. H. *et al.* The crystal structure of DNA mismatch repair protein MutS binding to a G·T mismatch. *Nature* **407**, 711–717 (2000).

69. Natrajan, G. *et al.* Structures of Escherichia coli DNA mismatch repair enzyme MutS in complex with different mismatches: A common recognition mode for diverse substrates. *Nucleic Acids Res.* **31**, 4814–4821 (2003).

70. Selmane, T., Schofield, M. J., Nayak, S., Du, C. & Hsieh, P. Formation of a DNA Mismatch Repair Complex Mediated by ATP. *J. Mol. Biol.* **334**, 949–965 (2003).

71. Hopfner, K. P. *et al.* Structural biology of Rad50 ATPase: ATP-driven conformational control in DNA double-strand break repair and the ABC-ATPase superfamily. *Cell* **101**, 789–800 (2000).

72. Zhou, Y., Ojeda-May, P. & Pu, J. H-loop histidine catalyzes ATP hydrolysis in the E. coli ABC-

transporter HlyB. *Phys. Chem. Chem. Phys.* **15**, 15811–15815 (2013).

73. Giron-Monzon, L. *et al.* Mapping protein-protein interactions between MutL and MutH by cross-linking. *J. Biol. Chem.* **279**, 49338–49345 (2004).

74. Ahrends, R. *et al.* Identifying an interaction site between MutH and the C-terminal domain of MutL by crosslinking, affinity purification, chemical coding and mass spectrometry. *Nucleic Acids Res.* **34**, 3169–3180 (2006).

75. Hermans, N. *et al.* Dual daughter strand incision is processive and increases the efficiency of DNA mismatch repair. *Nucleic Acids Res.* **44**, 6770–6786 (2016).

76. Lawrence, A. M. & Besir, H. Staining of proteins in gels with Coomassie G-250 without organic solvent and acetic acid. *J. Vis. Exp.* 2–4 (2009) doi:10.3791/1350.

77. Baerenfaller, K., Fischer, F. & Jiricny, J. Characterization of the 'Mismatch Repairosome' and Its Role in the Processing of Modified Nucleosides In Vitro. *Methods Enzymol.* **408**, 285–303 (2006).

78. Schindelin, J. *et al.* Fiji - an Open platform for biological image analysis. *Nat. Methods* **9**, (2009).

79. Krämer, S. D., Wöhrle, J., Rath, C. & Roth, G. Anabel : An Online Tool for the Real-Time Kinetic Analysis of Binding Events. (2019) doi:10.1177/1177932218821383.

80. OXENBURGH, M. S. & SNOSWELL, A. M. Use of Streptomycin in the Separation of Nucleic Acids from Protein in a Bacterial Extract. *Nature* **207**, 1416–1417 (1965).

81. Penney, C. L. A simple micro-assay for inorganic phosphate. *Anal. Biochem.* **75**, 201–210 (1976).

82. Van Veldhoven, P. P. & Mannaerts, G. P. Inorganic and organic phosphate measurements in the nanomolar range. *Anal. Biochem.* **161**, 45–48 (1987).

83. Duxbury, D. F. The Photochemistry and Photophysics of Triphenylmethane Dyes in Solid and Liquid Media. *Chem. Rev.* **93**, 381–433 (1993).

84. Itaya, K. & Ui, M. A new micromethod for the colorimetric determination of inorganic phosphate. *Clin. Chim. Acta* **14**, 361–366 (1966).

85. Martínez Gache, S. A., Recoulat Angelini, A. A., Sabeckis, M. L. & González Flecha, F. L. Improving the stability of the malachite green method for the determination of phosphate using Pluronic F68. *Anal. Biochem.* **597**, 113681 (2020).

86. Baykov, A. A., Evtushenko, O. A. & Avaeva, S. M. A malachite green procedure for orthophosphate determination and its use in alkaline phosphatase-based enzyme immunoassay. *Anal. Biochem.* **171**, 266–270 (1988).

87. Acharya, S. Mutations in the signature motif in MutS affect ATP-induced clamp formation and mismatch repair. *Mol. Microbiol.* **69**, 1544–1559 (2008).

88. Lamers, M. H. *et al.* ATP increases the affinity between MutS ATPase domains: Implications for ATP hydrolysis and conformational changes. *J. Biol. Chem.* **279**, 43879–43885 (2004).

89. Schofield, M. J. *et al.* The Phe-X-Glu DNA binding motif of MutS: The role of hydrogen bonding in mismatch recognition. *J. Biol. Chem.* **276**, 45505–45508 (2001).

90. Groothuizen, F. S. *et al.* Using stable MutS dimers and tetramers to quantitatively analyze DNA mismatch recognition and sliding clamp formation. *Nucleic Acids Res.* **41**, 8166–8181

(2013).

91. Blouin, S., Craggs, T. D., Lafontaine, D. A. & Penedo, J. C. *Functional studies of DNA-protein interactions using FRET techniques*. *Methods in Molecular Biology* vol. 1334 (2015).

92. Kunetsky, V. *et al.* DNA mismatch and damage detection using a FRET-based assay for monitoring the loading of multiple MutS sliding clamps. *bioRxiv* 2021.07.23.453479 (2021) doi:10.1101/2021.07.23.453479.

93. Dragan, A. I. *et al.* SYBR Green I: Fluorescence properties and interaction with DNA. *J. Fluoresc.* **22**, 1189–1199 (2012).

94. Hochreiter, B., Kunze, M., Moser, B. & Schmid, J. A. Advanced FRET normalization allows quantitative analysis of protein interactions including stoichiometries and relative affinities in living cells. *Sci. Rep.* **9**, 1–16 (2019).

95. Ban, C., Junop, M. & Yang, W. Transformation of MutL by ATP binding and hydrolysis: A switch in DNA mismatch repair. *Cell* **97**, 85–97 (1999).

96. Winkler, I. *et al.* Chemical trapping of the dynamic MutS-MutL complex formed in DNA mismatch repair in Escherichia coli. *J. Biol. Chem.* **286**, 17326–17337 (2011).

Acknowledgements

I am deeply grateful for the support and guidance provided by Dr. Ir. Joyce Lebbink throughout the course of this thesis. Despite her busy schedule, she always made time to offer valuable advice and discuss my experimental data, often leading to lively and engaging conversations. I would also like to express my gratitude to Charlie Laffeber, who taught me essential laboratory techniques and contributed to many fruitful discussions that shaped the direction of this project. Special thanks are due to Kelly de Koning for teaching me how to purify proteins and for sharing many laughs with me in the lab. Finally, I would like to thank my friends and family for their unwavering support and encouragement throughout this project. It has been an incredibly fulfilling and enjoyable experience.

Appendix

Oligonucleotides used during substrate DNA preparations:

Oligonucleotides*	**Sequence (5'-3')**
GT14^{AF647}	CCAGACGTCTGTCGACGTTGGGAAGCTTGAGTATTCTATAGTGTCACCT
AT14^{AF647}	CCAGACGTCTGTCAACGTTGGGAAGCTTGAGTATTCTATAGTGTCACCT
GT14	CCAGACGTCTGTCGACGTTGGGAAGCTTGAGTATTCTATAGTGTCACCT
AT14	CCAGACGTCTGTCAACGTTGGGAAGCTTGAGTATTCTATAGTGTCACCT
Bio-41Tup	**bio**-ATAGGACGCTGACACTGGTGCTTGGCAGCTTCTAATTCGAT
Bio-41Glow	**bio**-ATCGAATTAGAAGCTGCCAGGCACCAGTGTCAGCGTCCTAT
Bio-41Alow	**bio**-ATCGAATTAGAAGCTGCCAAGCACCAGTGTCAGCGTCCTAT
41Tup	ATAGGACGCTGACACTGGTGCTTGGCAGCTTCTAATTCGAT
41Glow	ATCGAATTAGAAGCTGCCAGGCACCAGTGTCAGCGTCCTAT
41Alow	ATCGAATTAGAAGCTGCCAAGCACCAGTGTCAGCGTCCTAT

*Nucleotides indicated in bright green constitute the mismatch. Nucleotides indicated in red are fluorescently labelled using an Alexa Fluor® 647 fluorophore. "**bio**" indicates the presence of a covalently linked biotin moiety.

Sequencing primers:

Sequencing primer	**Sequence (5'-3')**
MutS Fw	GACGCCCATACGCCCATGATGC
MutS Fw2	GCACTAATCCTGCGGAACTG
MutS Fw3	CGCTTTCCAGCAACTGCCGG
MutS Fw4	GAAGAAACTTCGCCTGCGGT
T7 Rev	GGGTTATGCTAGTTATTGCTCAGCGG
T7 Fw	GCGAAATTAATACGACTCACTATAGG

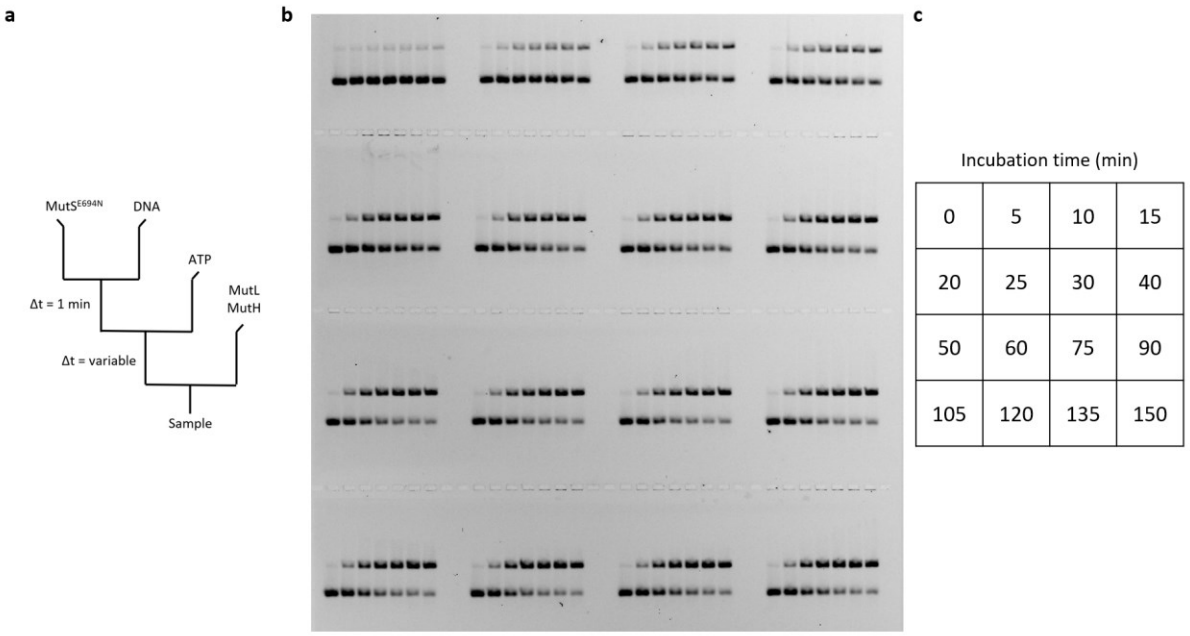

Figure 72. Exemplary gel data revealing dependency of MutH activation on incubation time by the MutS^{E694N} sliding clamps prior to addition of MutL and MutH in the absence of trap oligonucleotides. ***a****, Schematic summary of the order of addition.* ***b****, Exemplary gel data.* ***c****, Matrix with incubation times corresponding to the series shown in* ***b****.*

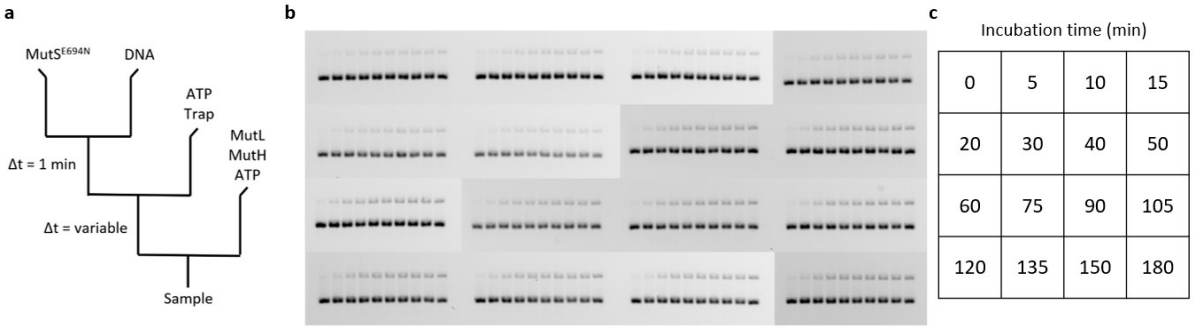

Figure 73. Exemplary gel data revealing dependency of MutH activation on incubation time by the MutS^{E694N} sliding clamps prior to addition of MutL and MutH in the presence of trap oligonucleotides. ***a****, Schematic summary of the order of addition.* ***b****, Exemplary gel data.* ***c****, Matrix with incubation times corresponding to the series shown in* ***b****.*

“The more we know, the more we realize there is to know.” - Jennifer Doudna